Doctoral Programme in
Biomedicine and Biotechnology

PhD thesis

Mouse model for Charcot-Marie-Tooth as a tool to better understand the disease

Manuela Barneo Muñoz

Directed by : Francesc Palau Martínez
Paula Juárez Gómez

Tutor: David Ruiz Arahal

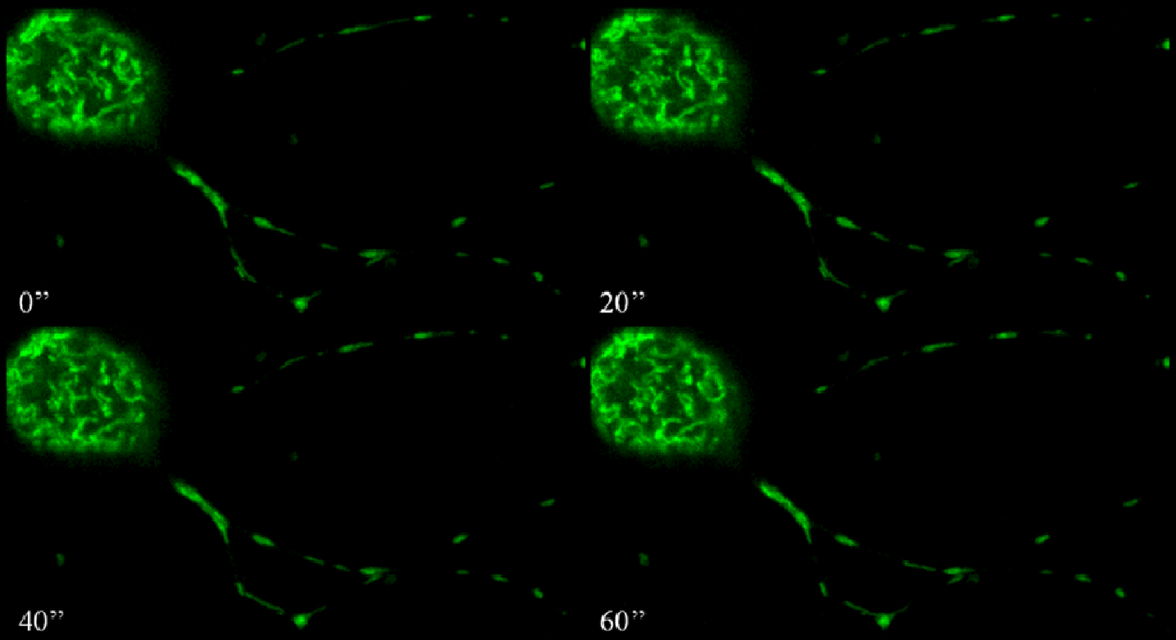

Doctoral Programme in Biomedicine and Biotechnology

PhD thesis

Mouse model for Charcot-Marie-Tooth as a tool to better understand the disease

Manuela Barneo Muñoz

Directed by:
Francesc Palau Martínez
Paula Juárez Gómez
Tutor:
David Ruiz Arahal

This thesis has been possible thanks to a Formación Personal Investigador fellowship (BES-2010-040234) as part of Plan Nacional Poject named "Papel de la mitocondria en la neurodegeneración de las neuropatías periféricas hereditarias" (SAF2009-07063).

Dr Coleman's laboratory stay was possible thanks to Estancias Breves Program (EEBB-I-14-00467) named "Estudio del movimiento mitocondrial un el modelo murino para la enfermedad de Charcot-Maire-Tooth deficiente en *Gdap1*".

In addition, as a result of part of this thesis a paper has been published named Lack of GDAP1 induces neuronal calcium and mitochondrial defects in a knockout mouse model of Charcot-Marie-Tooth neuropathy**,** Barneo-Muñoz M, Juárez P, Civera A, Yndriago L, Pla-Martin D, Zenker J, Cuevas C, Estela A, Sánchez-Aragó M, Forteza-Vila J, Cuezva JM, Chrast R, Palau P. (2015) PLOS Genetics DOI:10.1371/journal.pgen.1005115.

Ever tried.
Ever failed.
No matter.
Try again.
Fail again.
Fail better.

Samuel Beckett

Thank you letter:

No puedo estar más de acuerdo con las palabras de Samuel Beckett de la página anterior. La verdad es que no se si él se refería a la realización de una tesis doctoral ya se puede aplicar a la vida en general. No obstante, si nos centramos en el trabajo en el laboratorio, es cierto que nos caemos muchas veces. Hay experimentos que no son fáciles de poner a punto y nos desesperamos. Sin embargo, cambiamos algún parámetro y volvemos a intentarlo con la misma ilusión.

La tesis doctoral se resume en eso: aprendizaje. Aprendemos técnicas de laboratorio, aprendemos a desenvolvernos en público, aprendemos a escribir ciencia,... Aprendemos de la gente que nos rodea, de nuestros compañeros de laboratorio que al final pasan a ser compañeros de la vida, amigos.

Llegados a este punto, creo que es el momento de agradecer a todas las personas que han hecho posible que hoy me encuentre escribiendo los agradecimientos de mi tesis doctoral.

I am totally agree more with the words of Samuel Beckett on the previous page. Indeed, I do not know if he was speaking about a PhD thesis; it can be applied to life in general. However, if we focus on the laboratory work, it is true that many times we fall. There are experiments that are not so easy to set up and we despair. Despite this we change a parameter and try again with the same enthusiasm.

The thesis is summarized in that: learning. Learn laboratory techniques, learn how manage in public, learn writing science ... We learn from the people around to us, our lab partners that ultimately become life partners, friends.

At this point, I think it's time to thank all the people who have made possible that today I am writing the thank you letter of my thesis.

En primer lugar, me gustaría dar las gracias al Dr Palau por haber depositado en mí su confianza. Gracias Paco por haberme seleccionado como becaría FPI. Gracias también por haberme dirigido, junto con la Dra Juárez. Gracias a los dos por todas las discusiones sobre ratones, mitocondrias, tablas, figuras y demás.

Por supuesto todo este trabajo no hubiera sido posible sin un laboratorio, un grupo de personas que día tras día hemos trabajado codo con codo para sacar el trabajo adelante, tanto en el Instituto de Biomedicina de Valencia (IBV) como en el Centro de Investigación Príncipe Felipe (CIPF). Gracias a Amalia Capilla, Ana Giménez, Anna Estela, Arantxa Bolinches, Azahara Civera, Belén Mollá, Benito Alarcón, Carme Cucarella, Carmen Carceller, Carmen Espinós, David Pla, Diana Muñoz, Diego Cerveró, Edu Calpena, Elena Carceller, Estela Pérez, Estrella Rubio, Fátima Riveiro, Ibo Galindo, Ingrid Mendes, Inma Ballester, Janet Hoenicka, Jerónimo Forteza, Jorge, Larissa Gómez, Laura Yndriago, Laura Ramírez, Lola Martínez, Lorena Serrano, Lucía Díaz, Luis Navarro, Manuel, Manolo, Soriano, Mª Luz Pinci, María Benavente, Mª Elena Mateo, Mario Soriano, Marta Casado, Mireia Tondo, Paloma González, Pascual Sanz, Paula Sancho, Pepe Cubells, Pili González, Raúl, Salva Martí, Sara Fernández, Stïjn, Susana Paricio, Susana Rovira, Vicente Villarta, Víctor López, Vicenzo Lupo, Viviana Bisbal y a todo IBV-ocio. Gracias porque habéis colaborado en mi formación, porque me habéis ayudado, porque habéis cuidado a los ratones como si fuera vuestra tesis la que estaba en juego,… De verdad que me llevo un pedacito de cada uno. Todos, y alguno más que me dejo, formáis parte de mi vida. Intentaré no olvidar vuestros consejos.

Gracias también a mi tutor, el Dr. David Ruiz Arahal, por su amabilidad y sonrisa siempre disponible.

This thesis has been also possible thanks to Dr Coleman's hospitality. I really appreciate all your help, thanks for be so patient with me. Thanks Michael, Jon and Stefan for have been so kind with me and teach me how work with live imaging and with life real. Thanks Christy, Claire, Mat, Robert and Stacey to make me feel part of the team. Thank you, Anastasiya, Maria and Valentina, to make me feel at home.

Tampoco me quiero olvidar de los inicios. Quisiera dar las gracias al Dr Gabino Rios por atender a una estudiante de 4º de biología en su ansia por entrar en un laboratorio. Nunca olvidaré la importancia de colocar balanceados los eppendorfs en la centrífuga.

Tampoco olvidaré como trabajar en una campana de flujo laminar, cómo destapar un tubo con una sola mano mientras la otra pipetea; gracias Salva y Gloria. Gracias a todo el laboratorio del Dr Joan Ferré: Agata, Anabel, Balta, Cristina, Ezequiel, Gloria, Ivan, Joan, Joel, Juliana, Leila, Maissa, María, Marina, Núria, Patricia, Rosi, Salva, Sara, Silvia y Yolanda. Gracias también a Amparo, Bea, Mª Carmen y JuanMa. Hicisteis que una niña creyera que se podía dedicar a la investigación y me auxiliasteis en el camino.

Gracias también al laboratorio de Genómica Funcional de Levaduras. Gracias Paula y José Enrique por encargarme mi primer "poyectito" y por volver a confiar en mi ahora otra vez. Gracias a Adriana, Alice, Carlos, Carmen, Daniel, Elena, Esther, Fany, Fernando, Jordi, María, Marta, Nati, Nikki, Oreto, Pepe, Tian y Toni por vuestros consejos y enseñanzas.

Por supuesto, gracias también a mis amigos de la carrera y del pueblo: Alejandra, Anna, Aurora, Mari, Teresa, Ferran, Jaume, Salva, Inés y Javi, Irene y Pau, Miriam y Tomy, José Antonio y Raquel, Fanny y Notario, Lledó y Campillo, Ángel y Jaume, Bet y Álex, Pepa e Iván, Bea y Náger, Vanesa, Trini, Mª Angeles,….. Todos me habéis comprendido cuando no podía quedar porque tenía ratones. Me habéis soportado y me habéis dado ánimos.

No me quiero olvidar de mi familia, en especial a mi madre que es la que más ha "sufrido" todo esto. Gracias mamá por estar ahí aun sin entender que seguir estudiando después de la carrera se puede considerar un trabajo. Gracias Marijose, Jacin, Paco, Eric y Javi por apoyarme en los momentos difíciles.

Per últim, vull donar les gràcies també a la persona en la que formaré la meua pròpia família. Gràcies Jose Manuel per existir, per haver-me trobat. Sense tu haguera sigut impossible somniar desperta. Gràcies per ensenyar-me a tindre paciència; encara estic aprenent.

Abbreviations

ACh	Acetylcholine
AChR	Acetylcholine receptors
AD	Autosomal dominant
ANT	Adenine nucleotide translocator (ADP/ATP translocator)
AR	Autosomal recessive
ATP	Adenosine triphosphate
BAX	BCL2-associated X protein
Bcl-2	B-cell CLL/lymphoma 2
BDNF	Brain-derived neurotrophic factor
bp	Base pairs
Ca^{2+}	Calcium
cDNA	Copy Deoxyribonucleic acid
CDNB	1-chloro-2,4-dinitrobenzene
CHN	Congenital hypomyelination neuropathy
CMAP	Compound muscle action potential
CMT	Charcot–Marie–Tooth disease
CMT1	Demyelinating Charcot–Marie–Tooth disease
CMT2	Axonal Charcot–Marie–Tooth disease
CMTI	Intermediate Charcot–Marie–Tooth disease
CMTX	Charcot–Marie–Tooth disease X-linked
CNS	Central nervous system
CO_2	Carbon dioxide
CoA	Coenzyme A
Complex I	Ubiquinone oxidoreductase complex
CypD	Cyclophilin D
DeSyn	Delayed synapsing NMJ
DI CMT	Dominant intermediate Charcot-Maire-Tooth
div	Days "in vitro"
DNA	Deoxyribonucleic acid
DRG	Dorsal Root Ganglia
DRP1	Dynamin-related protein-1
DSS	Dejerine–Sottas syndrome
EGR2	Early growth response 2
ER	Endoplasmic reticulum
ETC	Electron transport chain
FaSyn	Fast Synapsing NMJ
FIS1	Mitochondrial fission protein 1
GD3 synthase	alpha-N-acetyl-neuraminide alpha-2,8-sialyltransferase 1
GDAP1	Ganglioside-induced differentiation-associated protein-1
GDAP1L1	Ganglioside-induced differentiation-associated protein-1 like 1
GJB1	Gap junction protein beta 1
GSH	Glutathione
GST	Glutathione S-transferase
HD	Hydrophobic domain
HMN	Hereditary motor neuropathies

HMSN	Hereditary motor and sensory neuropathies
HPN	Hereditary peripheral neuropathies
HSAN	Hereditary sensory and autosomic neuropathies
HSN	Hereditary sensory neuropathies
HSPB1	Heat shock protein family B (small) member 1
IMM	Inner mitochondrial membrane
IN	Interneuron
KHC	Kinesin Heavy Chain
KO	Knockout
MAPs	Microtubule-associated proteins
MFF	Mitochondrial fission factor
MFN1	Mitofusin-1
MFN2	Mitofusin-2
MN	Motor neuron
MNCV	Motor nerve conduction velocity
MPTP	Mitochondrial permeability transition pore
MPZ	Myelin protein zero
mRNA	Messenger Ribonucleic acid
mtDNA	Mitochondrial DNA
MTMR2	Myotubularin related protein 2
Myo19	Myosin XIX
Na^+/K^+ ATPase	Sodium-potassium adenosine triphosphatase
NADH	Nicotinamide adenine dinucleotide (reduced form)
NEFL	Neurofilament, light polypeptide
NF	Neurofilament
NGF	Nerve growth factor
NMJ	Neuromuscular Junction
NT3	Neurotrophin-3
OMM	Outer mitochondrial membrane
OPA1	Optic Atrophy-1
OXPHOS	Oxidative phosphorylation
P0	Myelin protein zero (MPZ)
P1	Postnatal day 1
PCR	Polymerase Chain Reaction
PMP22	Peripheral myelin protein 22
PNS	Peripheral Nervous System
PRX	Periaxin
RAB6B	Member RAS oncogene family
RNA	Ribonucleic acid
ROS	Reactive Oxygen Species
RT-PCR	Reverse Transcriptase Polymerase Chain Reaction
SC	Spinal Cord
SCG	Superior Cervical Ganglion
SEM	Standard Error of the Mean
SN	Sensory neuron
SNAP	Sensory nerve action potential

SNPH	Syntaphilin
SOCE	Store-operated Ca^{2+} entry
SOD	Superoxide dismutase
TCA	Citric acid cycle
TMD	Transmembrane domain
Trk	Tropomyosinreceptor- kinase
TSC	Terminal Schwann cells
UCP	Mitochondrial uncoupling proteins
VDAC	Voltage-dependent anion channel
WAVE1	WASP family verprolin homologous protein 1
WT	Wild type
$\Delta\Psi m$	Inner mitochondrial membrane potential

Spanish Abstract

Introducción

La enfermedad de Charcot-Marie-Tooth (CMT) es uno de los trastornos neurológicos hereditarios más comunes que afecta a 17-40 de cada 100.000 personas según poblaciones; concretamente esta cifra se sitúa en 28 personas de cada 100.000 en España. La enfermedad recibe el nombre de los tres médicos que la identificaron por primera vez en 1886; Jean-Marie Charcot y Pierre Marie en París, Francia y Howard Henry Tooth en Cambridge, Inglaterra. La enfermedad de CMT, también conocida como neuropatía hereditaria motora y sensitiva o atrofia muscular del peroneo, abarca un grupo de trastornos que afectan los nervios periféricos.

El fenotipo clásico incluye problemas en la marcha, déficit sensorial distal y atrofia distal inferior dando un aspecto de "jambes de coq" o botella de champagne invertida. Otras características completan el deterioro de patrón distal típico de CMT. Por ejemplo, disminución o ausencia de reflejos y equilibrio debido a la pérdida propioceptiva y deformidades esqueléticas como "pes cavus" y dedos en martillo. La escoliosis moderada puede formar parte de este fenotipo clínico. La severidad de la neuropatía puede evaluarse por un marcador de la neuropatía de CMT, un examen clínico de nueve ítems que mide síntomas sensoriales, síntomas motores, velocidades de conducción nerviosa y fuerza en brazos y piernas.

De hecho, clínicamente, la examinación electrofisiológica es el primer paso importante de la división de CMT en subtipos. Los estudios de conducción nerviosa permiten una clasificación preliminar en formas desmielinizantes, axonales o intermedias. En la mayoría de los casos, la velocidad de conducción de los nervios motores (MNCV) y las amplitudes del potencial de acción compuesto del músculo (CMAP) en las extremidades superiores son necesarias ya que los nervios de la extremidades inferiores a menudo muestran ausencia de respuesta. Se diagnostica *CMT1 o desmielinizante* si esta velocidad de conducción motora es menor de 38 m/s. Si esta velocidad motora es normal (mayor de 45 m/s), se observa disminución de la amplitud de CMAP y disminución del potencial de acción del nervio sensitivo (SNAP), se diagnostica *CMT2 o axonal*. *CMT Intermedia* (CMTI) se diagnostica si MNCV entra en el rango de 25 – 45 m/s.

Otra clasificación, según el tipo de herencia, también es posible. La variante de disfunción de la mielina -CMT1- y la variante axonal -CMT2- presentan herencia autosómico dominante (AD), mientras que CMTX es un desorden ligado al cromosoma X. En cambio, variantes con herencia autosómica recesiva (AR CMT) se clasifican como CMT4 si tienen características desmielinizantes y CMT2B o CMT2 AR si tienen resultados axonales (Tazir et al. 2014).

Hasta la fecha, 80 genes causantes de CMT han sido identificados (Timmerman et al. 2014). Algunos de ellos son causantes de diversos subtipos de CMT. Ya en el año 2002 dos grupos asociaron un mismo gen -*GDAP1* (MIM# 606598)- a dos subtipos de CMT, desmielinizante autosómica recesiva (Baxter et al. 2002) y axonal autosómica recesiva (Cuesta et al. 2002).

En la actualidad se sabe que *GDAP1* (Ganglioside-induced Differentiation Associated Protein 1) causa tanto CMT4A (MIM# 214400) desmielinizante autosómica recesiva, AR-CMT2K (MIM# 607706) axonal autosómica recesiva, CMT2K (MIM# 607831) axonal autosómica dominante, como CMTRIA (MIM# 608340) intermedia autosómica recesiva (www.omim.org). Es importante remarcar que en el área Mediterránea gran parte de los casos de CMT son debidos a mutaciones en *GDAP1* (Sivera et al. 2013).

GDAP1 se había identificado con anterioridad como uno de los 10 cDNAs expresados en una línea celular de neuroblastoma ratón diferenciada (Neuro2), en la que la diferenciación colinérgica había sido inducida por transfección de GD3 sintasa (a2,8-sialiltransferasa). Este gen, con una longitud de 23,728 pares de bases (pb), contiene seis exones y cinco intrones. Dos variantes transcripcionales han sido descritas, siendo la isoforma "a" la más larga, con 358 aminoácidos. La isoforma "b" es exactamente igual que la "a" pero tiene 68 aminoácidos menos en la parte N-terminal, resultando en una proteína de 290 aminoácidos (Cassereau et al. 2011).

GDAP1 pertenece a la familia de enzimas glutatión S-transferasas, presentando dos dominios de unión para GSH (de los aminoácidos 26 al 119 y del 210 al 287). La proteína presenta también dos hélices -α4 y α5- (entre los aminoácidos 152-164 y 169-195), un único dominio transmembrana (TMD) en el extremo de la C-terminal y un dominio hidrófobo (HD) (Marco et al. 2004). A la misma familia pertenece su gen parálogo, *GDAP1L1* (Marco et al. 2004), del que poco se ha estudiado.

Estudios de expresión han detectado su mensajero predominantemente en sistema nervioso (Cuesta et al. 2002; Pedrola et al. 2005). La proteína ha sido detectada tanto en neuronas sensitivas y motoneuronas (Pedrola et al. 2008), como en células de Schwann (Pedrola et al. 2005; Niemann et al. 2005). A nivel celular, se localiza en la membrana mitocondrial externa (Pedrola et al. 2005; Niemann et al. 2005).

La función de GDAP1 ha sido profundamente estudiada en modelos celulares. Aunque no se ha conseguido detectar actividad glutatión S-transferasa (Pedrola et al. 2005), algunos autores relacionan esta proteína con el estrés oxidativo (Noack et al. 2012). Lo que sí ha sido ampliamente demostrado es el rol de *GDAP1* como regulador de la dinámica mitocondrial; actuando como factor de fisión mitocondrial independiente de *FIS1* y *DRP1* (Niemann et al. 2005; Niemann et al. 2009). Otros autores también relacionan a *GDAP1* con el movimiento mitocondrial (Pla-Martín et al. 2013). Además, también ha sido relacionado con la fisión de lo peroxisomas (Huber et al. 2013) y la homeóstasis del calcio (Pla-Martín et al. 2013).

Hipótesis y objetivos

Basándonos en estudios previos hechos en cultivo celular y en la patofisiología de los pacientes de CMT, nuestra hipótesis es que *GDAP1* está implicado en el transporte mitocondrial y en el posicionamiento de dicho orgánulo dentro de las neuronas y sus axones. Así, la patología de la enfermedad se debe a la disfunción en el transporte y/o localización de las mitocondrias, lo cual puede estar relacionado con la longitud del nervio.

Así, el objetivo principal de esta tesis es investigar la función de *GDAP1* y comprender su implicación en la enfermedad de CMT. Para ello hemos generado un ratón nulo para el ortólogo murino de *GDAP1* como herramienta para investigar cómo la falta de función del gen causa la neuropatía. Avances en este tema pueden llegar a prevenir o reparar la axonopatía.

Como primer punto de la tesis, es necesario caracterizar nuestro modelo de ratón y asegurarnos que es adecuado como modelo de CMT. Una vez este objetivo se ha conseguido, ya podremos utilizarlo como herramienta para entender en profundidad en proceso patogénico.

Resultados y Discusión

El ratón nulo para *Gdap1* (*Gdap1*$^{-/-}$) se generó suprimiendo el exón 1 del *Gdap1* murino mediante el sistema de recombinación Cre/loxP (genOway, Lyon, Francia; véase Materiales y Métodos para más detalles). Los ratones *Gdap1* $^{-/-}$ se obtuvieron mediante cruces entre heterocigotos (*Gdap1*$^{+/-}$). Los tres genotipos obtenidos en la descendencia cumplían las proporciones mendelianas y no se observaron diferencias en longevidad o fertilidad entre ellos. Los genotipos se comprobaron al tatuar los ratones, mediante biopsias de la cola que fueron utilizadas para obtener ADN genómico. Mediante diversas estrategias de PCR, y usando como molde el ADN genómico; se detectó la deleción del exón 1 en homocigosis en los ratones *Gdap1*$^{-/-}$ y en heterocigosis en los *Gdap1* $^{+/-}$. Los ratones *Gdap1*$^{+/+}$ no presentaban alteración alguna en su genoma.

La ausencia de expresión en los ratones *Gdap1* $^{-/-}$ se comprobó mediante la detección de la proteína endógena en los controles (*Gdap1*$^{+/+}$) y la carencia en los *Gdap1* $^{-/-}$. La falta de *Gdap1* se comprobó también a nivel de mensajero, concluyéndose que la deleción del primero de los seis exones de *Gdap1* es suficiente para abolir su expresión en el modelo de ratón. Además, comprobamos la expresión de su gen parálogo, *GDAP1L1*, (Marco et al. 2004); detectando el mensajero en solamente en sistema nervioso central (SNC). Este hecho contrasta con la hipótesis de que *GDAP1L1* pueda asumir la función de *GDAP1* cuando este último está mutado o delecionado (Niemann et al. 2014).

Aprovechando el hecho de tener un anticuerpo para la detección de GDAP1, nos planteamos estudiar su expresión en todos los tejidos del ratón. La proteína GDAP1 fue detectada solo en tejido nervioso, corroborándose así los datos previos (Pedrola et al. 2005; Pedrola et al. 2008).

La ausencia de *Gdap1* en el ratón provocó defectos en el caminar, como una posición anormalmente baja del cuerpo, y una pérdida de reflejos al ser sostenidos por la cola. Además, a partir de los 6 meses algunos ratones presentaban deformidades en las patas similares al *pes cavus*. Esto concuerda con el fenotipo clásico de los pacientes de CMT: andar equino y las deformidades en los pies conocidas como *pes planus* o *cavus* (Brennan et al. 2015). Estos defectos no se observaron en el modelo murino de Niemann et al. 2014.

Datos más cuantitativos obtenidos mediante rota-rod test revelaron defectos en la actividad motora debidos a la pérdida de *Gdap1* a partir de los 3 meses. Además, mediante el estudio de la pisada, se determinó que los ratones deficientes presentaban defectos en el posicionamiento de los dedos y en la forma de apoyar en pie, lo que les obliga a dar pasos más cortos. Estas alteraciones en la pisada concuerdan con mal funcionamiento de los pequeños músculos del pie inervados por el nervio ciático y la parálisis de los músculos flexores del tobillo (Wiethölter et al. 1990). A diferencia de los pacientes (Brennan et al. 2015), no se pudo detectar pérdida de masa muscular en los músculos de la pierna.

La falta de *Gdap1* en el ratón también provocaba defectos en las uniones neuromusculares (NMJ); encontrando desconexión entre el axón motor y la fibra muscular a los 12 meses de edad. No se observó la típica fragmentación de la degeneración Wallerian (Coleman & Freeman 2010); sin embargo sí se detectaron anomalías en la parte más distal del axón tipo lazos y engrosamientos. Este tipo de estructuras se han relacionado con axones en retraimiento (Bishop et al. 2004). Defectos en estas sinapsis producen debilidad o parálisis muscular (Tintignac et al. 2015).

Para finalizar la caracterización del modelo, se observó también daño en la médula espinal de ratones *Gdap1*$^{-/-}$. Produciéndose una pérdida progresiva de motoneuronas en el asta ventral. Por el contrario, no se observaron alteraciones en los ganglios de la raíz dorsal, al menos a nivel histológico.

GDAP1-CMT se ha relacionado con CMT tanto axonal como desmielinizante, por ello también se estudió la Velocidad de Conducción Nerviosa (MNCV), rasgo diferencial entre ambos tipos de CMT. A los 5 meses de edad se observó un moderado descenso en la MNCV de los ratones *Gdap1*$^{-/-}$ en comparación con los controles; hecho que también ocurre en las neuropatías axonales (Sevilla et al. 2003). En las neuropatías desmielinizantes las reducciones son mayores (Tazir et al. 2014). Estudiando el Potencial de Acción Muscular Compuesto (CMAP), también observamos reducción de en área y en la amplitud; lo que puede reflejar pérdida de motoneuronas o un desorden de las uniones neuromusculares (Murray et al. 2014).

Otra forma de clasificar CMT en axonal o desmielinizante es realizando una biopsia de algún nervio periférico, normalmente del sural (Sevilla et al. 2003). En nuestro modelo de ratón, nosotros optamos por el nervio ciático, al ser este el más largo (Krinke et al. 2014). Los ratones *Gdap1*$^{-/-}$ presentaban una menor densidad de fibras nerviosas a los 5 meses de manera similar a los pacientes (Sevilla et al. 2003). Por el contrario no se encontró alteración alguna en el g-ratio o presencia de los bulbos de cebolla característicos de los tipos desmielinizantes.

Una vez caracterizado el modelo, nuestro objetivo era entender mejor la patofisiología a nivel celular de la enfermedad. Para ello hicimos uso del cultivo de neuronas sensitivas del ganglio dorsal (DRG) de ratones adultos (Valdés-Sánchez et al. 2010). Los cultivos de DRG ratones *Gdap1*$^{-/-}$ eran capaces de crecer; sin embargo, presentaron neuronas con somas más pequeños y neuritas más cortas en comparación con los controles. Además, se detectaron problemas en las modificaciones post-traduccionales que sufre el citoesqueleto de microtúbulos en ratones de 5 meses. El menor nivel de acetilación y mayor nivel de tirosinación encontrados, se corresponden con una desestabilización de los microtúbulos; pudiendo desencadenar problemas a nivel del trasporte de vesículas y mitocondrias (Zala et al. 2013).

Además del estudio de muestras fijadas de neuronas en cultivo de DRG de ratones adultos, se estudiaron las mitocondrias en movimiento mediante la microinyección de cultivos postnatales. La microinyección nos permitió seguir las mitocondrias dentro una neurita desde su zona más proximal hasta la más distal (Gilley et al. 2011). Estudios en cultivos de DRG revelaron defectos en el movimiento retrogrado (de la zona distal a la proximal) de las mitocondrias. Concretamente se observó una tendencia al aumento del número de mitocondrias en movimiento y un aumento de su tamaño. Estos datos contrastaron con lo encontrado en cultivo de ganglio cervical superior (SCG), tejido no afectado en pacientes de CMT, donde se detectaron unas mitocondrias más lentas y con tendencia a más cortas; siendo las estáticas las que aumentaban su tamaño.

El estudio se completó con el rescate de la neuronas nulas para *Gdap1*. En DRG se observó un descenso del número de mitocondrias en sentido retrógrado así como un descenso de la velocidad en sentido anterógrado debido a la expresión de *GDAP1*. En SCG solo se observó el descenso en el número de mitocondrias en sentido retrógrado.

Aprovechando esta técnica, se analizó el efecto de las mutaciones más frecuentes de *GDAP1* en los cultivos de DRG. Mutaciones dominantes no fueron capaces de alterar los parámetros estudiados en neuronas control. Sin embargo, mutaciones dominantes y recesivas, alteraron dichos parámetros en neuronas *Gdap1*$^{-/-}$, siendo el efecto de la mutaciones en posición 157 y 161 más agresivo que el de las albergadas en posición 120. Esta relación con el sitio mutado en vez de con el tipo de herencia contrasta con la patología en pacientes donde las formas recesivas de *GDAP1*-CMT suelen ser más agresivas (Sevilla et al. 2008).

Para finalizar, se estudiaron también estos parámetros de movilidad mitocondrial en el nervio ciático del ratón gracias al uso de explantes de ratones que poseían sus mitocondrias marcadas. Ratones nulos para *Gdap1* de 1 mes de edad presentaron defectos en velocidad y tamaño de sus mitocondrias al compararlos con los controles. Concretamente, se observó un descenso en la velocidad anterógrada (del soma en la médula al terminal nervioso en el músculo) y un aumento del tamaño de las mitocondrias que se movían en sentido retrógrado (del terminal nervioso en el músculo al soma en la médula). Estos datos corroboran y explican más en profundidad las alteraciones en el movimiento mitocondrial descritas en líneas de neuroblastoma debidas a la interferencia de GDAP1 (Pla-Martín 2012).

Si repasamos todos los defectos producidos por la falta de GDAP1 en el movimiento mitocondrial y en el crecimiento de las neuronas, las proteínas MIRO/MILTON vienen a nuestra mente. MIRO es una GTPasa pequeña asociada a la mitocondria que regula el transporte de mitocondrias y la organización en las prolongaciones celulares (Tang 2015). De hecho, el ratón nulo para *Miro1* exhibe reducción en la velocidad retrógrada (Nguyen et al. 2014). De manera similar a MIRO, GDAP1 también tiene proteínas a las que se une (Pla-Martín 2012) que pueden explicar con detalle las alteraciones observadas en el ratón nulo.

La hipótesis es que GDAP1 interacciona con los transportadores SUMO4 e EIF2B5, entre otros. La pérdida de *GDAP1* afecta a diversos procesos en los que estos transportadores están implicados. La ausencia de GDAP1 hace que, de alguna manera SUMO no pueda activar DRP1 (Ong et al. 2015). Como consecuencia la fisión se bloquea produciendo mitocondrias elongadas.

Además, como GDAP1 no puede unirse a EIF2B5, EIF2 no puede tener la conformación apropiada y no puede bloquear Bcl-xL mediante CHOP (Iurlaro & Muñoz Pinedo 2015). Bcl-xL bloquea DRP1 (Saez-Atienzar et al. 2016) y como consecuencia la fisión se bloquea de nuevo. Bcl-xL también bloquea la acetilación de la tubulina (Saez-Atienzar et al. 2016) y, como consecuencia, el movimiento mitocondrial se ve afectado.

Finalmente, como GDAP1 también interacciona con Caytaxina, el ratón nulo para *Gdap1* presenta una velocidad anterógrada más lenta.

Como consecuencia de la menor velocidad anterógrada, los axones distales se denervan a nivel de las NMJs. Mitocondrias más lentas también provocan la posición incorrecta de las mitocondrias en relación con el retículo endoplasmático, así como estrés de retículo.

Conclusiones

1º: *Gdap1* murino se expresa en el sistema nervioso central y en el periférico. Tejidos no neuronales no expresan GDAP1.

2º: Otros miembros de la familia *Gdap1*, como *Gdap1L1*, también se expresan en el sistema nervioso central del ratón.

3º: La eliminación del primer exón de *Gdap1* es suficiente para generar un modelo de ratón para Charcot-Marie-Tooth (CMT) debido a mutaciones en *GDAP1*. La pérdida de expresión ubicua en el ratón no afecta a su viabilidad y fertilidad. Como modelo, el ratón *Gdap1*$^{-/-}$ presenta las principales características de la enfermedad: pie cavo, déficits motores, velocidad de conducción nerviosa ligeramente reducida y alteraciones en el potencial de acción compuesto.

4º: El uso de este modelo nos ha permitido determinar que CMT debido a *GDAP1* es una neuropatía de tipo axonal.

5º: El nervio ciático, el cual tiene axones sensitivos y motores, está alterado en ratones de 5 meses de edad. Se ha detectado pérdida del número de fibras y un cambio en el tamaño de las mismas. No se observaron signos desmielinizantes.

6º: En el músculo, la pérdida de *Gdap1* produce denervación. Las placas neuromusculares no se encuentran totalmente ocupadas por los terminales nerviosos a los 12 meses de edad. Además, detectamos estructuras anormales en dichos terminales. Las uniones neuromusculares de ratones de 5 meses de edad, son indistinguibles entre controles y animales nulos para *Gdap1*.

7º: En la parte ventral de la médula espinal, la pérdida de *Gdap1* produce una pérdida progresiva de neuronas sanas. Señales de daño han sido detectadas en lisados de la médula espinal completa.

8º: En los ganglios de la raíz dorsal (DRG), la ausencia de GDAP1 parece no alterar las neuronas sensitivas al menos a nivel histológico hasta los 12 meses de edad.

9º: Cultivos de DRG de animales adultos se ven comprometidos por la pérdida de GDAP1. Se han observado somas más pequeños y neuritas más cortas. Desestabilización del citoesqueleto de microtúbulos puede explicar estos defectos.

10º: La pérdida de GDAP1 afecta principalmente al transporte y la dinámica mitocondrial. Tejidos afectados en CMT de los ratones *Gdap1*$^{-/-}$, como DRG en cultivo y nervio ciático, presentaron mitocondrias en movimiento retrógrado más largas. Además, la velocidad anterógrada estaba reducida. Tejidos no afectados en CMT, como ganglio superior cervical en cultivo, presentó mitocondrias más cortas y lentas en movimiento retrógrado.

11º: Mutaciones en *GDAP1* presentes en pacientes de CMT produjeron efectos diversos en neuronas sensitivas en cultivo. Esta variedad de efectos concuerda con al amplio rango de fenotipos presentado en los pacientes.

Material y Métodos

Para llevar a cabo todo este estudio profundo del ratón nulo para *Gdap1* se han utilizado técnicas frecuentemente realizadas en laboratorios de genética molecular. Otras son de uso rutinario en ámbitos donde se trabaja con el ratón como animal modelo. Sin embargo también se han puesto a punto algunas técnicas novedosas en nuestro laboratorio como el estudio de las uniones neuromusculares (NMJ).

Para ello elegimos el Gastrocnemius (en la pantorrilla) como músculo de estudio por presentar unas sinapsis retrasadas (DeSyn, Delayed Synapsis), cuyo mantenimiento depende exclusivamente de los factores provenientes del nervio (Pun et al. 2002), y por ser un músculo grande de fácil acceso (Murray et al. 2014). La técnica de marcaje de las NMJ consistió en diseccionar el musculo y fijarlo en paraformaldehído. Posteriormente se marcó la parte muscular de la NMJ, el receptor de la Acetilcolina (AChR) con bungarotoxina conjugada con rodamina. Para marcar la parte del terminal nervioso se realizó una inmunohistoquímica normal con un anticuerpo primario frente a la Beta Tubulina III y un secundario conjugado con Alexa-488. Una vez realizado el marcaje, se procedió a cortar el músculo longitudinalmente para su posterior montaje en portaobjetos. Fue necesario el uso de un microscopio confocal potente para poder obtener imágenes confocales de series contiguas en z (cada 0.5µM). Con todas esas imágenes confocales ser realizó una reconstrucción en 3D con la que estudiar si las NMJ estaban correctamente inervadas. Una NMJ se contabilizó como completamente ocupada si había evidencia de una continuidad entre el terminal nervioso (Beta tubulina III) y la placa neuromuscular (AChR) (Wong et al. 2009).

Otra técnica interesante fue el uso de microinyecciones para marcar mitocondrias selectivamente en un subconjunto de neuritas de neuronas sensitivas en cultivo (Gilley & Coleman 2010). Microinyectando un marcador mitocondrial (Milde et al. 2013) en 50-60 neuronas de un total de 5000-6000 en cultivo, es relativamente fácil capturar videos de su movimiento en la parte más distal de sus neuritas. Para su posterior análisis existe también un software (Andrews et al. 2010) que nos facilita el seguimiento de las partículas en movimiento, en nuestro caso mitocondrias, calculando su velocidad y tamaño entre otros parámetros.

Finalmente, más que una técnica, fuimos capaces de aprovecharnos de la gran variedad de ratones genéticamente modificados existentes hoy en día en el mercado. Cruzamos nuestros ratones nulos para *Gdap1* con otros que presentaban sus mitocondrias marcadas (http://jaxmice.jax.org/strain/018397.html). La descendencia de estos cruces presentaba el alelo mutado para *Gdap1* y las mitocondrias marcadas. La obtención de estos ratones hizo posible estudiar la mitocondrias en movimiento en el mismo nervio ciático de los animales; sin necesidad de disgregación, cultivo y marcaje.

Introduction

1.- The disease of study: CMT

1.1.-History and clinical features of CMT

Hereditary peripheral neuropathies (HPN) include hereditary motor and sensory neuropathies (HMSN), hereditary motor neuropathies (HMN), hereditary sensory neuropathies (HSN) and hereditary sensory and autosomic neuropathies (HSAN). Despite this heterogeneity, HPN are a group of disorders that share characteristic clinical phenotypes that manifest as a peripheral neuropathy with a chronic progressive course. The most frequent entity, HMSN, also known by the eponym Charcot–Marie–Tooth disease (CMT), is a heterogeneous group of disorders which can be classified on the basis of their clinical, neurophysiological, genetic and pathological features. Charcot–Marie–Tooth disease is one of the most common degenerative disorders of the peripheral nervous system (Tazir et al. 2014). Nowadays, the prevalence of CMT disease is 40 cases per 100000 population in the United States, 28 per 100000 in Spain, 18 per 100000 in Italy and 11 per 100000 in Japan (Kedlaya 2014).

Historically, it was in 1886 when Professor Jean Martin Charcot (1825-1893) and his student Pierre Marie (1853-1940) published in Paris the first description of distal muscle weakness and wasting beginning in the legs, calling it ‘peroneal muscular atrophy’. At the same time in Cambridge, Howard Henry Tooth (1856-1926) described the same disease in his PhD dissertation, calling the condition ‘peroneal progressive muscular atrophy’. Tooth was the first to attribute symptoms correctly to neuropathy rather than to myelopathy, as physicians previously had done (Kedlaya 2014).

Currently, most cases of CMT are slowly progressive disorders that usually present in the second decade, although earlier or later initial presentations may occur depending on the underlying genetic abnormalities. The classical phenotype includes steppage gait, moderate distal sensory deficit, and distal lower amyotrophy giving an aspect of “jambes de coq” or an inverted champagne bottle. Other characteristical features such as decreased or absent deep tendon reflexes in distal symmetric pattern gait and balance impairment, because of proprioceptive loss and skeletal deformities that result in "pes cavus" and hammertoes, complete the typical CMT phenotype (figure I1). Moderate scoliosis may be part of this clinical phenotype. The severity of the neuropathy can be evaluated by a CMT neuropathy score, a nine-item clinical examination that measures sensory symptoms, motor symptoms, arm and leg strength and nerve conduction velocities.

Figure I1. Common foot deformities in Charcot–Marie–Tooth disease and related disorders. (A) Claw toes, (B) pes cavus and (C) hind foot varus deformities of the feet (Rossor et al. 2015).

The electrophysiological examination is the first important step in separating *myelinopathies* from neuronopathies or *axonopathies*. Nerve conduction studies allow a preliminary subtype classification into demyelinating, axonal or intermediate CMT forms. In most cases, motor nerve conduction velocity (MNCV) and compound muscle action potential (CMAP) amplitudes in the upper extremities are required since the lower extremity nerves often demonstrate absent responses. When the median MNCV is <38 m/s, CMT1 (*demyelinating* form) is diagnosed, whereas if the median MNCV is >45 m/s with the finding of decreased CMAP amplitude, decreased or absent median sensory nerve action potential (SNAP) and in general absent sural and peroneal SNAPs, CMT2 (*axonal* form) is diagnosed. Intermediate CMT (CMTI) is diagnosed if the median MNCV falls in the range of 25–45 m/s within the family. In addition to MNCVs subtype classification is also based on the pattern of inheritance. The myelin dysfunction variant of CMT, CMT1, and the axonal variant, CMT2, are autosomal dominant (AD) disorders, whereas CMTX is an X-linked disorder. In contrast, autosomal recessive CMT variants (AR CMT) are classified as CMT4 if they have demyelinating features and CMT2B or AR CMT2 if they have axonal findings (Tazir et al. 2014).

Autosomal dominant CMT are the most frequent forms of CMT in most European and North-American countries. AD CMT1 is the most common form, such that it accounts for more than 80% of patients with CMT attending an inherited neuropathy clinic. Most patients with AD CMT1 have the classical CMT phenotype. Neuropathological features include a significant reduction of myelinated axons and “onion bulbs” which are composed of several layers of basal lamina, connective tissue and Schwann cells (hypertrophic neuropathy) around thinly myelinated axons. Most of AD CMT1 patients have a mild to moderate disability although some of them have a marked handicap and end up in wheelchairs. Autosomal dominant axonal CMT (CMT2) is relatively frequent as it may represent about a third of all AD CMT cases. Most CMT2 patients have a classical CMT phenotype but with a wider range of age of onset. Moreover, sural nerve biopsy findings demonstrate axonal loss often with a cluster of regeneration(axonal sprouting), without pathological evidence of primary demyelination. Autosomal dominant intermediate CMT (DI CMT) is characterized by a classic, mild to moderately severe CMT phenotype, and median MNCVs overlapping those observed in CMT1 and CMT2, with a range from 25 to 50 m/s.

Autosomal recessive CMT disorders were once considered to be extremely rare. However, clinical and molecular investigations of CMT families with AR inheritance, originating from countries around the Mediterranean basin, in the Middle-East and in Europe are increasing. Most autosomal recessive CMT cases are characterized by earlier onset and more rapid clinical progression that results in more marked distal limb deformities such as pes equino-varus, claw-like hands, and sometimes major spinal deformities. Nerve biopsy studies in AR CMT1 demonstrate prominent demyelinating lesions responsible for marked secondary axonal loss along with subtype-specific myelin abnormalities, whereas in AR CMT2 myelinated fibres are severely reduced in number without evidence of demyelination and remyelination or of active axonal regeneration. Otherwise, severe to late onset autosomal recessive intermediate CMT diseases have also been reported.

X-linked CMT should be suspected when male-to-male transmission is absent on pedigrees and when males are more impaired than females. Four dominant and recessive X-linked CMT subtypes have been described to date (Tazir et al. 2014).

1.2.- Genes and molecular basis in CMT

The first CMT locus was mapped in 1982, and 30 years of genetic research has not only allowed the successful identification of 80 disease-causing genes (figure I2), but also pioneered the discovery of novel genomic mechanisms. Loci and genes for CMT and related peripheral neuropathies were initially identified using genetic linkage studies, positional cloning, or candidate gene approaches (Timmerman et al. 2014).

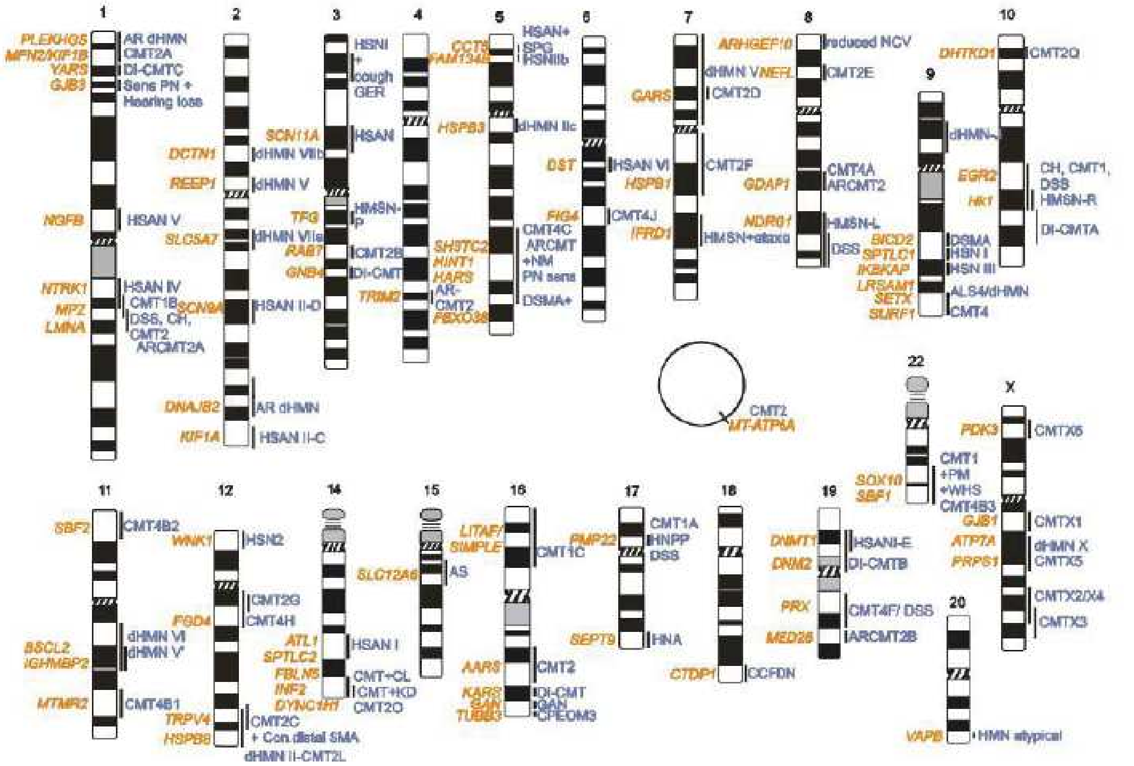

Figure I2. Genes and loci for Charcot-Marie-Tooth (CMT) and related inherited peripheral neuropathies. The figure shows 80 currently known genes (orange symbols) and their corresponding chromosomal loci (vertical bars). The corresponding phenotypes are indicated by blue symbols and are according to the disease nomenclature. Note that the disease names may not always correspond to information available in OMIM, GeneReviews, or in other publicly available databases. (Timmerman et al. 2014)

At the present time, mutations or rearrangements in *PMP22*, *GJB1*, *MPZ* and *MFN2* in the order of decreasing frequency account for about 90% of the molecular diagnoses in western populations (Sivera et al. 2013), while mutations in all other genes tested seem rare. Otherwise, most of the known CMT genes are strictly implicated either in axonal CMT or in demyelinating form, while some like *GDAP1*, *NEFL* and *MPZ* may be mutated in both forms. Some patients with Dejerine–Sottas syndrome (DSS) or congenital hypomyelination neuropathy (CHN) phenotypes may also share mutations in dominant or recessive genes such as *MPZ*, *PMP22*, *EGR2*, *GDAP1*, *MTMR2* or *PRX*. Moreover, gene mutations are mainly of dominant inheritance and others are recessive, while some of them such as *EGR2*, *P0*, *NEFL*, *MFN2*, *GDAP1*, and *HSPB1* mutations may be of both inheritance traits (Tazir et al. 2014).
(Extended table in the Appendix with CMT types, gene and phenotype, table A1)

Genes encoding proteins expressed in Schwann cells and neurons are linked to CMT, proteins that are involved in a wide range of processes: myelin assembly, cytoskeleton/axonal transport, protein aggregation, endosomal sorting, mitochondrial functions, mRNA processing/transcription, and ion channel transport (figure I3). When these proteins are mutated, various cellular processes are disrupted, thus resulting in CMT (Jerath & Shy 2014).

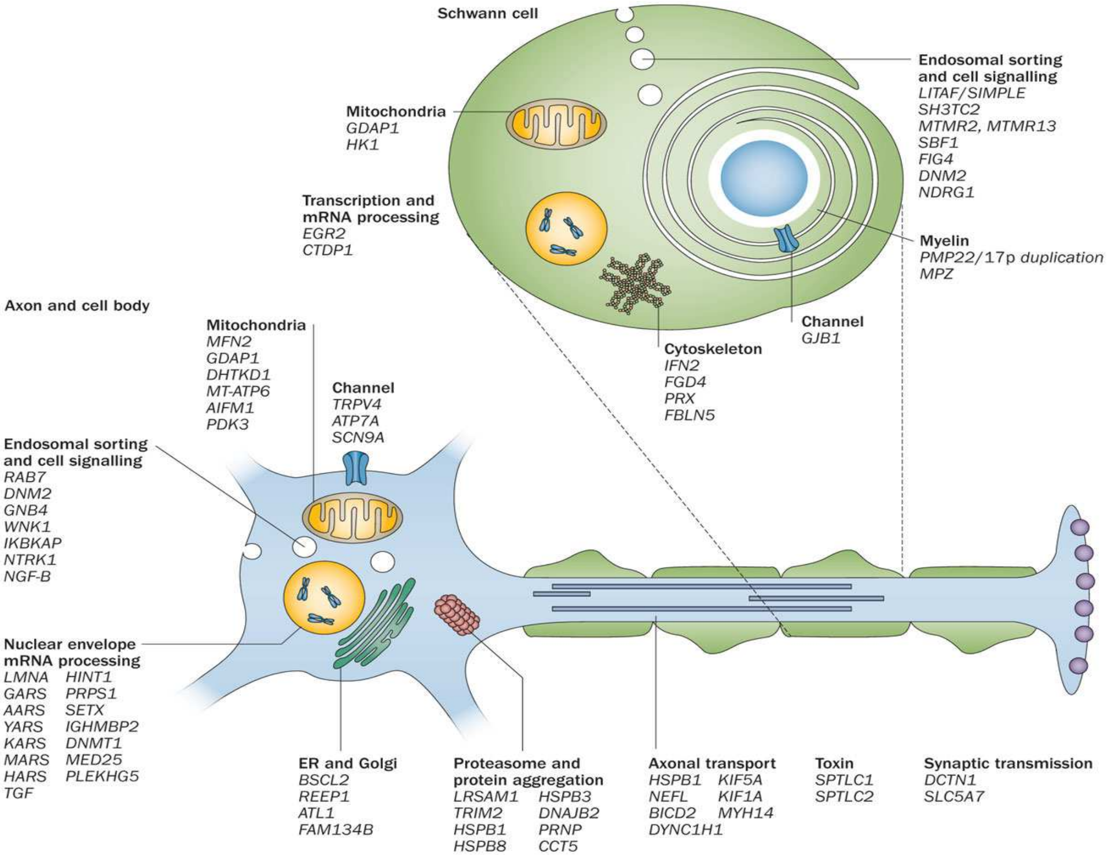

Figure I3. Known disease genes for CMT and related disorders, and their proposed pathomechanism. The figure shows all known genes and their involved cellular function, either in neuron or in Schwann cell (Rossor et al. 2015)**.**

Through this variety of genes and molecular processes, we can conclude that CMT disease pathophysiology of both the myelinopathy and axonopathy forms is the consequence of altered Schwann cell-axon communication; abnormal intercellular contact and signalling induce neurodegeneration and axonal loss, which ultimately produce muscular atrophy and weakness (Juárez & Palau 2012).

2.-The gene of study: *GDAP1*

2.1.- GDAP1-related CMT

Locus 8q13-q21 was linked to autosomal recessive CMT (CMT4A) with slow demyelinating presentation in four consanguineous Tunisian families in 1993 by the group of Dr Jeffery M. Vance. Several years later the same group identified the candidate gene, encoding *ganglioside-induced differentiation-associated protein-1* (*GDAP1*) (Baxter et al. 2002) and the group of Dr Francesc Palau also found an association of the *Gdap1* gene with axonal recessive CMT (AR-CMT2K) (Cuesta et al. 2002). This was the first time that same gene was linked with both demyelinating and axonal CMT (table I1).

CMT Type	Inheritance	Clinical presentation	Nerve/muscle pathology
CMT4A RI-CMTA AR-CMT2K	AR	Severe phenotype: early onset and rapid progression with proximal involvement, loss of ambulation; frequent vocal cord palsy	Axonal changes, secondary myelin abnormalities. No specific mitochondrial abnormalities found.
AD-CMT2K	AD	Variable onset, less severe course	Chronic axonal degeneration. Mitochondrial abnormalities reported.

Table I1. GDAP1 associated CMT types with clinical and neuropathologic phenotypes. Part of table 3 (Genes involved in mitochondrial dynamics, associated CMT types with clinical and neuropathologic phenotypes), here showing only GDAP1 associated CMT (Pareyson et al. 2015).

To date, 59 allelic variants has been already found in *GDAP1* (LOVD v.2.0 Build 36©2004-2014 Leiden University Medical Center) (see table A2 at the Appendix for details). 54 of these variants are pathogenic and link the gene with several types of CMT.

It is important to note relevant changes in CMT genetic distribution (table I2). A clear example of this is the predominance of *GDAP1* over *MFN2* in Spanish clinical series (Sivera et al. 2013). Indeed, there is a high rate of CMT patients in Mediterranean basin that have mutations in *GDAP1* in comparison with some other countries (Manganelli et al. 2014).

	Frequency, % (number of patients)				
	Manganelli et al. n = 197	Sivera et al. n = 404*	Gess et al. n = 589†	Murphy et al. n = 471‡	Saporta et al. n = 787
Country	Italy	Spain	Germany	UK	USA
Genes					
PMP22	72.3 (107)	56.1 (186)	69.9 (237)	69.0 (205)	65.0 (343)
GJB1	9.5 (14)	16.9 (56)	13.8 (47)	15.4 (46)	15.1 (80)
GDAP1	**5.4 (8)**	**12.7 (42)**	**0**	**0.6 (2)**	**1.1 (6)**
MPZ	4.7 (7)	5.7 (19)	6.1 (21)	4.3 (13)	8.5 (45)
SH3TC2	2.0 (3)	0.6 (2)	0	1.6 (5)	0.6 (3)
MFN2	1.3 (2)	1.2 (4)	3.5 (12)	4 (12)	4 (21)

Table I2. Comparison of genetic distribution in several series of patients depending on country. Percentages and numbers indicate the most common genes in series of Charcot-Marie-Tooth patients. *Caucasian cases only (excluded Gypsy cases). †Patients with sufficient nerve conduction studies. ‡Patients attending inherited neuropathy clinic;. #*PMP22* duplication, deletion, and point mutations. (Adapted from Manganelli et al. 2014).

2.2.-*GDAP1*

GDAP1 was previously identified as one of 10 cDNAs expressed in a differentiated Neuro2a mouse neuroblastoma cell line, in which cholinergic differentiation with neurite sprouting was induced by transfection of GD3 synthase (a2,8sialyltransferase) cDNA.

This gene, with a length of 23,728 base pairs (bp), contains six exons and five introns (figure I4). Two transcript variants of *GDAP1* have been identified. Transcript variant 1, representing the longer variant, encodes the longer isoform, designated as isoform "a" (358 amino acids). Transcript variant 2, encoding isoform "b", contains an alternative in-frame exon, uses an alternative splice site in the 5′ coding region, and a downstream start codon, compared to transcript variant 1. Isoform "b" (290 amino acids) has a shorter N-terminal region compared to isoform "a" (Cassereau et al. 2011).

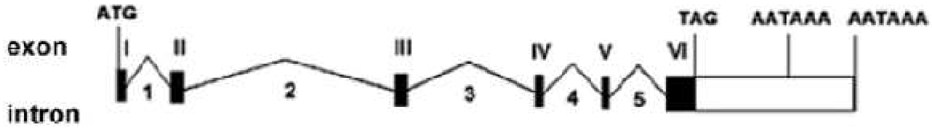

Figure I4. Molecular analysis of *GDAP1*. Diagram showing exon–intron structure. Exons are indicated by black boxes; exon 6 coding sequence is in black and the noncoding sequence is in white (Cuesta et al. 2002).

It was detected two GST domains analyzing the secondary structure (figureI5). Amino-acid residues 26–119 showed the βαβαββα topology of the glutathione (GSH) binding site, and amino-acid residues 210–287 (Cuesta et al. 2002). It has been also shown that GDAP1 has a single transmembrane domain (TMD) at the extremity of the C-terminal, and a hydrophobic domain (HD) in the flanking C-terminal region. Moreover, GDAP1 has two additional regions between amino acids 152–164 and 169–195 which are predicted to represent two helices, α4 and α5 (figure I6), creating the α4–α5 loop (Marco et al. 2004).

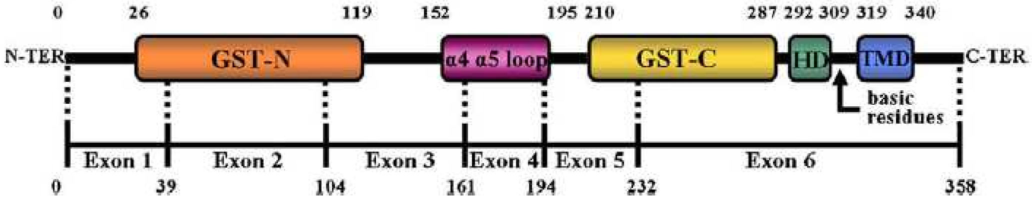

Figure I5. Schematic representation of the GDAP1 protein with predicted domains and the GDAP1 genomic organization with the corresponding exons. The numbering above the GDAP1 protein indicates the amino acid positions of the structural domains. The numbering below the genomic organization corresponds to the amino acid boundaries of each exon (Cassereau et al. 2011).

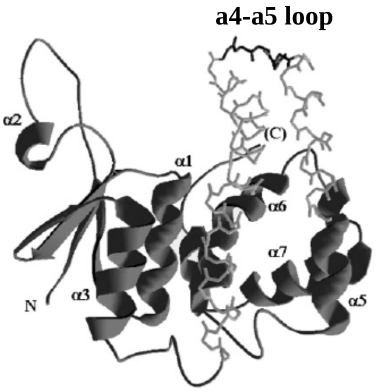

Figure I6. Predicted three-dimensional structure for human GDAP1 protein. The region presented as a backbone corresponds to part of the *Zea mays* GST used to model GDAP1 structure. This region (alpha helices 4 and 5 and loop between them) cannot be properly analysed for GDAP1 because of lack of sequence similarity. The region shown in black would correspond to the position of the GDAP1 a4-a5 loop, in the case that helices 4 and 5 conserve the same structure that is in canonical GSTs. N indicates N-terminal end. (C) indicates approximate position of the C-terminal end. (Marco et al. 2004).

GDAP1 expression studies show that mRNA is expressed in almost all the human and mouse tissues analysed but is most abundant in nervous tissues (Cuesta et al. 2002; Pedrola et al. 2005). Protein studies show GDAP1 expression not just in dorsal root ganglia (DRG) sensory neurons and motor neurons from anterior horn of spinal cord, whose axons are the site of pathology, but also in large neurons in the brain (Pedrola et al. 2008). Others authors also observed expression in myelinating Schwann cells (Niemann et al. 2005).

GDAP1 clearly appears to be localized in mitochondria, based on subcellular fractionation studies in human neuroblastoma cell line and overexpression experiments in fibroblasts. It has been also demonstrated that transmembrane domains are necessary for the correct localization of GDAP1 to mitochondria (Pedrola et al. 2005). Indeed, loss of GDAP1 signal after proteinase incubation and similar detection as porin after detergent treatment, demonstrate that GDAP1 is an outer mitochondrial integral membrane protein whose GST domains are exposed to cytoplasm (Niemann et al. 2005).

It has been clearly demonstrated that GDAP1 is a fission-inducing factor. Mouse neuroblastoma cell line experiments have revealed that overexpression of GDAP1 promotes mitochondrial fragmentation without inducing cellular apoptosis, changes in mitochondrial transmembrane potential or interfering in mitochondrial fusion. Moreover, transfections with *GDAP1*-specific RNAi led to an increase in the number of cells with a tubular mitochondrial morphology compared with untransfected or control transfected cells (Niemann et al. 2005). Additional studies, in human neuroblastoma cells, proved that *GDAP1* depletion induces a reduction in mitochondrial interconnectivity and an increase in organelle motility but without increasing tubular mitochondrial morphology (Pla-Martín et al. 2013). *GDAP1* dominant mutations cause a loss or reduction of fission activity, or interfere with mitochondrial fusion. Recessively inherited mutant forms of *GDAP1* display reduced fission activity compared to wild-type *GDAP1* (Niemann et al. 2009).

GDAP1-induced fission is dependent on Fis1 and Drp1. Unlike with other fission factors, GDAP1-induced fission does not increase the susceptibility of cells to undergo apoptosis (Niemann et al. 2009).

The amino-acid sequence of GDAP1 shows strong similarity to glutathione S-transferases (GSTs) (Cuesta et al. 2002). However, a measure of GST enzymatic activity using the model substrate 1-chloro-2,4-dinitrobenzene (CDNB), an electrophilic substrate used to study the kinetic properties of GSTs, did not confirm GST activity for GDAP1 without transmembrane domain. It remains possible that GST activity for GDAP1 requires a proper localization (Pedrola et al. 2005).

Recent experiments determine that *GDAP1* over-expression produced an increase of the total cellular GHS content and the mitochondrial membrane potential up to a level where it apparently limits mitochondrial respiration, leading to reduced mitochondrial Ca^{2+} uptake and superoxide production. The authors supported the hypothesis that the potential GST-GDAP1 is implicated in the control of the cellular GHS content and mitochondrial activity and the involvement of oxidative stress in the pathogenesis of *GDAP1*-related CMT (Noack et al. 2012).

In agreement, studies in human neuroblastoma cells proved that *GDAP1* depletion increase ROS loads according to hypothesis that lack of *GDAP1* causes oxidative stress. However, as these cells did not present alterations in mitochondrial electron transport chain complexes activity, it is unclear whether this oxidative stress has a mitochondrial origin (Bolinches Amorós 2014).

However, *GDAP1* dominants mutations lead to mitochondrial damage manifested in partial disturbance of the inner mitochondrial membrane potential (ΔΨm), increased reactive oxygen species (ROS) loads, and increased susceptibility to apoptotic stimuli. Recessively inherited mutant forms of GDAP1 do not induce this damage (Niemann et al. 2009).

Experiments in skin fibroblasts from AD-CMT2K patients conclude that the lower respiration rate due to impaired complex I activity reduces ATP production without decreasing the efficiency of oxidative phosphorylation. Mitochondrial energetic metabolism of AD-CMT2K fibroblasts revealed a functional impairment of mitochondrial complex I activity. In AR-CMT2K fibroblasts, the rate of ATP synthesis driven by complex I was reduced by as much as 50%. However, the rate of ATP production per unit oxygen consumption (ATP/O ratio) was normal in AD-CMT2K fibroblasts, indicating that the efficiency of oxidative phosphorylation was unaffected (Cassereau et al. 2009). The authors hypothesize that lack of ATP due to a Complex I deficiency could reduce mitochondrial mobility (figure I7), particularly in the distal portion of neuronal axons. Insufficient mitochondrial motility in the long axons might explain, at least in part, why the distal portions of the peripheral nerves are principally affected in CMT disease involving *GDAP1* mutations (Cassereau et al. 2011).

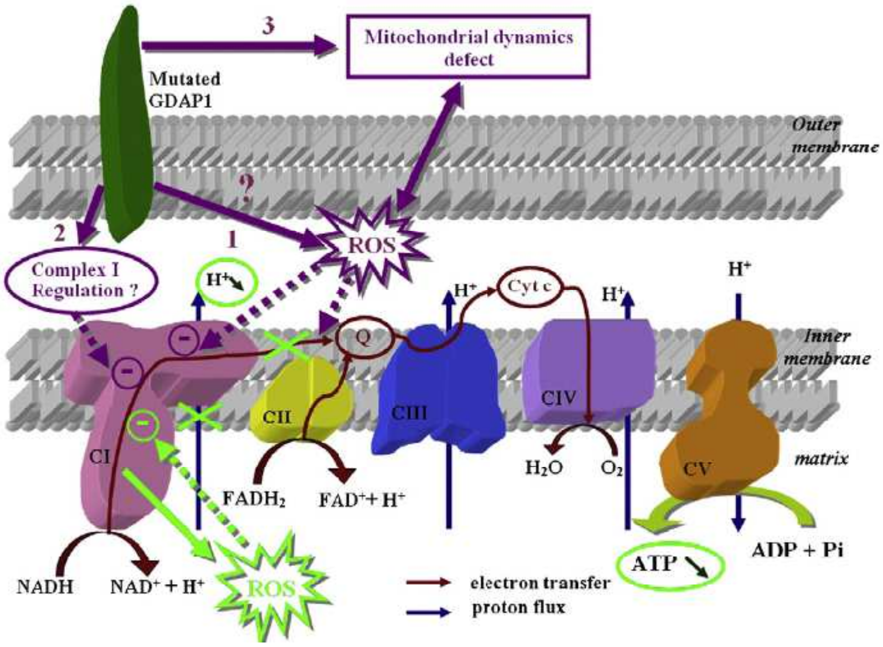

Figure I7. Schematic hypotheses evoked to explain the mitochondrial dynamics and bioenergetics defect in CMT4A/2K (purple dotted arrows) and consequences of the complex I deficiency (in green). 1: The mutated GDAP1 increases the ROS level which has a deleterious effect on lipid peroxidation, and on protein oxidation of complex I. 2: GDAP1 plays a role in complex I regulation involving the phosphorylation and/or acetylation pathways. 3: The mutated GDAP1 is responsible for a mitochondrial dynamics defect, either directly or through an increase of the ROS level. A deficit of complex I leads to a decrease in the reduction of NADH, altered electron transfer to complex III, a reduction of the pumping of protons into the intermembrane space, an excessive production of ROS and, finally, a reduction of ATP synthesis (Cassereau et al. 2011).

In addition, it has been suggested that GDAP1 may participate in mitochondrial movement within the cell. Human neuroblastoma cells experiments revealed that GDAP1 interacts with the trafficking associated proteins RAB6B and caytaxin and with β-tubulin. These authors hypothesize that GDAP1 may have a role in the movement of mitochondria towards the ER and mitochondria–ER interaction that may be relevant to the cellular pathogenesis of *GDAP1*-related neuropathies (Pla-Martín et al. 2013).

Others authors affirm that mitochondrial fission factor GDAP1 is also a peroxisomal fission factor. Loss of GDAP1 results in elongated peroxisomal morphologies, as the fission capacity is decreased, whereas overexpression promotes peroxisomal fragmentation. GDAP1-induced fission relies on the presence of mitochondrial fission factor (MFF) and dynamin-related protein-1 (DRP1), demonstrating that GDAP1 influences fission upstream of the conserved basic fission machinery of mitochondria and peroxisomes. To induce fission, the integrity of HD is essential in GDAP1 (Huber et al. 2013).

A relationship between Ca^{2+} and GDAP1 was also suggested. GDAP1 over-expression caused a decrease in cytosolic Ca^{2+} concentration (Noack et al. 2012) and its depletion caused an increase (Pla-Martín et al. 2013). More specifically, researchers conclude that *GDAP1* depletion ends in a failure to sustain store-operated Ca^{2+} entry (SOCE) upon mobilization of ER-Ca^{2+} due to an impaired SOCE-driven Ca^{2+} uptake in mitochondria. These authors propose that both the abnormal mitochondrial distribution and its impact in Ca^{2+} homeostasis could underlie the pathogenesis of *GDAP1*-related CMT disease (figure I8). Depletion of *GDAP1* may affect the proper mitochondrial network distribution, its relationship with the ER, and its positioning near subplasmalemmal regions which may impair the SOCE process and Ca^{2+} ER refilling (Pla-Martín et al. 2013).

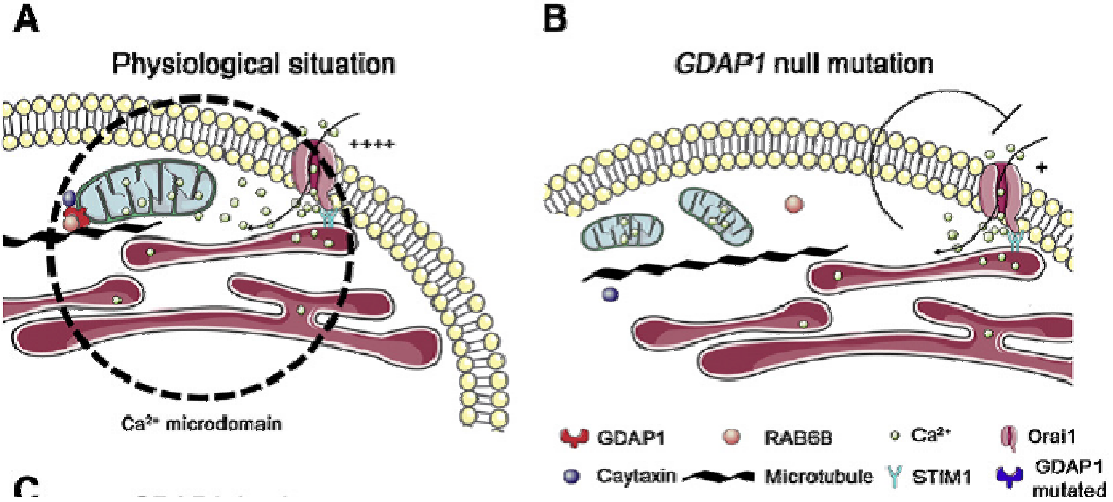

Figure I8. Proposed model for GDAP1 function. (A) The scheme shows GDAP1 participation in both retrograde and anterograde movements mediate d by RAB6B and caytaxin, respectively, which allows mitochondria to be positioned at Ca^{2+}microdomains between ER and plasma membrane. (B,) Mitochondrial movement might be affected by the absence of GDAP1 in the case of null mutations (Pla-Martín et al. 2013).

2.3.-*GDAP1* family: *GDAP1L1*

Phylogenetic analysis demonstrate that *GDAP1* belongs to a new group of GST-like proteins that is quite different from all other GST classes (GDAP1 class). Genes of this class, which includes human *GDAP1* and *GDAP1L1* (GDAP1like1) genes, are characterized by three main features. (1) Their distinctive sequences appear quite distant from all other GSTs in dendrograms (figure I9). (2) They have a characteristic additional amino acid region between predicted helices a4 and a5 (a4-a5 loop) that is absent in most GSTs. (3) They also have C-terminal extensions that may correspond to transmembrane domains. Those domains are absent in canonical GSTs, which, in general, are cytosolic enzymes. These studies also conclude that obvious orthologs of *GDAP1* exist in many vertebrate species. *GDAP1* paralogs, corresponding to the closely related *GDAP1L1* human gene and its orthologs, also are found in different vertebrates (Marco et al. 2004). *GDAP1* and *GDAP1L1* are most closely related to the Zeta, Omega and Theta GST classes but are unlikely to catalyse reactions with compounds that are known substrates for other previously studied GSTs (figure I9) (Shield et al. 2006).

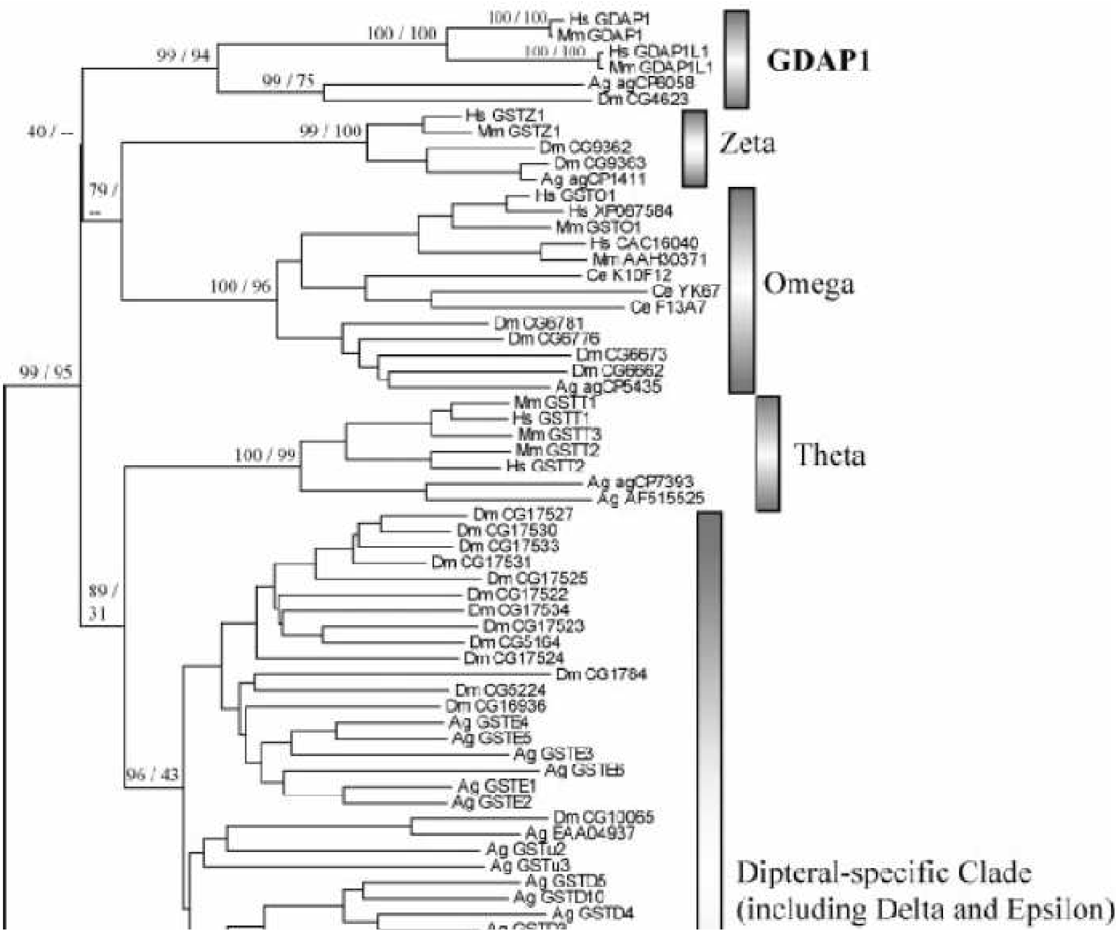

Figure I9. Unrooted NJ tree for GSTs of model animals (Hs: *Homo sapiens*, Mm: *Mus musculus*, Dm: *Drosophila melanogaster*, Ag: *Anopheles gambiae*, and Ce: *Caenorhabditis elegans*). Numbers refer to NJ and MP bootstrap values (Marco et al. 2004).

The chromosomal locus of *GDAP1L1* is 20q12. This gene, with a length of 33,818 base pairs, contains eight exons. Five to nine transcript variants of *GDAP1L1* have been identified depending on database. The most strongly supported isoform has 367 amino acids but all this information is based in sequences and predictions (ID 78997 in www.ncbi.nlm.nih.gov; ENSG00000124194 in www.ensembl.org; OTTHUMG00000032530 in vega.sanger.ac.uk). GDAP1L1 has a 56% amino acid sequence identity and 70% similarity with GDAP1(figure I10) (Shield et al. 2006).

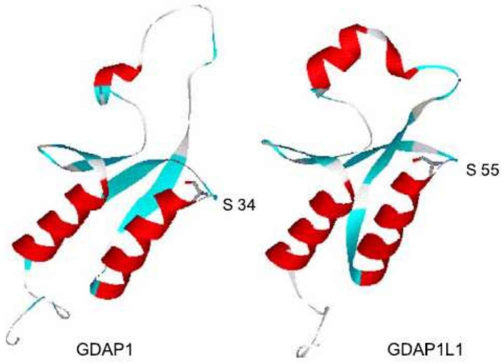

Figure I10. Homology modelled structures of the amino terminal thioredoxin-like domains of GDAP1 and GDAP1L1. The conserved active site serine positioned at the amino terminal end of helix 1 is shown in stick format (Shield et al. 2006).

Little has been published about *GDAP1L1*. In 2014 it was established that the *Gdap1l1* mouse ortholog is expressed in the CNS, but not in the PNS (Niemann et al. 2014). In addition, even if the murine ortholog is a cytosolic protein, GDAP1L1 can be translocated to mitochondria under stress conditions with increased oxidized glutathione concentration (Niemann et al. 2014). According to that Niemann et al. (2014) proposed that loss of GDAP1 is compensated by the mitochondrial translocation of GDAP1L1 in CNS.

3.-Peripheral nervous system

Peripheral neuropathy is a condition where damage resulting from mechanical or pathological mechanisms is inflicted on nerves within the peripheral nervous system (PNS). Damage can be located either on neuron's axons (axonopathy) or on Schwann cells surrounding its (myelopathy). In contrast to the central nervous system (CNS), the PNS possesses a unique ability to regenerate, recognized since the time of Camilo Golgi and Santiago Ramon y Cajal. However, despite the considerable capacity for regrowth upon injury, PNS regeneration is far from complete, especially in larger species such as humans, and functional recovery rarely returns to pre-injury levels (Richner et al. 2014).

The *peripheral nervous system* includes sensory receptors, sensory neurons, and motor neurons. Sensory receptors are activated by a stimulus that is converted to an electric signal and transmitted to a sensory neuron. Sensory neurons connect sensory receptors to the CNS that processes the signal, and transmits a message back to an effector organ through a motor neuron. The PNS has two parts: the somatic nervous system and the autonomic nervous system.

The *somatic nervous system* (voluntary) controls movements of skeletal muscles and enables humans to react consciously to environmental changes. It includes 31 pairs of spinal nerves and 12 pairs of cranial nerves (but not the optic nerve). Spinal nerves emerge from various segments of the spinal cord (figure I11) and it has a dorsal and a ventral root. The dorsal root contains afferent (sensory) fibres that transmit information to the spinal cord from the sensory receptors. Cell bodies of the afferent fibres reside in the Dorsal Root Ganglia (DRG). The ventral root contains efferent (motor) fibres that carry messages from the spinal cord to the effectors. Cell bodies of the efferent fibres reside in the spinal cord gray matter. These roots become nerves that innervate muscles and organs.

The *autonomic nervous system* (involuntary) maintains homeostasis automatically and without voluntary input. Its parts include receptors within viscera (internal organs), the afferent nerves that relay the information to the CNS, and the efferent nerves that relay the action back to the effectors. The effectors in this system are smooth muscle, cardiac muscle and glands, all structures that function without conscious control. The efferent portion of the autonomic system is divided into sympathetic and parasympathetic systems (www.pennmedicine.org 2001).

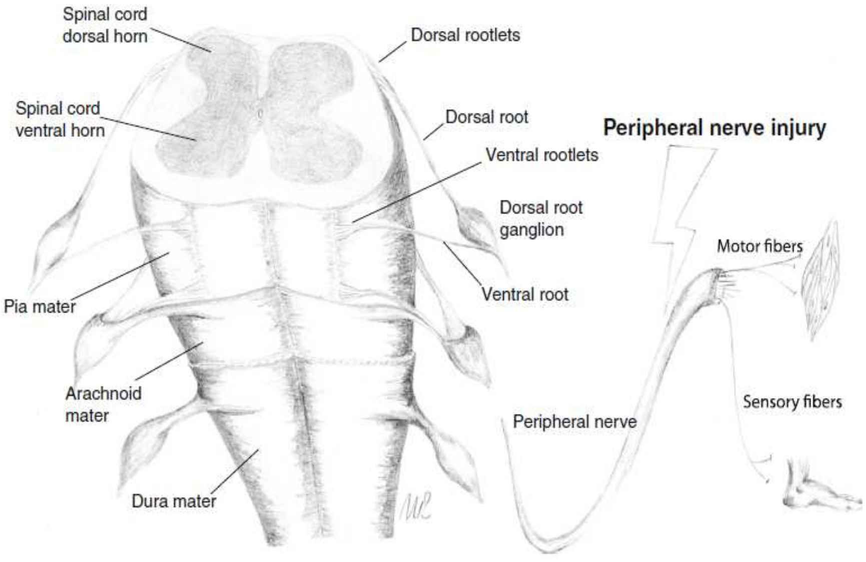

Figure I11. The spinal cord (CNS) and the peripheral nervous system (PNS). Peripheral nerve injury induces various changes in the PNS (peripheral nerve fibres and DRGs) but also in the central nervous system (CNS) (spinal cord) (Richner et al. 2014).

3.1- DRG

Dorsal Root Ganglia (DRG) neurons are primary afferent neurons responsible for transmitting sensory information from the periphery to the CNS. The DRGs are part of the PNS and are located in the neural foramen of the vertebrae, in close proximity to the CNS. For each cervical (C), thoracic (T), lumbar (L) and sacral (S) vertebra the DRGs are designated C, T, L or S and the corresponding number of the given vertebra in a rostro-caudal order (Richner et al. 2014).

DRG cell bodies are pseudo unipolar, with a peripheral and a central branch. The DRG contain many functional classes of sensory neurons (Smith et al. 2012). Sensory neuron types can be delineated by the expression of neurotrophic factor receptors, tropomyosin receptor-kinase A (TrkA), TrkB, TrkC, which serve as receptors for the neurotrophins (figure I12) (Lallemend & Ernfors 2012).

Nociceptive neurons are small, unmyelinated cells mediating pain sensation. They also express the TrkA receptor and respond to the neurotrophin NGF. Their central projections terminate largely in laminae I and II

Tactile mechanosensitive sensory axons are larger than nociceptive axons and are well myelinated. Peripherally they project via cutaneous nerves to a variety of specialized receptors in skin. Their central terminations are restricted to the dorsal horn but in deeper laminae than nociceptive axons, and these projections are arranged topographically, reflecting the specific area of skin they innervate peripherally. Many of these neurons express TrkB and respond to the neurotrophin BDNF.

The largest sensory neurons are *proprioceptive*, projecting peripherally via muscle nerves and supplying muscle spindles and Golgi tendon organs. They provide the CNS with information regarding body position and muscle length and tension. These neurons respond to the neurotrophin NT3 via TrkC receptors. Their central axons project to more ventral layers of the spinal cord than mechanoreceptors do, where they provide direct excitatory input to motoneurons (mediating the simple stretch reflex) as well as a variety of interneurons involved in locomotion (Smith et al. 2012).

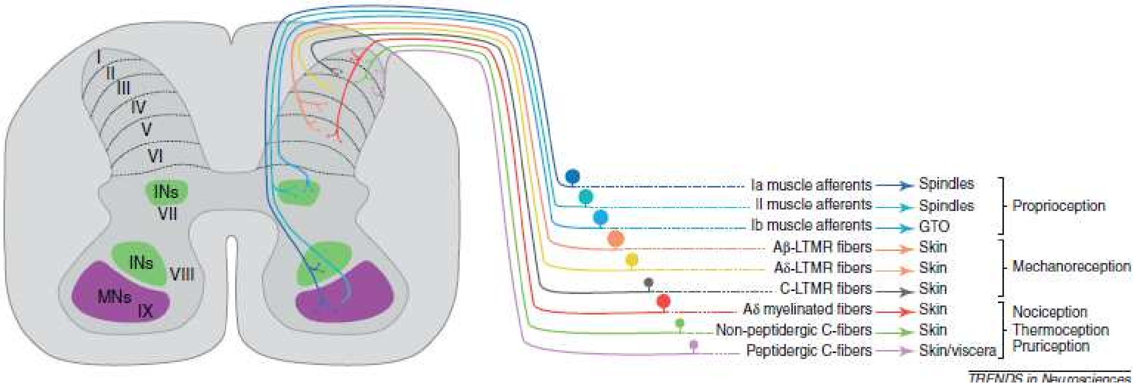

Figure I12. Central termination patterns of different classes of DRG neuron. The group Ia and some group II afferents that innervate muscle spindles (spindles) in the periphery project into the ventral spinal cord to connect motor neurons directly. Group Ib afferents (which innervate golgi tendon organs, GTO) as well as group II afferents, connect interneurons at the intermediate zone of the spinal cord. The C-, Aδ- and Aβ-low-threshold mechanoreceptors (LTMRs) project to the dorsal horn. Hence, C-LTMR endings terminate in lamina IIi and overlap with the Aδ-LTMR fibres that end partly within lamina II and mainly in lamina III. The Aβ-LTMR fibres terminate in laminae III through V. The Aδ myelinated fibres innervate laminae I and V and peptidergic and non-peptidergic neurons, laminae I and II. Nociceptive, thermoceptive and pruriceptive neurons are either unmyelinated (C-fibre) or lightly myelinated (Ad) sensory neurons. Peripherally, all types except types Ia, Ib and II afferents, innervate the skin and, unlike peptidergic neurons, non-peptidergic neurons terminate only in cutaneous fields and do not contribute to deep innervation of, for instance, viscera (Lallemend & Ernfors 2012).

3.2- Motor neuron

The human body has more than 300 bilateral pairs of muscles containing more than 100 million muscle fibres, which are innervated by more than 120,000 motor neurons (MN) in the spinal cord alone (Kanning et al. 2010).

Lower MN cell bodies are located in specific nuclei in the brainstem as well as in the ventral horn of the spinal cord and therefore, like upper MNs, have their soma within the CNS. The remarkable characteristic of lower MNs is their axonal extension connecting targets outside of the CNS. Lower MNs are cholinergic and receive inputs from upper MNs, sensory neurons (SNs) as well as from interneurons (INs). Paralysis is a typical clinical symptom of lower MN lesions since once damaged there is no alternative route to convey the information to the muscle targets in the periphery. Lower MNs are classified into three groups according to the type of target they innervate: (i) branchial, (ii) visceral, and (iii) somatic MNs.

Somatic MNs are located in the Rexed lamina IX in the brainstem and the spinal cord and innervate skeletal muscles responsible for movements. MNs form coherent groups connecting to a unique muscle target defined as MN pools. A motor unit defines a single MN together with all its axonal branches and all the muscle fibres it innervates. Interestingly, motor units are homogeneous: a MN innervates muscle fibres of a single type (figure I13).

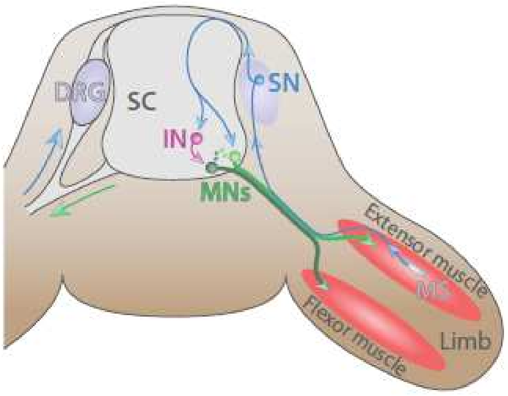

Figure I13. Schematic of a myotatic reflex illustrating the spinal cord (SC) circuitry. Sensory neuron (SN, blue) located in the DRG transmits a stretch stimulus sensed by the muscle spindle (MS, gray) to an interneuron (IN, purple) as well as directly to motor neurons (MNs, dark and light green). In turn, MNs stimulate the contraction of extensor muscle (red) and ensure the concomitant relaxation of the antagonist flexor muscle located in the limb (Stifani 2014).

Somatic MNs can be divided into 3 groups: (i) alpha, (ii) beta, and (iii) gamma according to the muscle fibre type they innervate to within a specific muscle target (figure I14) (Stifani 2014).

Alpha motor neurons, the most abundant and biggest, innervate extrafusal skeletal muscle and drive muscle contraction. Most α-MNs receive direct Ia input.

Gamma motor or fusimotor neurons innervate intrafusal muscle fibres of the muscle spindle and play complex roles in motor control.

Beta motor neurons, less well-defined population, innervates both intra- and extrafusal fibres (Kanning et al. 2010).

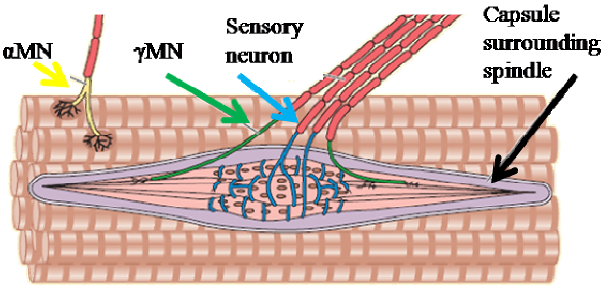

Figure I14. Schematic of muscle innervation. Longitudinal section of muscle fibres showing that αMN (yellow) innervates extrafusal muscle fibres, whereas γMN (green) connects to intrafusal fibres within the muscle spindle surrounded by the capsule. Sensory neurons (blue) carry information from the intrafusal fibres to the central nervous system (Adapted from Purves et al. 2004).

Neuromuscular junction.

The neuromuscular junction (NMJ) is a specialized synapse in the peripheral nervous system, which serves to achieve reliable transmission between the αMN and skeletal muscle fibres (Punga & Ruegg 2012).

The NMJ is composed of three compartments (figure I15):

(1) The presynaptic part – the motor nerve terminal – is responsible for synthesis, storage and release of the neurotransmitter acetylcholine (ACh).

(2) The intrasynaptic part – the synaptic basal lamina – constitutes a structural and functional extracellular matrix and facilitates adhesion between synaptic membranes.

(3) The postsynaptic part – the muscle membrane – contains a high density of acetylcholine receptors (AChRs) and other molecules important for the establishment and maintenance of the NMJ (Punga & Ruegg 2012).

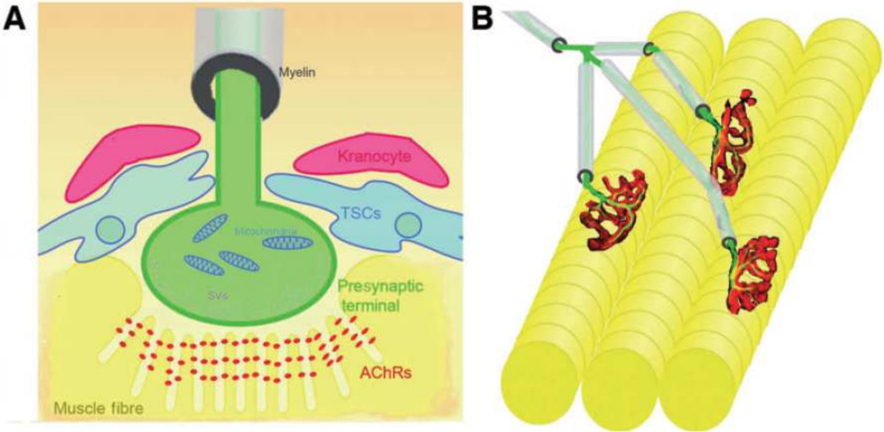

Figure I15. The mammalian neuromuscular junction (NMJ). (A) Schematic diagram illustrating cell types and organelles at the mammalian NMJ. The presynaptic motor nerve terminal are shown in green. Note the presence of large numbers of mitochondria. The post-synaptic muscle fibre is shown in yellow, with characteristic postsynaptic folds and clustering of acetylcholine receptors (AChRs; red). Terminal Schwann cells (TSC) are shown in blue and two NMJ-capping cells (kranocytes) are shown in magenta. (B) Schematic diagram illustrating the normal innervation pattern of three muscle fibres (yellow) in an adult mammalian muscle. Note how each muscle fibre is only innervated by a single axon (green; ensheathed by myelin shown in grey) at a single point of synaptic contact (red; AChRs). Also note how each presynaptic motor nerve terminal branches at the endplate resulting in a mirror image of the underlying AChRs (Murray et al. 2010).

Notably, the NMJ goes through a unique series of maturation processes that differ from those of the central synapse. First, whereas maturation of the central synapse normally occurs within hours, the NMJ takes days to weeks to refine its molecular and structural organization to achieve its mature form, which exhibits efficient neurotransmission. Furthermore, the stability of the NMJ increases on maturation, and the synaptic structure, once mature, persists throughout most of postnatal life, thus enabling life-long effective motor performance (Shi et al. 2012). There is, however some loss of NMJ innervation and reinnervation by axonal sprouting in ageing animals.

Due to the tight correlation between synaptic activity and NMJ morphology, a great deal of information can be gained about the functional status of motor neurons from analysis of NMJ morphology. As loss of NMJs frequently represents one of the first aspects of neuromuscular pathology, quantification at the level of innervation can give important information about the progression of pathology and the potential effect of a therapeutic intervention. Furthermore, as NMJ loss represents a significant step in pathological progression, the development of therapeutics that can stabilize connections and encourage regeneration may yield significant benefit (Murray et al. 2014).

4.- Mitochondrial dynamics in peripheral nerves

Peripheral nerves require efficient energetic metabolism to maintain their complex machinery and the transport of many molecular and organelle cargoes along axons, which may be as long as one meter. The highly specialised Schwann cell with many myelin lamellae wrapping axons also has to be maintained. Proper mitochondrial functioning is therefore fundamental for axonal and myelin formation and maintenance (Pareyson et al. 2015).

4.1.- Mitochondria in neurons

Mitochondria are organelles with an outer and an inner membrane (OMM, IMM). In the outer membrane porins forms large aqueous channels that make it permeable to molecules up to 5000 daltons, including small proteins. Such molecules can enter the intermembrane space which is chemically equivalent to the cytosol.

The major working part of the mitochondrion is the matrix and the inner membrane that surrounds it (figure I16). The inner membrane is highly specialized, it is selectively permeable to those small molecules that are metabolized or required by the many mitochondrial enzymes concentrated in the matrix. The matrix enzymes include those that metabolize pyruvate and fatty acids to produce acetyl CoA and those that oxidize acetyl CoA in the citric acid cycle. The principal end-products of this oxidation are CO_2, which is released from the cell as waste, and NADH, which is the main source of electrons for transport along the respiratory chain—the name given to the electron-transport chain in mitochondria. The enzymes of the respiratory chain are embedded in the inner mitochondrial membrane, and they are essential to the process of oxidative phosphorylation, which generates most of the animal cell's ATP. The inner membrane is usually highly convoluted, forming a series of infoldings, known as cristae, that project into the matrix (Alberts et al. 2007).

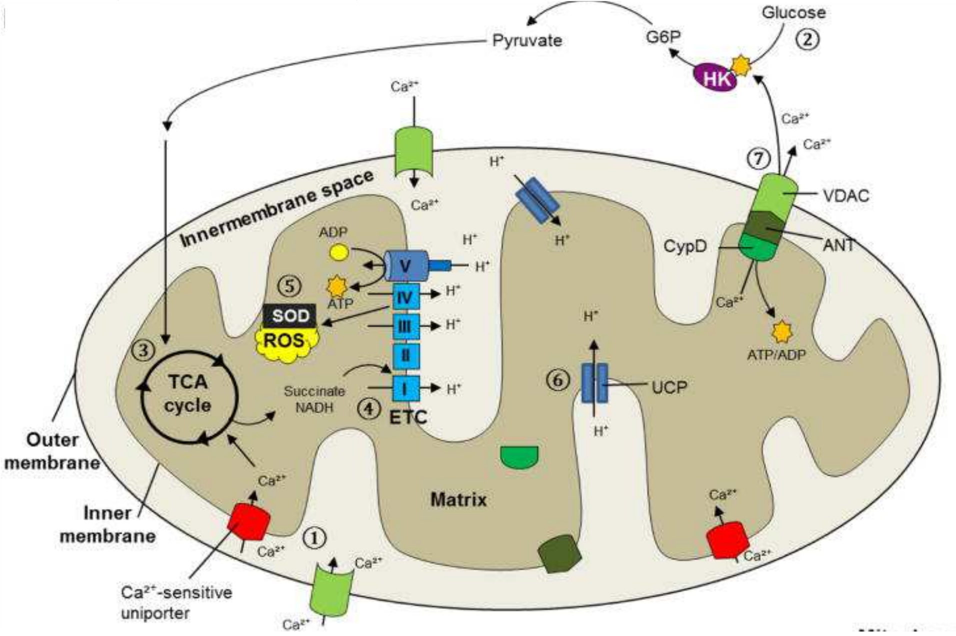

Figure I16. Mitochondrial function in normal cells. Under regular oxygen conditions, healthy cells primarily rely on mitochondrial OXPHOS for ATP production. 1) Ca^{2+} ions are taken up into a mitochondrion through VDACs and Ca^{2+}-sensitive uniporter channels, and stimulate ATP generation. 2) Glucose is converted into pyruvate during glycolysis which is 3) imported into the mitochondrion for entry into the TCA cycle. 4) Reduced succinate and NADH molecules are used by the ETC complexes to power ATP generation. 5) ROS created along the ETC are balanced by antioxidants, such as superoxide dismutase (SOD), and 6) UCP channels. 7) Excess Ca^{2+} ions are expelled from the mitochondrion through the MPTP comprised of VDAC, ANT, and CypD (Carlson et al. 2013).

Mitochondria are essential organelles for the life and death of eukaryotic cells and participate in oxidative phosphorylation; biogenesis of iron-sulfur clusters, heme, certain lipids, amino acids (Otera et al. 2013) and it targets signalling molecules including hydrogen peroxide and nitric oxide. Further, owing to their large capacity to store Ca^{2+}, mitochondria are crucial for Ca^{2+} buffering and are thus involved in numerous signalling pathways. However, mitochondrial Ca^{2+} overload can lead to neuronal apoptosis or necrosis (Sajic 2014).

The biosynthesis of mitochondria requires contributions from two separate genetic systems. The majority of the proteins in mitochondria are encoded by special genes devoted to this purpose in nuclear DNA. These proteins are imported into the organelle from the cytosol after they have been synthesized on cytosolic ribosomes. Other organelle proteins are encoded by mitochondrial DNA (mtDNA), consisting in many copies of small circular DNA anchored to the IMM, and synthesized on ribosomes within the organelle. In mammalian cells, mtDNA makes up less than 1% of the total cellular DNA. The human mitochondrial genome contains about 16,500 nucleotides and encodes 2 ribosomal RNAs, 22 transfer RNAs and 13 different proteins. Those proteins are subunits of Citochrome oxidase, ATP synthase and NADH dehydrogenase (Alberts et al. 2007).

Mitochondria proliferate by growth and division, thus their fusion and fission are important for maintaining mitochondrial number and function (Otera et al. 2013). Post-mitotic tissues such as components of the nervous system have the lowest capacity to maintain function following impairment of mitochondrial function, due to their limited capacity for self-renewal (Sajic 2014).

Furthermore, neurons are spatially complex cells with long axons, which renders the distant parts more liable to experience mitochondrial insufficiency than the majority of spherical or columnar cells. In neurons, as well as the standard cellular requirements, ATP is necessary for impulse conduction, as maintenance and post-impulse restoration of the membrane potential is dependent on the removal of Na^{+} ions by the Na^{+}/K^{+}ATPase. These great variations in impulse activity over time, thus the relative metabolic demands of central and peripheral components of the same neuron are constantly changing. Clearly, delivering mitochondria to areas of high metabolic demand (the right place) at the right time is essential, but should not be done at the expense of neglecting the cell body. Therefore, the long-distance two-way transport system for mitochondria in neurons is necessarily complex, receiving signals from several regions and "trying" to provide a sufficient supply to all areas simultaneously, including sites remote from the cell body. Indeed, with some cell processes more than one metre long in human, clearly the potential difficulties are compounded in that the very process of delivering energy has evolved into a major energy-requiring system in its own right (Sajic 2014).

4.2.- Mitochondrial fusion-fission

Mitochondrial dynamics define the continuous process of fusion and fission of these organelles, fundamental to regulate their shape, size and number, as well as the mitochondrial transport along axons, and the interactions with other organelles, such as the endoplasmic reticulum (ER) (Pareyson et al. 2015).

Fusion is the combination of two separate mitochondria into one and serves to mix and unify the mitochondrial compartment (Cagalinec et al. 2013). It is a two-step process whereby first the OMMs fuse, followed by fusion of the IMMs. At least one fusing partner needs to be mobile and move towards the other fusing partner. The probability that a mobile mitochondrion will get engaged in fusion with a stationary mitochondrion increases with the velocity of the moving partner. In other words, the greater the speed at impact, the higher the chance that the colliding mitochondria will fuse (Sajic 2014).
Mitochondrial fusion (Figure I17) is regulated by dynamin-like GTPases located both in the OMM, Mitofusin-1 (MFN1) and Mitofusin-2 (MFN2), and in the IMM, Optic Atrophy-1 (OPA1). MFN1 and MFN2 form homo- and hetero-oligomers in OMM of two mitochondria, determining their tethering in the fusion process. MFN1 interacts also with OPA1, important for the IMM fusion and cristae shaping (Pareyson et al. 2015).

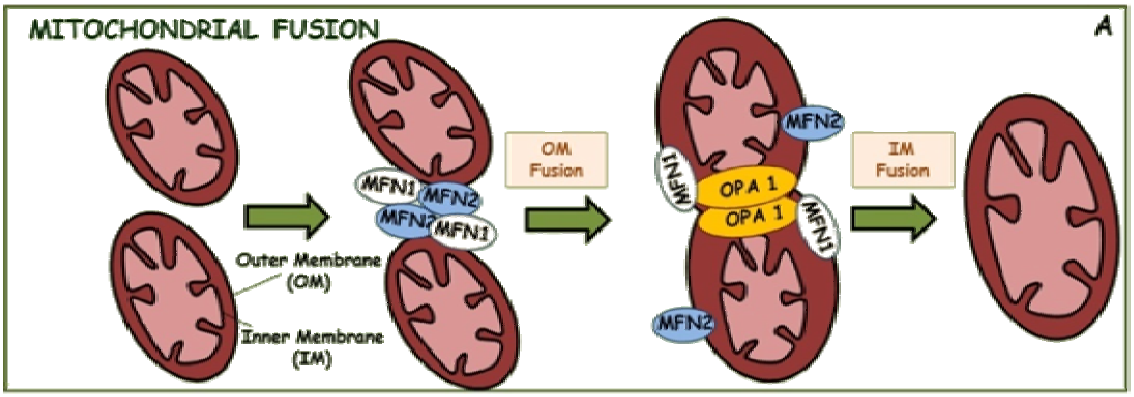

Figure I17. Mitochondrial fusion. In the mitochondrial fusion, two mitochondria next to each other come into contact and the mitofusins (MFN1 and MFN2) in the outer membranes (OM) of the two mitochondria tether them by forming homo- and hetero-dimers. The two OM fuse and then the inner membranes (IM) begin the fusion process which is mediated by OPA1, located in the IM, which interacts also with MFN1. After fusion of the membranes, the two mitochondria merge their whole content and at the end of the process one larger mitochondrion is obtained (Pareyson et al. 2015).

Fission generates morphologically and functionally distinct organelles (Cagalinec et al. 2013). Under basal physiological conditions, fusion is in equilibrium with fission in such a way that the distribution of mitochondrial sizes in cells is maintained relatively constant (Sajic 2014).
Mitochondrial fission is regulated by other proteins (Figure I18), including mitochondrial fission factor (MFF) and mitochondrial fission protein 1 (FIS1), acting in the OMM as ligands of a cytoplasmic multimeric GTPase, also related to dynamins, named DRP1 (dynamin-related protein-1) in mammals. GDAP1 participates possibly favouring the assembly of DRP1 (Pareyson et al. 2015).

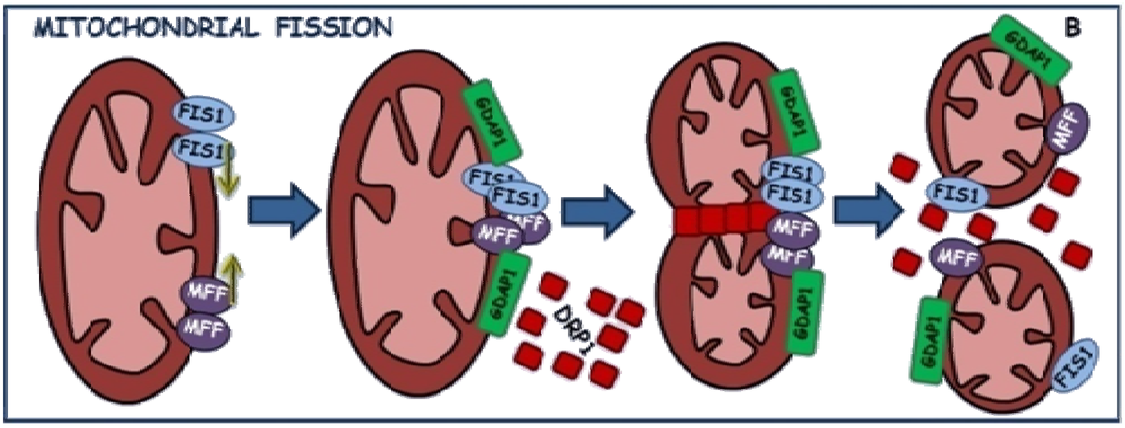

Figure I18. Mitochondrial fission. Fission of one mitochondrion leads to the formation of two novel mitochondria in a process which is less known. In the fission process, MFF and FIS1, in the OM, interact with the cytoplasmic multimeric protein DRP1, an important effector of fission. GDAP1 participates in OM (Pareyson et al. 2015).

The balance of these two processes determines organelle shape, size and number and is critical for organelle distribution and bioenergetics. The latter is particularly important in neurons, which have a unique bioenergetic profile due to their dependence upon energy from mitochondria and their specialised, compartmentalised energy needs. Beyond the control of morphology, the mitochondrial fusion-fission cycle appears to be also critical in regulating cell death and mitophagy. Mitochondrial fission contributes to quality control by favouring removal of damaged mitochondria via mitophagy and may facilitate apoptosis in conditions of cellular stress. Failure of mitochondrial fusion-fission dynamics has been linked to several diseases as CMT and other neurodegenerative diseases (Cagalinec et al. 2013).

4.3.- Mitochondrial transport in neurons

In motor and sensory neurons of the peripheral nervous system, mitochondria are particularly concentrated in defined regions: the initial segment of the axon stemming from the perikaryon, close to nodes of Ranvier, at distal sites close to the neuromuscular junctions (motor neurons) or to the sensory end terminals (sensory neurons), and at the site of any lesion (Pareyson et al. 2015). Approximately 30–40% of total mitochondria are in movement reflecting the acute need for buffering Ca^{2+} influx and distributing ATP among the microdomains inside neurons. A mitochondrion can either move continually over a long distance at a relatively constant speed, or pause sporadically and start again with a different speed or direction (Lovas & Wang 2013).

The neuronal cytoskeleton, which is composed of microtubules, actin filaments and neurofilaments, acts as a railway to transport mitochondria along neurons. The axonal flow is termed *anterograde* when directed toward the terminal end and *retrograde* when going backwards to the neuron's soma.

The majority of mitochondrial movement is microtubule-based (A-C in figure I19). Two principal motor proteins have been described. The kinesin family proteins transfer cargoes from the cell body toward the terminal end (anterograde), whereas dynein is preferentially involved in retrograde flow. Both protein families have a microtubule-binding domain with two branches and an ATP-hydrolyzing activity allowing a step-like movement; moreover, they use several adaptors and scaffolding proteins to recognize and bind cargoes (Pareyson et al. 2015).

The Miro-Milton complex is the best understood adaptor complex for the regulation of mitochondrial anterograde transport. The current model suggests that Miro functions as a receptor with a transmembrane domain integrated into the outer mitochondrial membrane, and Miro binds to Milton, which in turn binds to Kinesin Heavy Chain (KHC) (A in figure I19).

The adaptor proteins for retrograde movement of mitochondria are less clear; it seems that there is only one complex, dynactin, which binds to dynein and microtubules directly via its largest subunit, p150. Dynactin may facilitate the processivity of the dynein motor or its cargo binding (B in figure I19) (Lovas & Wang 2013).

Most of immobile mitochondria there are also bound to microtubules, which is regulated by syntaphilin (SNPH). SNPH serves as a docking protein (C in figure I19) (Ni et al. 2015).

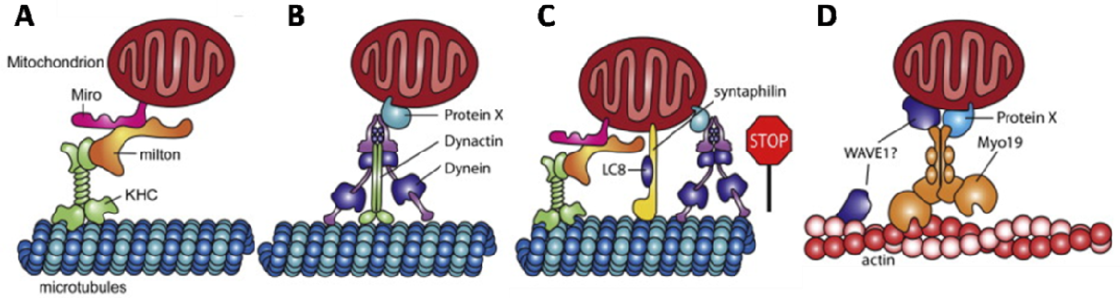

Figure I19. Schematic representations of mitochondrial transport machineries. A) Mitochondria are transported on microtubules by kinesin; Milton acts as an adaptor linking Kinesin Heavy Chain (KHC) to miro. B) Mitochondria are transported on microtubules by dynein; Dynactin act as an adaptor. C) mobile mitochondria stop once they bind to syntaphilin, while still being attached to motors and microtubules; dynein light chain, LC8, has been shown to be involved in this immobilization by stabilizing syntaphilin–microtubule interactions. D) Mitochondria are transported on actin filaments byMyo19; WASP family verprolin homologous protein 1 (WAVE1) regulates actin polymerization. "Protein X" indicates additional unidentified proteins on the outer mitochondrial membrane (Lovas & Wang 2013).

Mitochondria are also transported along actin filaments (D in figure I19), a process that happens more frequently in dendritic spines, growth cones, and synaptic button where the actin cytoskeleton is enriched. This actin-based movement is relatively short-range, likely mediated by myosin motors, and important for local and acute translocation and docking of mitochondria in response to action potentials, Ca^{2+} influx, or neurotrophic stimulation. Actin-based transport can also coordinate, supplement, or even oppose microtubule-based transport.

Although mitochondria are able to travel along actin, little is known of actin motors or their mitochondrial adaptors. As a motor, Myo19 has been described but it is still unknown if Myo19 binds to the mitochondrial membrane directly or via its binding partners. In addition, the WASP family verprolin homologous protein 1 (WAVE1) that regulates actin polymerization has been recently shown to control depolarization-induced mitochondrial movement into spines and filopodia and regulate spine morphogenesis (Lovas & Wang 2013).

The last component of neuron cytoskeleton, neurofilaments, are particularly abundant in axons and their main function is to control the axon diameter and thereby axonal conductance (Kevenaar & Hoogenraad 2015). Neurofilament network disruption can impair axonal architecture and axonal transport. Neurofilaments influence the dynamics of mitochondria too by regulating their arrest when detaching from molecular motors and microtubules, as stationary mitochondria appear to be bound to the "beams of the scaffold" NF-M and NF-H (C in figure I20) (Pareyson et al. 2015).

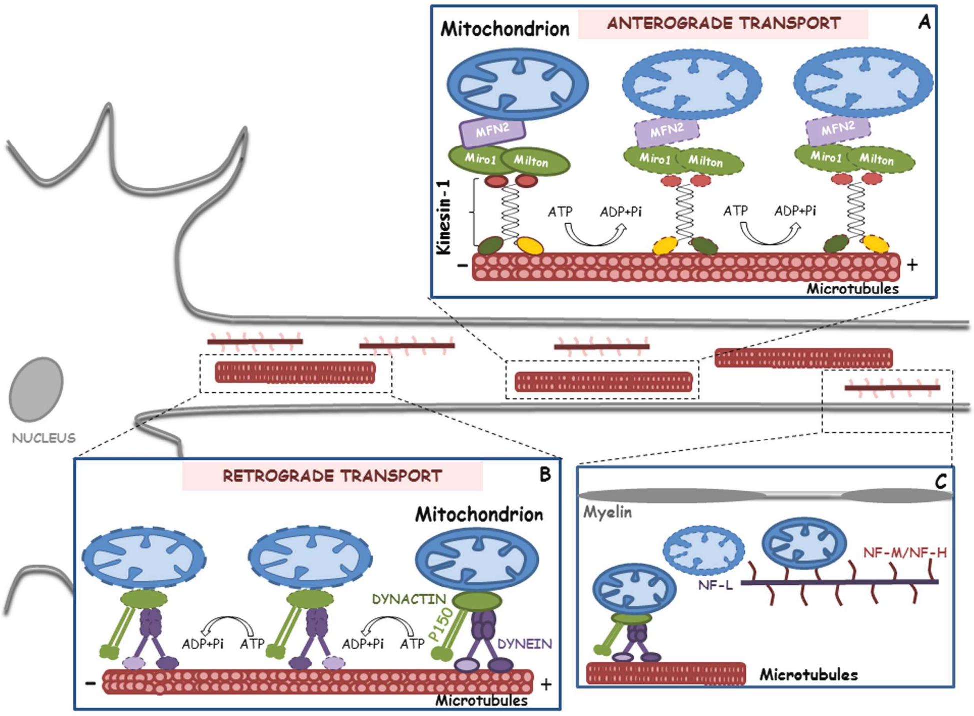

Figure I20. Axonal transport. The figure shows the anterograde and retrograde transport taking place in the axon of a neuron. The cytoskeletal architecture with the polarized microtubules and the neurofilament scaffold is represented. (A) Anterograde transport toward the terminal end is mediated by kinesins and kinesin-1 is the main mediator of mitochondrial anterograde transport. It steps along microtubules in an ATP-consuming process with its leg-like heavy chains and, through the adaptor Miro1-Milton complex bound to MFN2, transports the entire mitochondrion. (B) The dynein complex moves in the opposite direction (retrograde axonal flow) in the same step-wise ATP-consuming fashion. It ties the mitochondrion through dynactin and its important p150glued subunit. (C) Mitochondria move along the cells and are particularly concentrated in regions of high energetic demand, such as at the node of Ranvier. Stationary mitochondria are bound to neurofilaments (NF-M, NF-H) (Pareyson et al. 2015).

4.4.-Microtubules as railway of axonal transport

Microtubules are cylindrical polymers built up from α- and β- tubulin heterodimers, with a fast-growing plus-end and a more stable minus-end. These tubulin polymers switches stochastically between polymerization and depolymerization, a process called dynamic instability (Kevenaar & Hoogenraad 2015). In an axon, microtubules are uniformly arrayed with all plus-ends pointing to the axonal terminal and the minus-ends to the cell body, whereas in a dendrite their polarities are typically more mixed (Lovas & Wang 2013). Microtubules serve as tracks and different molecular complexes carry mitochondria along this railway. Polymerization of alpha- and beta-tubulin heterodimers confers a clear polarization, fundamental for properly directing axonal transport, as molecular motors preferentially move in a unique direction (Pareyson et al. 2015). Microtubules are uniformly arranged in axons: their plus ends are oriented distally and minus ends are directed toward the soma.

The dynamics of microtubules are regulated by a large number of factors, including microtubule-associated proteins (MAPs), motor proteins, post-translational tubulin modifications and plus-end tracking proteins (Kevenaar & Hoogenraad 2015).

There are post-translational tubulin modifications that makes microtubules more stable (figure I21). In migrating mammalian cells, subsets of microtubules that orient towards the leading edge are more stable and enriched in acetylation and detyrosination (Wloga & Gaertig 2010). In agreement, acetylation and detyrosination occurs on polymerized microtubules; deacetylation and retyrosination on depolymerised ones. Moreover, a preference of some kinesins for acetylated and detyrosinated microtubules has been reported (Janke & Kneussel 2010).

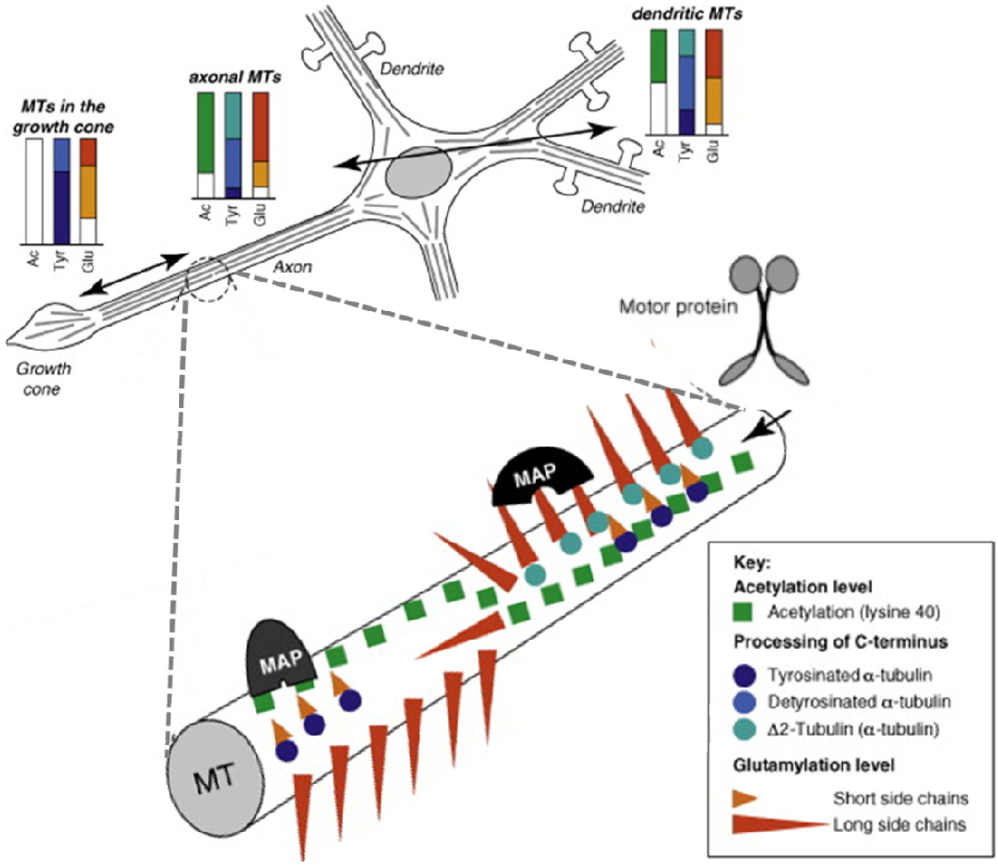

Figure I21. Microtubule cytoskeleton implications in axonal transport. Post-translational tubulin modification can regulate axonal transport by modulating motor proteins and microtubule-associated proteins (MAPs) linking to microtubules (Adapted from Janke & Kneussel 2010).

5.-Models to study CMT

5.1.- Mouse as a model of CMT

Owing to the rapid progress in animal genome engineering, mouse models of disease are experiencing tremendous development. There is a need for phenotypic characterization of the novel models including the morphologic approach. The small body size of this species requires specific technical solutions enabling the assessment of particular morphological features (Krinke et al. 2014). The characterization of mouse models of human disease is essential for understanding the underlying pathophysiology and developing new therapeutics. Many diseases are often associated with more than one model, and so there is a need to determine which model most closely represents the disease state or is most suited to the therapeutic approach under investigation. In the case of neurological disease, motor tests provide a good read-out of neurological function (Brooks & Dunnett 2009).

Peripheral nervous system in mouse.

PNS is guided by the same rules as in other species. In general, sensitivity is determined by the size of affected structures. Therefore, the sciatic nerve, the longest spinal nerve, is suitably represents the peripheral nerves. Axonal damage or “axonopathy” is “distally accentuated”, most prominent in the distal nerve branches; according to dying back theory, axons located distally from an injury undergo degeneration. Moreover, since the axons are maintained by axonal transport of materials supplied by the nerve cell body, and such transport to distal nerve branches needs to overcome long distances, the distal axonal portions most remote from the nerve cell body are most vulnerable.

In order to assess whether damage to nerve fibres is distally accentuated, the sciatic nerve must be collected and examined at least at two levels: proximally (above the knee)and distally in one of the main branches , e.g. the tibial nerve (below the knee). It is important to remark that the mouse sciatic nerve originates mainly from the third (L4) and fourth (L5) lumbar spinal cord segments (figure I22). The number of lumbar vertebrae in mice is variable, e.g. mostly five vertebrae occur in DBA/2J, mostly six vertebrae in C57BL/6J and a mix in B6129PFZ/J (Krinke et al. 2014).

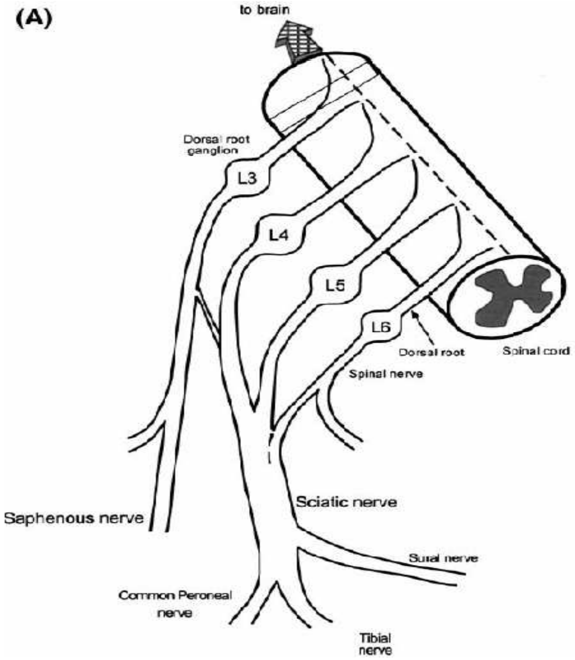

Figure I22. Image representing spinal cord, DRG and sciatic nerve in rat. Diagram of the sciatic and saphenous nerves, their terminal branches and their dorsal root origins showing that the saphenous nerve (femoral nerve plexus, L3 DRG) has minimal overlap with the sciatic nerve plexus (L4, 5 and 6 DRGs) (Decosterd & Woolf 2000).

Relationship between sciatic nerve branches and footpad innervation has also been established (figure I23). The saphenous nerve innervates the medial footpad while the tibial and sural branches of the sciatic nerve innervate the central and lateral parts respectively (Decosterd & Woolf 2000).

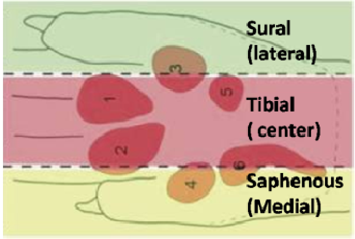

Figure I23. Different zones of the plantar surface of the rat paw innervated by the sciatic terminal branches and the saphenous nerve. At the borders between the skin territories some overlap of axonal terminals may occur (Decosterd & Woolf 2000).

Examination of the PNS reasonably includes samples of the skeletal muscle. In the mouse, the soleus muscle is type I (oxidative) predominant and quadriceps femoris or long digital extensor are type II (glycolytic) predominant. Like in other species, medial gastrocnemius muscle is considered to contain nerve fibres especially susceptible to toxic neuropathies (Krinke et al. 2014).

Analyzing NMJs, skeletal muscles of mouse can be subdivided into two subtypes, designated *Fast Synapsing* (FaSyn, like gluteus) and *Delayed Synapsing* (DeSyn, like gastrocnemius), muscles (figure I24). These muscles differ in the rate of neuromuscular synaptogenesis during embryonic development and in the maintenance of NMJs in the adult. In FaSyn muscles, a mature pattern is achieved within less than 1 day of development but, in DeSyn muscles, it requires 4–5 days. These differences in the timing and rate of synapse assembly appear to reflect muscle-intrinsic, nerve-independent programs of focal AChR clustering. In a DeSyn muscle (such as the soleus), focal AChR clustering and maintenance depends critically on nerve-derived factors, whereas this dependence is much more limited in FaSyn muscles. NMJs on FaSyn and DeSyn muscles continue to differ for several months after birth. Thus, after birth and up to 3–5 months of age, AChR clusters and presynaptic nerve terminals in DeSyn muscles are selectively vulnerable to the absence of nerve-evoked activity (Pun et al. 2002).

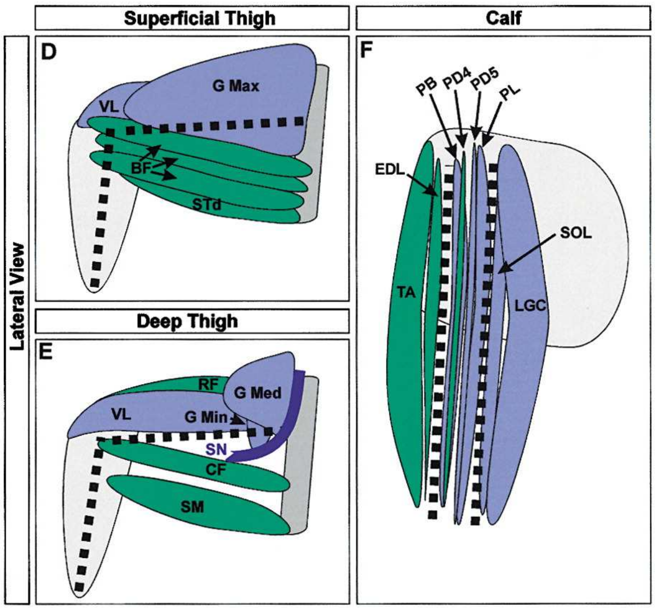

Figure I24. Distribution of FaSyn and DeSyn Muscles in the Hind limb of the Mouse. DeSyn muscles are in blue, and FaSyn muscles are in green. The dotted lines indicate positions of the bones. SN: sciatic nerve (E). Lateral (D–F) views of thigh (D, and E) and calf (F). Lateral views are subdivided into superficial (D) and deep (E). Thigh muscle abbreviations: BF, biceps femoris; CF, caudofemoralis; GMax, gluteus maximus; GMed, gluteus medius; GMin, gluteus minimus; RF, rectus femoris; Std, semitendinosus dorsal; SM, semi-membranosus; and VL, vastus lateralis. Calf muscle abbreviations: EDL, extensor digitorum longus; LGC, lateral gastrocnemius; PB, peroneus brevis; PD4, peroneus digitiquarti; PD5, peroneus digitiquinti; PL, peroneus longus; SOL, soleus; TA, tibialis anterior; (Pun et al. 2002).

Mitochondria labelling in mice

The co-evolution of optical *in vivo* imaging (or *in vivo* microscopy) and mouse genetics allows the investigation of neurological disease models in living animals at the level of single cells. Of particular importance was the generation of transgenic mice that express high levels of fluorescent proteins in their neurons. In these mice, neurons are labelled with different spectral variants of fluorescent proteins, which are expressed under the control of a modifiedThy1-promoter element (Misgeld & Kerschensteiner 2006).

More specifically, mice engineering has made possible the generation of a fluorescence labels to selectively image mitochondrial dynamics in the mouse nervous system, in both live mice and acute explants (figure I25). In vivo imaging of mitochondria is very useful tool to analyse this essential organelle (Misgeld et al. 2007).

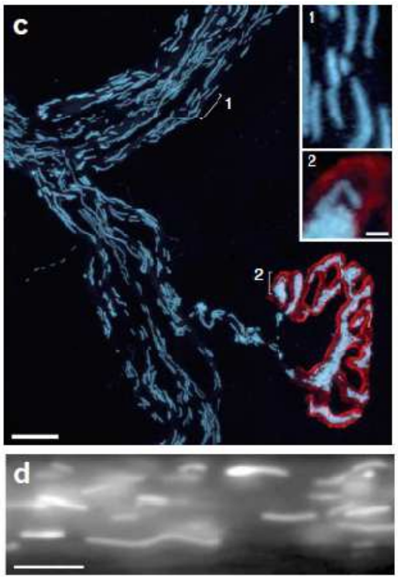

Figure I25. In vivo imaging of mitochondrial transport. (c) Peripheral motor nerve fascicle in a Thy1-mitoCFP-S mouse. Mitochondria align inside motor axons (inset 1), and a high density of mitochondria fills the terminal branches of neuromuscular junctions (inset 2; acetylcholine receptors labelled with a-bungarotoxin; red). (d) Time-lapse series of mitochondria in the proximal part of an intercostal axon in a nerve-muscle explant. An averaged still frame of the imaged axon segment (top), and the filtered and intensity-inverted version of the image (middle) are shown (Misgeld et al. 2007).

5.2.- Primary culture as a model of CMT

Cell culture is used by researchers worldwide to elucidate metabolic pathways and to discover the mechanisms involved in cell signalling, regulation of gene expression and protein synthesis, cell proliferation, senescence, and cell death. However, it must be noted that cells in culture are different from those *in vivo* in many ways. The normal extracellular matrix (which has important influences on cell morphology and function) is absent, as are other cell types that normally surround the cells in question and communicate with them (Halliwell 2014).

The formation of a complex nervous system requires microtubule-mediated processes that coordinate proliferation, migration, and differentiation of neuronal cells (figure I26). Therefore, it is not surprising that many neurodevelopmental problems and neurodegenerative disorders are caused by deficiencies in microtubule-related genes (Kapitein & Hoogenraad 2015). Use of primary culture allows us to study in depth several processes related with mitochondrial dysfunction: neurite initiation and outgrowth, axon elongation and regeneration, dendritic spine morphodynamics, synapse functioning and axonal transport.

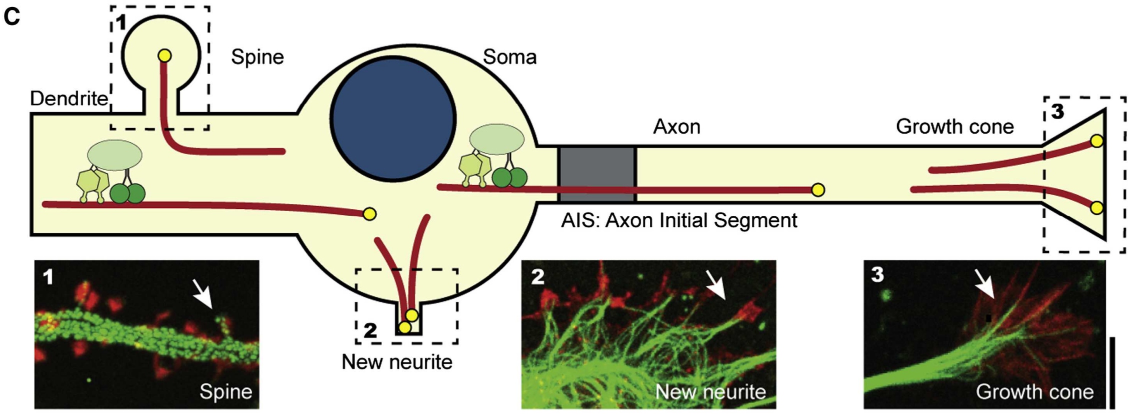

Figure I26. Neuronal microtubule, and their functions studied in cell culture. Cartoon illustrating the different functions of neuronal microtubules. Zooms show microtubule organization in dendritic spines (1), emerging neurites (2), and growth cones (3) of cultured rat hippocampal neurons. (1) Zoom of dendritic spines of neurons at DIV56 expressing the actin marker Lifeact (red) and the microtubule growth marker MT+TIP. For the MT+TIP, an overlay of 48 frames is shown to highlight the trajectories in the dendritic shaft, including spine entries. (2 and 3) Zooms of neurite formation (2) and a growth cone (3) from a cultured rat hippocampal neurons at DIV6, stained for tubulin (green) and actin (red). Arrows indicate overlap between the actin and microtubule cytoskeleton (Kapitein & Hoogenraad 2015).

Adult DRG primary culture.

Dorsal Root Ganglia (DRG) are a convenient source of neurons for studying the mechanisms of PNS development, growth, maintenance and disease *in vitro*. In addition, in peripheral neuropathies such as CMT, the possibility to culture affected cells and study disease progression can help to investigate the pathological mechanism. Evaluation of different parameters in DRG neuron cultures throughout the disease time course enables us to study disease progression.

DRG cultures often are used in neuron disease models as they are relatively easy to dissect, dissociate and maintain in culture (figure I27).

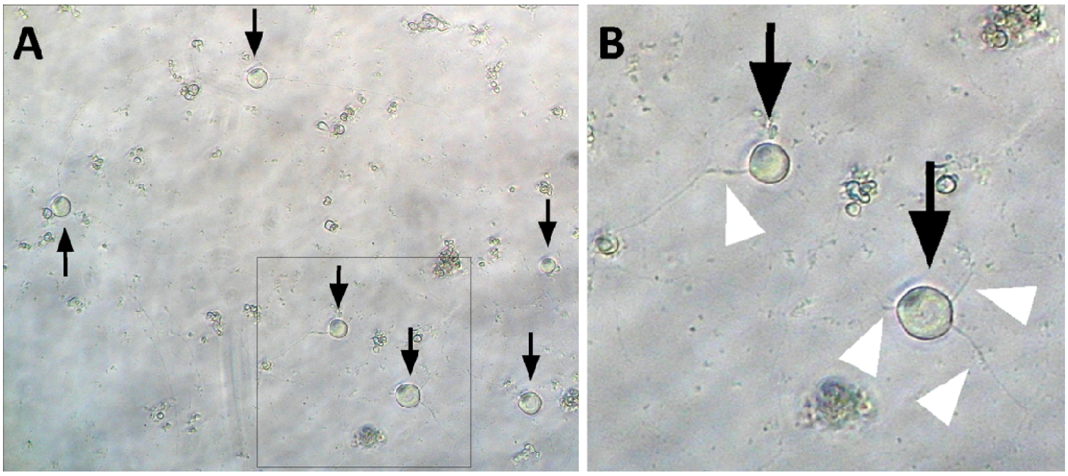

Figure I27. Adult DRG primary culture 5div. Representative image of DRG primary culture from 2 months old mouse after 4 days "in vitro" (div). Note that neuron soma appears as a bright spheres (black arrows) while neurites come out from soma as a thin processes becoming a neuronal net (white head arrows). B is a magnification of square drawn in A.

Postnatal SCG primary culture.

The rodent superior cervical ganglion (SCG) is a useful and readily accessible source of neurons for studying the mechanisms of sympathetic nervous system (SNS) development and growth *in vitro.* The SNS of early postnatal animals undergoes a great deal of remodelling and development; thus, neurons taken from mice at this age are primed to re-grow and establish synaptic connections after *in situ* removal. The stereotypic location and size of the SCG make it ideal for rapid isolation and dissociation (Jackson & Tourtellotte 2014).

Several techniques such as microinjection (figure I28) can be used to analyse mitochondrial movement in postnatal SCG culture (Gilley & Coleman 2010). To study mitochondrial movement there are many commercial markers. However, microinjection allows us to label only a few neurons in the dish and to know the orientation of individual axons.

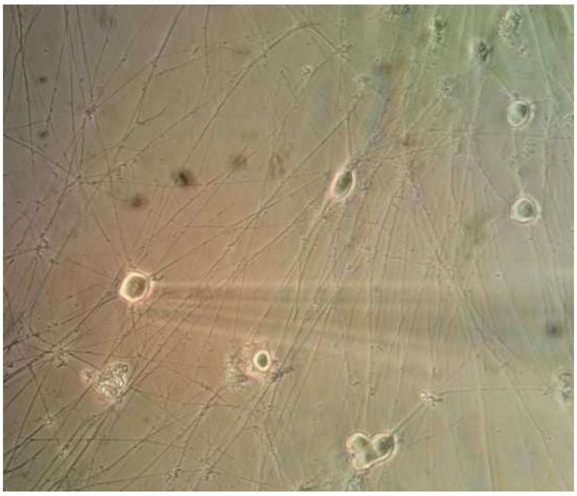

Figure I28. Postnatal SCG primary culture during microinjection. Representative image of SCG primary culture from P1 mouse after 4div. Note that neuron soma appears as a bright spheres while neurites come out from soma as a thin processes. Note also the shadow of microinjector pipette during microinjection of soma neurite.

Hypothesis & Objectives

Mutations in many genes cause Charcot-Marie-Tooth (CMT) neuropathy; and due to this a wide variety of subtypes and associated phenotypes has been described. *Ganglioside-induced differentiation-associated protein-1* (*GDAP1*) is one of these genes causing CMT, which is the special interest in Mediterranean basin due to the elevated frequency of CMT patients with mutations in this gene.

Despite previous studies in cell culture, the function of GDAP1 still unclear. It was initially described as a fission-inducing factor, but the molecular roles and pathogenic mechanisms in CMT disease remain undetermined.

Hypothesis

Based on cell culture studies and also the pathophysiology of CMT patients our hypothesis is that GDAP1 is implicated in mitochondrial transport and positioning within the neurons and axons. The disease pathology is due to impairment of transport and/or mislocalisation of mitochondria, which may be related to the nerve length.

Objective

The main objective of this thesis is to investigate the function of GDAP1 and understand its implications for CMT disease. For this purpose we have generated *Gdap1* null mice as a tool to investigate how the lack of gene function leads to neuropathy and to characterise the degeneration course.

As a first aim of this thesis, it is necessary to characterize our mouse and assess its suitability as a model for *GDAP1*- related CMT. Once this first goal is reached, we can use it as a tool to better understand the pathogenic mechanisms. A good mouse model for a disease should allow us to investigate the molecular changes occurring in all mouse tissues because of the mutated gene, so we are not limited to cell culture. Discovering the function of GDAP1 and understanding its implications for neuropathy may help make it possible to prevent or repair axon loss in CMT patients.

Thus, the main objective comprises 3 goals:

(1) Characterization of the *Gdap1* null mice
(2) Consolidate *Gdap1* null mice as a CMT model
(3) Determine the function of *GDAP1* and understand its implications for CMT disease

Results

1.- Mouse model characterization

A knockout mouse for *Gdap1* (*Gdap1*$^{-/-}$) was generated by genOway (Lyon, France; see Materials&Methods for more details), deleting exon 1 of murine *Gdap1*. Briefly, embryonic 129sv stem cells were transfected with a FRT-recombinase plasmid which also contains a homologous region to the first of six exons of *Gdap1* and a neomycin resistance gene. Recombined cells were then injected into blastocyts to create chimera mice. Chimeras were crossed with Flp recombinase-expressing C57BL/6J to remove the Neo resistance cassette and generate a line of Neo-excised floxed mice. *Gdap1*$^{+/flox}$ mice were crossed with ubiquitous Cre deleter mice to obtain constitutive *Gdap1*$^{+/-}$strains (figure R0).

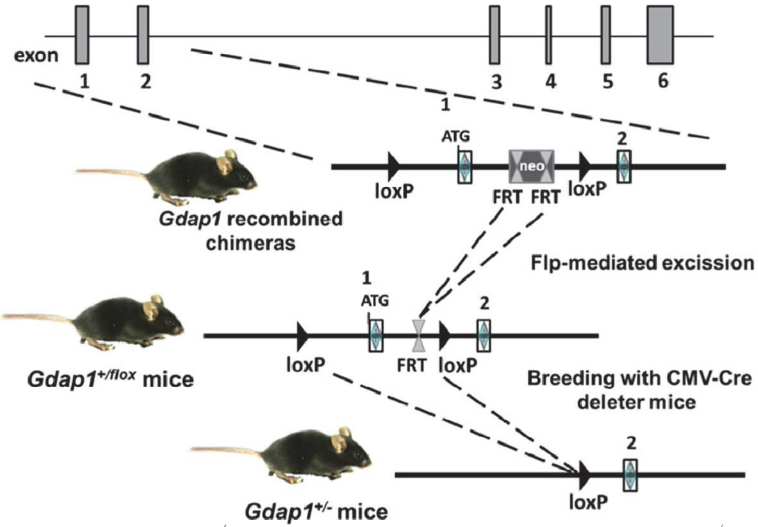

Figure R0. Generation of *Gdap1*$^{-/-}$mice. Schematic representation of *Gdap1*$^{-/-}$ targeting strategy. Diagram is not to scale. Hatched rectangles represent Gdap1 exons 1 to 6, solid line represents mouse chromosome 1. FRT sites are represented by double triangles and loxP sites are right-faced triangles.

Gdap1$^{+/+}$, *Gdap1*$^{+/-}$ and *Gdap1*$^{-/-}$ mice were born as offspring of *Gdap1*$^{+/-}$ breeding. All three genotypes were born at expected Mendelian ratios, had normal life span and were fertile. Knockout (*Gdap1*$^{-/-}$) mice pathology was compared with that of CMT patients and wild type (*Gdap1*$^{+/+}$) mice were used as controls.

1.1- Genetic and protein characterization

Genotyping was performed by PCR analysis of mouse genomic DNA obtained from tail biopsies. A PCR strategy allowed us to distinguish *Gdap1*$^{+/+}$, *Gdap1*$^{+/-}$ and *Gdap1*$^{-/-}$ by identifying the deleted gene as a shorter amplified product(
Figure R1).

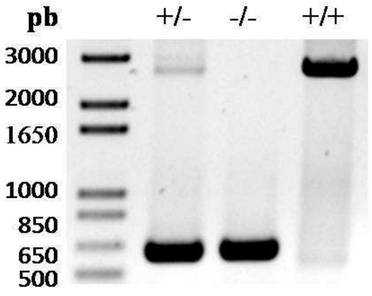

Figure R1. *Gdap1* genotyping. PCR strategy 2 is able to differentiate *Gdap1*$^{+/+}$ (2500pb), *Gdap1*$^{-/-}$ (550pb) and *Gdap1*$^{+/-}$ (both bands 2500 and 550pb).

Protein expression of GDAP1 was characterized in adult *wild-type* mouse tissue lysates (Figure R2). The expected band (37kDa) was only detected in brain, cerebellum, medulla, spinal cord and dorsal root ganglia. Total amount of loaded protein was not enough to detect its expression in sciatic nerve. The other tissues tested were negative to GDAP1 detection.

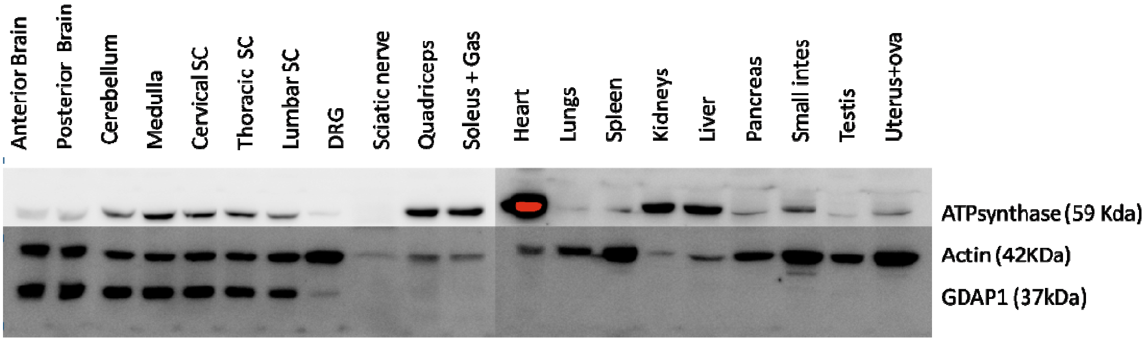

Figure R2. GDAP1 expression in wild type adult mice. Protein expression study in neuronal and non neuronal tissues: anterior brain, posterior brain, cerebellum, medulla, cervical spinal cord, thoracic spinal cord, lumbar spinal cord, dorsal root ganglia (DRG), sciatic nerve, quadriceps, soleus&gastrocnemius, heart, lungs, spleen, kidneys, liver, pancreas, small intestine, testis, uterus&ovarius. Actin was used as a housekeeping, ATP synthase as a mitochondrial marker and anti-GDAP1 (Abnova) for GDAP1 detection.

Loss of GDAP1 according on genotype was confirmed by western blot of neuronal and non-neuronal tissue lysates from *Gdap1*$^{+/+}$, *Gdap1*$^{+/-}$ and *Gdap1*$^{-/-}$ littermates (Figure R3). In these experiments we loaded more amount of protein so we could detect GDAP1 expression even in low-expression tissues such as sciatic nerves.Neuronal tissues were positive to GDAP1 expression and protein expression decreased in *Gdap1*$^{+/-}$ when it was compared with *Gdap1*$^{+/+}$.

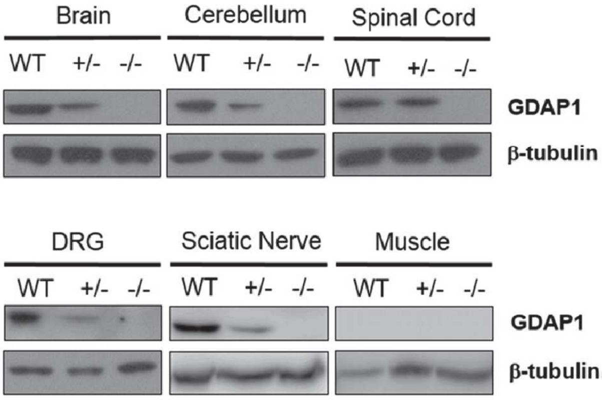

Figure R3. GDAP1 expression according on genotype. Protein expression study in neuronal and non neuronal tissues from *Gdap1*$^{+/+}$ (WT), *Gdap1*$^{+/-}$ and *Gdap1*$^{-/-}$ littermates. β-tubulin was use as a housekeeping and anti-GDAP1 from Abnova for GDAP1 detection.

In order to confirm the absence of protein expression in our mouse model we used three different commercial antibodies against GDAP1. Here we show another example of the lack of GDAP1 in *Gdap1*$^{-/-}$mice (Figure R4). In this case, a different antibody was used to test protein expression in *Gdap1*$^{+/+}$ and *Gdap1*$^{-/-}$mice tissues in comparison with neuroblastoma SH-SY5Y cell line (Pla-Martín et al. 2013). In contrast to the previous antibody (from Abnova), for which the immunogenic sequence was amino acids 158 to 267, this second one (from Sigma) covered amino acids 141 to 283.

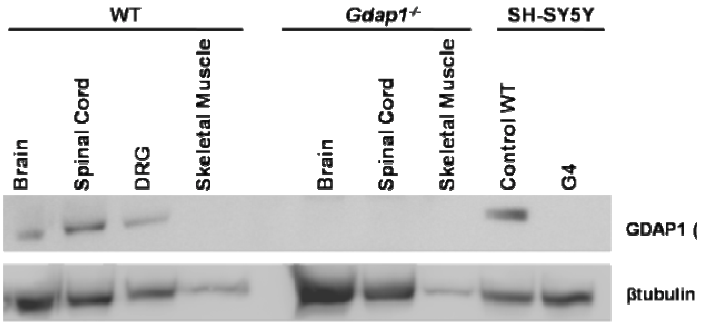

Figure R4. GDAP1 expression in *Gdap1*$^{+/+}$ and *Gdap1*$^{-/-}$ mice tissues. Protein expression study in *Gdap1*$^{+/+}$ (WT) and *Gdap1*$^{-/-}$ mice tissues in comparison with human neuroblastoma SH-SY5Y control and G4 cell line (Pla-Martín et al. 2013). Note that G4 cell line is a *GDAP1* knock-down cell model in SH-SY5Y cells. β-tubulin was used as a housekeeping and anti-GDAP1from Sigma for GDAP1 detection.

*Gdap1l1*expression.

*Gdap1l1*is a paralogue gene of *Gdap1* (Marco et al. 2004). Murine GDAP1L1 shows 58% of identity with GDAP1 (88% covered), although at nucleotide level this similarity (66%) just reaches 18% covered. However, there is still a possibility that the paralogue assumes *Gdap1* function (Niemann et al. 2014). To investigate these phenomena, we also analysed *Gdap1l1* expression in neuronal mice tissues from our mice model.

No differences were observed between WT and *Gdap1*$^{-/-}$ mice regarding *Gdap1l1* expression at RNA level detected by RT-PCR (Figure R5). We determined that *Gdap1l1* was expressed mainly in brain but not in DRG. The same RNA samples were used to confirm the expression of *Gdap1* (Figure R5). Even though there was a weak band in spinal cord of *Gdap1*$^{-/-}$, it is so poor after all PCR cycles.

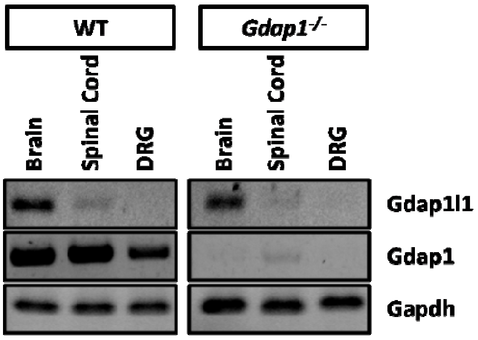

Figure R5. *Gdap1l1* and *Gdap1* expression by RT-PCR in *Gdap1*$^{+/+}$ (WT) and *Gdap1*$^{-/-}$ mice tissues. Primers design is described at Materials&Methods section. Gapdh, was used as housekeeping gene.

1.2- Phenotypic characterization of *Gdap1*$^{-/-}$ mice

CMT-related hallmarks.

The clinical hallmarks of CMT include distal muscle weakness and wasting, loss of proprioception and pinprick sensation and a classical steppage gait with foot deformities, such as pes planus or cavus. The age of onset can vary from infancy to late adulthood with clinical severity ranging from mild to severe (Brennan et al. 2015). The severe recessive form of *GDAP1*-related CMT starts early in infancy or childhood with weakness and wasting of the feet followed by involvement of the hands leading to pronounced disability. Patients are usually wheelchair bound starting from the second decade of life (Sevilla et al. 2008). Based on that we decided to compare motor behaviour in *Gdap1*$^{-/-}$ and WT mice at the early adult age.

We started with the observation of the mice into the cage and we detected an abnormal low position during locomotion in knockout mice (Figure R6, left upper images).We also noticed dragging tail in comparison with wild type animals (Figure R6, left upper images). Both hallmarks are indicators of distal muscles weakness (Wiethölter et al. 1990). However, the penetrance was not complete and not all the knockout mice presented the same phenotype.

Furthermore, we observed abnormal hind-limb clasping reflex in 3 months-old *Gdap1*$^{-/-}$ mice. When lifted by the tail, control mice responded normally, by extending their hind limbs and body, but *Gdap1*-deficient mice flexed their legs to the trunk or tightened the back limbs to their bodies (Figure R6, left down images). This abnormal reflex has been attributed to motor deficits (Rogers et al. 2001).

In addition, several 6 months-old and older *Gdap1*$^{-/-}$ mice presented pes planus or cavus in one or both of their hind limbs (Figure R6, right image).

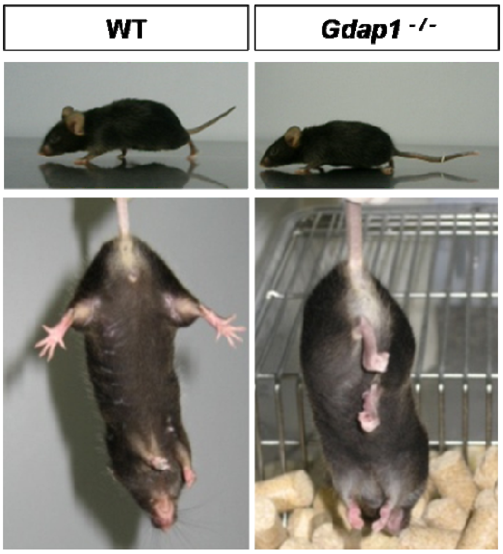

Figure R6. Representative images of control and *Gdap1*$^{-/-}$ phenotype. In the left upper images we can compare the body position of both genotypes mice while they are walking; note that *Gdap1* deficient mouse has a lower position of the body. In the left down panel we can compare the mice behaviour when they are hold by the tail; note that control mice try to rely on some structure with the hind limb while deficient mouse shrinks them. In the right image we can see a 8 months old *Gdap1*$^{-/-}$ that show a pes cavus like phenotype in the right hind limb

Despite all these motor alterations, *Gdap1*$^{-/-}$ mice had a normal lifespan, and no others problems were detected in appearance and behaviour or breeding. Weight differences were not significant until 16 months when *Gdap1*$^{-/-}$ mice became overweight in comparison with wild type (Figure R7).

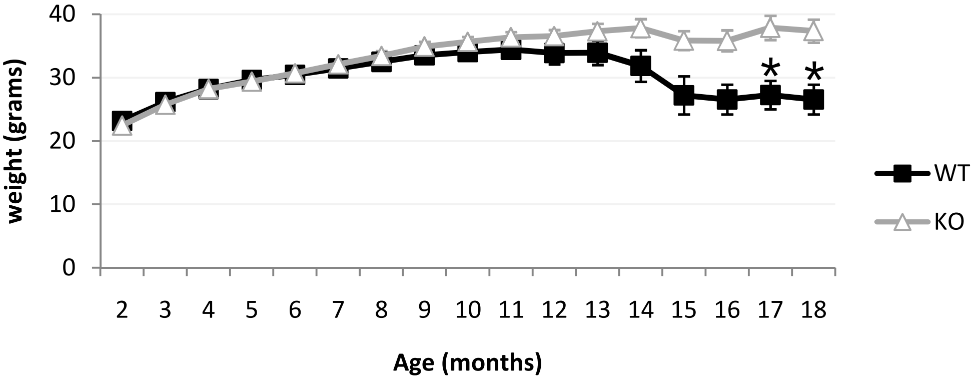

Figure R7. Line chart representing weight of wild type (black squares) and *Gdap1*$^{-/-}$ (white triangles) mice. Average ± SEM are shown. Note that no differences were found since 2 to 16 months old mice (t Test value * < 0.05).

Rota-rod analysis.

Skeletal muscle weakness is the underlying cause of the majority of clinical problems in people suffering CMT disease. Nowadays we know that strength training may improve functional performance. In a comparative study, patients with CMT appeared to benefit significantly from a strengthening program, whereas patients with myotonic muscular dystrophy in the same study showed neither beneficial nor detrimental effects (El-Abassi et al. 2014).

The rota-rod test was specifically designed for making automated measurements of neurological deficits in rodents, and is one of the most commonly used tests to measure motor function in mice (Brooks & Dunnett 2009). To avoid learning results in *Gdap1*$^{-/-}$ mice, we decided to perform rota-rod test just once in a life time by animal. Doing this we obtained point-time results along age but we avoid the learning parameter after several trials.

With the rota-rod test, we detected significantly reduced latency to fall in 3 months-old *Gdap1*$^{-/-}$ mice. The persistence of this motor behaviour was confirmed in older *Gdap1* lacking mice, from 4 to 7 months of age, but became more variable and thus non-significant after 9 months of age (Figure R8).

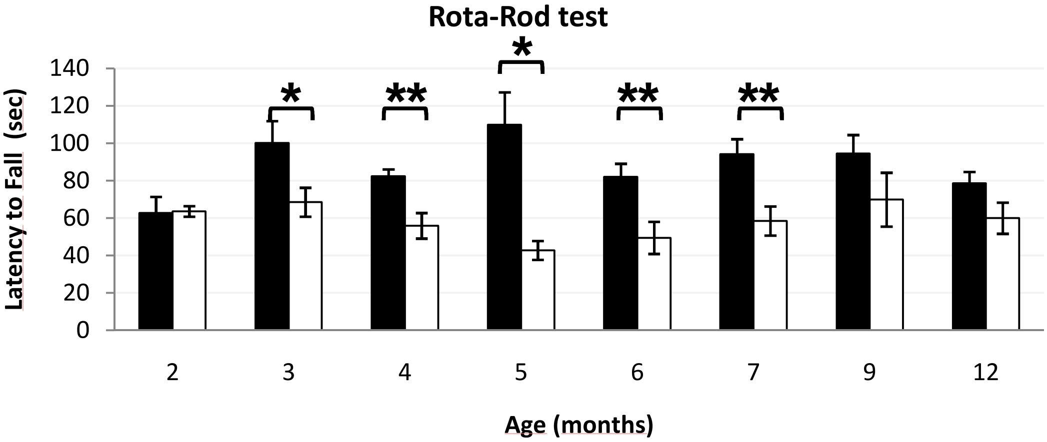

Figure R8. Column chart representing rota-rod scores for wild type (black) and *Gdap1*$^{-/-}$ (white) mice. Scores are represented as average ± SEM of time to fall off the accelerating rota-rod. (n>35, t Test value*≤ 0.05; **≤0.01).

Due to the lack of total penetrance that we had observed in our colony, we realized that siblings from the same litter could present different phenotypes, so we chose a cohort of more affected *Gdap1*$^{-/-}$ mice as an example of a severe affection of CMT and studied their motor behaviour. In this case we followed the evolution at rota-rod performance from the same mice over time (Figure R9). When compared to control mice *Gdap1*$^{-/-}$ animals always scored lower times of latency to fall, starting to be statistically significant at 5 months old and continuing this motor deficit up to 12 months.

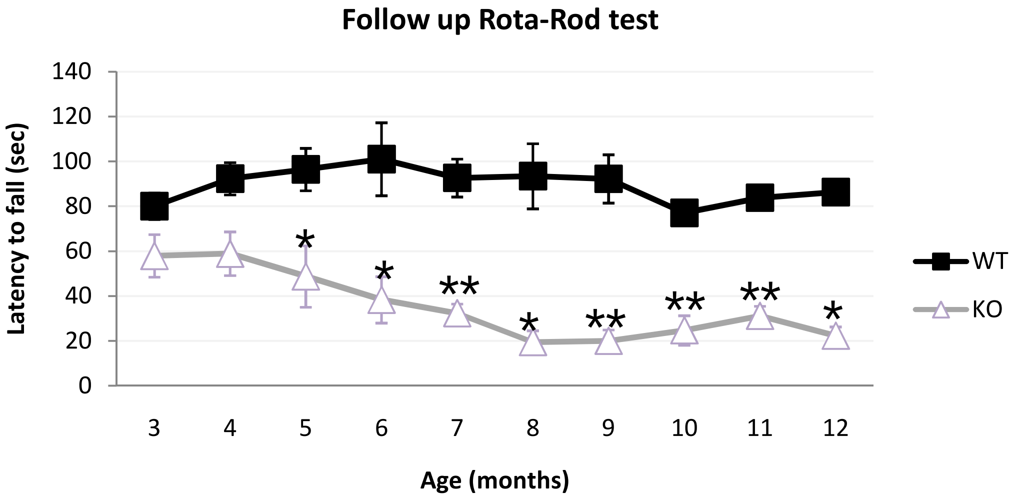

Figure R9. Line chart representing follow up rota-rod scores for wild type (black) and *Gdap1*$^{-/-}$ (white) mice. Scores are represented as average ± SEM of time to fall off the accelerating rota-rod. Animals used in this experiment performed rota-rod test monthly (n=3 for wild type and n=6 for *Gdap1*$^{-/-}$ mice, t Test value*≤ 0.05; **≤0.01).

Balance beam and pole tests.

Balance beam test assesses mice's ability to maintain balance while traversing a narrow beam to reach a safe platform. It was originally designed to assess motor deficits in aged rats and has been proved to be equally useful in assessing motor coordination and balance in young, injured and genetically altered mice (Brooks & Dunnett 2009). Along the same lines pole test can be used to analyse proprioception defects.

As our previous data showed that at 5 months old *Gdap1*$^{-/-}$mice presented rota-rod deficits, we decided to perform these both tests at this time point (figure R10). We could not detect any difference between knockout and control mice.

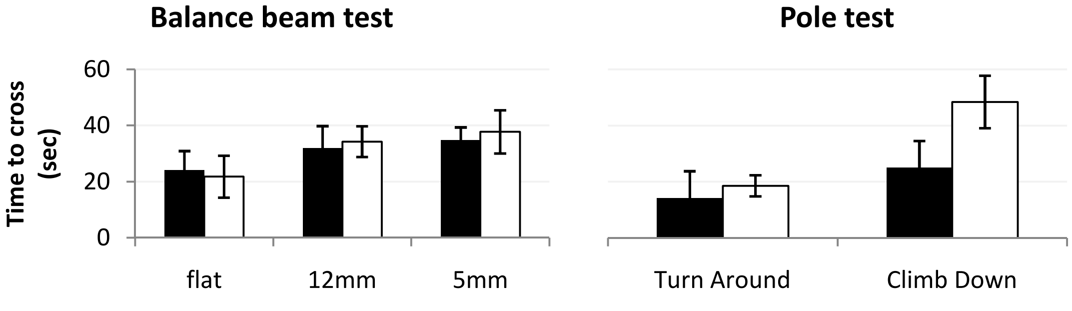

Figure R10. Column chart representing balance beam and pole test scores for wild type (black) and *Gdap1*$^{-/-}$ (white) 5 months old mice. Scores are represented as average ± SEM of time to cross, turn around or climb down. Animals used in this experiment only performed the test once in a life time, at 5 months old (n≥5).

Gait and footprint analysis.

A more detailed analysis of motor coordination and synchrony is provided by examining gait during normal walking (Brooks & Dunnett 2009). In order to better characterize motor phenotype of *Gdap1*$^{-/-}$ mice we analysed their gait behaviour at the age of 5 and 12 months (Figure R11).

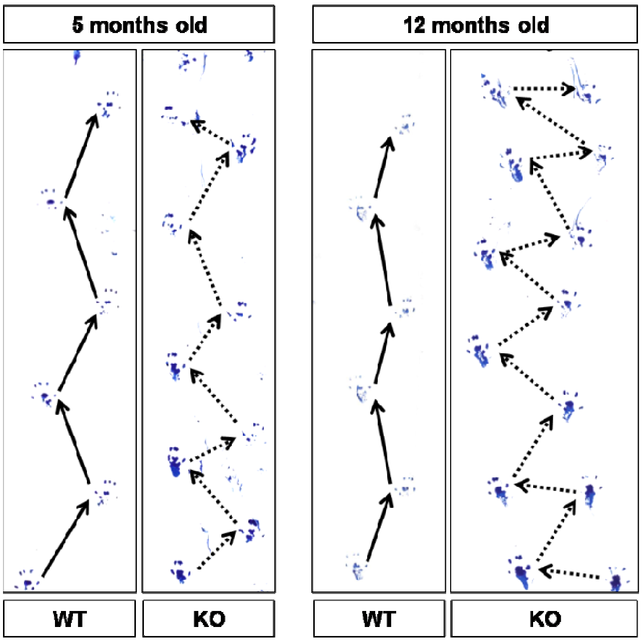

Figure R11. Representative hind limb walking track from a control (WT) and *Gdap1*$^{-/-}$(KO) mice at different age (5 and 12 months old). Arrows illustrate the gait to better distinguish shorter steps of *Gdap1*$^{-/-}$animals. Note also ink smears pattern due to dragged walking from CMT mice.

A detailed morphometric analysis of the gait (Table R1) revealed that at both time-points, *Gdap1*$^{-/-}$ mice had shorter stride length; and at 12 months we also detected narrower stride angle. Those facts agree with muscle weakness and steppage gait of CMT patients (Brennan et al. 2015).

We also detected an increase in stride width at 12 months; even though, as *Gdap1*$^{-/-}$ mice gain some weight with age we cannot correlate this parameter with sensory impairment as it has been done in other studies (Wiethölter et al. 1990), as long as there is a positive correlation between stride width and weight.

Gait-print	**5 months**		**12 months**	
	Mean (SEM)	p value	Mean (SEM)	p value
Stride Width				
WT	2,68 (0,09)	0,682	2,77 (0,20)	0,016
Gdap1$^{-/-}$	2,73 (0,09)		3,43 (0,07)	
Stride Length				
WT	7,49 (0,13)	0,043	7,25 (0,05)	0,013
Gdap1$^{-/-}$	6,70 (0,30)		6,41 (0,26)	
Stride Angle				
WT	130 (2)	0,196	132 (5)	0,014
Gdap1$^{-/-}$	127 (1)		112 (4)	

Table R1. Summary table of gait-print analysis parameters. Mean ± SEM from 5 control and 5 of *Gdap1*$^{-/-}$ mice are shown. Measurements are in centimetres apart from Stride Angle that is expressed in degrees. Student t test p values are also displayed.

As we observed everted paws in some mutant animals, we also analysed their footprints (Table R2). We detected a significant decrease of toe spreading values at 12 months in *Gdap1*$^{-/-}$ mice. As toe spreading correlates with the function of small foot muscles innervated by the sciatic nerve (Wiethölter et al. 1990), issues regarding sciatic nerve were revealed.

We also detected an increase in plantar length in *Gdap1*$^{-/-}$ mice at 5 months old which was more evident in 12 months old mice. Plantar length increases due to paresis of the flexors of the ankle (Wiethölter et al. 1990), when animals walk on their calcaneal bones which normally do not touch the ground.

Footprint	**5 months**		**12 months**	
	Mean (SEM)	p value	Mean (SEM)	p value
Plantar Length				
WT	1,27 (0,01)	0,029	1,20 (0,02)	0,000
Gdap1$^{-/-}$	1,32 (0,01)		1,38 (0,02)	
Toe Spreading				
WT	0,90 (0,04)	0,254	0,94 (0,01)	0,014
Gdap1$^{-/-}$	0,94 (0,04)		0,89 (0,01)	
Intermediate Toes				
WT	0,53 (0,03)	0,269	0,52 (0,02)	0,977
Gdap1$^{-/-}$	0,50 (0,02)		0,52 (0,03)	

Table R2. Summary table of footprint analysis parameters. Mean ± SEM from 5 control and 5 of *Gdap1*$^{-/-}$ mice are shown. Measurements are in centimetres. Student t test p values are also displayed.

2.- Histological findings

2.1- Skeletal muscle histopathology

Muscle abnormalities.

Effects of pathological and functional changes in *GDAP1* mutations causing CMT neuropathies are related to the axonal length, so distal limb muscles are usually the first to be affected (Sevilla et al. 2008). The classical CMT phenotype includes distal lower amyotrophy giving an aspect of “jambes de coq” or an inverted champagne bottle (Tazir et al. 2014).

Trying to find these human hallmarks in mice presents several hindrances. First of all mice are quadruped animals instead of bipeds. Secondly, human nerves can measure up to 120cm, compared to the 4 cm of the mice (Bala et al. 2014). Nevertheless, we excised and weighed larger distal muscles (soleus&gastrocnemius and quadriceps) looking for a CMT phenotype in our mouse model. The ratio of muscle mass (mg) divided by body mass (g) was calculated in order to control for the effect of mouse weight.

Strikingly, skeletal muscle weight ratio of *Gdap1*$^{-/-}$ mice didn't show any evidence of muscle mass loss in soleus&gastrocnemius at any time point. Unlikely, at quadriceps there was an increased ratio in *Gdap1*$^{-/-}$ mice at 9 and 15 months old (Figure R12). Maybe in mouse inverted champagne bottle appearance is due to an increase in quadriceps mass rather than a loss of gastrocnemius mass.

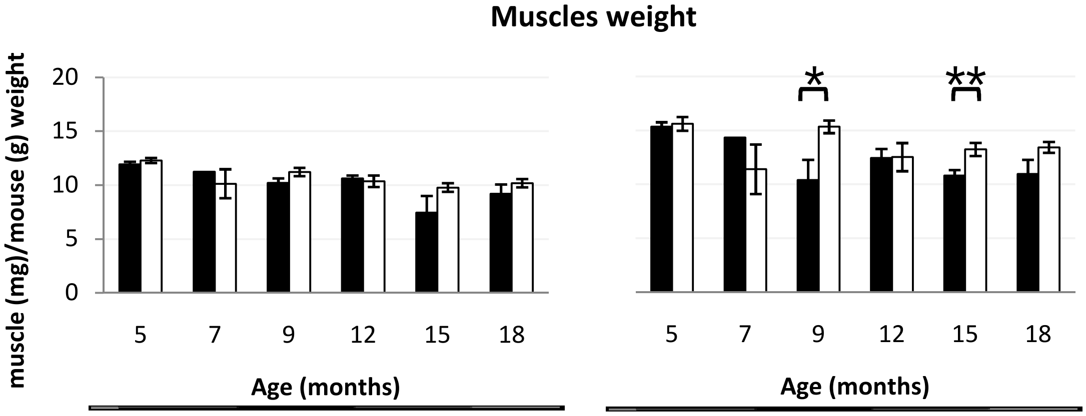

Soleus&Gastrocnemius Quadriceps

Figure R12. Column chart showing big distal muscles weight along age of wild type (black) and *Gdap1*$^{-/-}$ (white). Average ratio of muscle weight (mg) and animal weight (g) ± SEM is represented. Asterisks represent Student t Test value*< 0.05; **≤0.01.

To better understand motor deficits previously described, soleus&gastrocnemious muscles were studied microscopically in more detail. Hematoxilyn&eosin staining of paraffin-embedded muscle slices revealed inclusions of connective tissue at 5 months of age (

Figure R13). Presence of connective tissue in these muscles could explain why knockout mice didn´t show evidences of muscle wasting.

Same images showed damaged muscle fibres with pyknotic nuclear clumps and atrophic rounded muscle fibres in *Gdap1*$^{-/-}$ mice while this was less frequent in wild type animals (Figure R13).

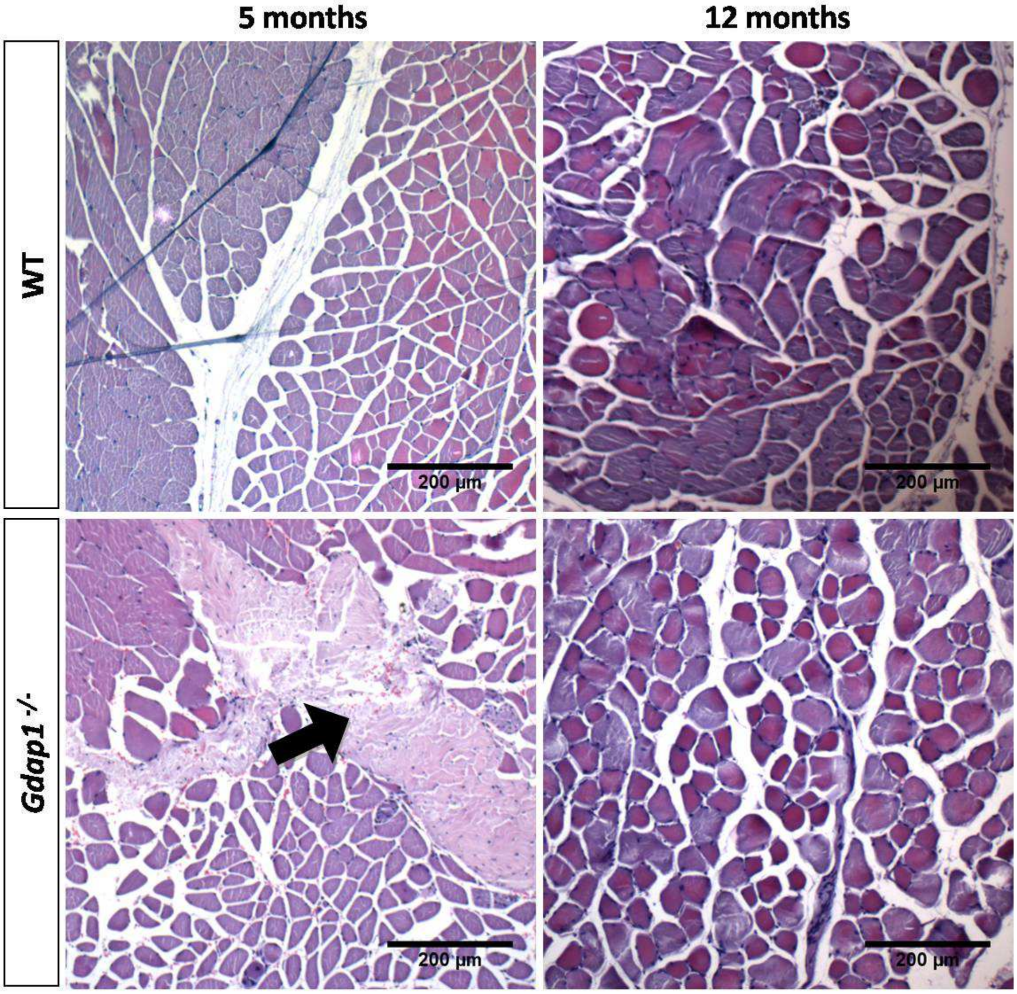

Figure R13. Representative images of gastrocnemius muscle from *Gdap1*$^{+/+}$ (WT) and *Gdap1*$^{-/-}$ mice at different age (5 and 12 months old). Hematoxilyn&Eosin staining of paraffined muscle sections. Scale bars represents 200µm. Arrow marks connective tissue inclusion. Note the shape and colour change in 12 months old *Gdap1*$^{-/-}$ muscle.

NMJ occupancy.

Distal skeletal muscle weakness is the underlying cause of the majority of clinical problems in CMT patients. The contractile activity of skeletal muscle is regulated by action potentials from motor neurons to muscle fibres. Transmission occurs at a highly specialized chemical synapse, the neuromuscular junction (NMJ) or motor endplate. Accordingly, impairment of NMJ function results in muscle weakness or paralysis (Tintignac et al. 2015). Due to the tight correlation between synaptic activity and NMJ morphology, a great deal of information can be gained about the functional status of motor neurons from analysis of NMJ morphology (Murray et al. 2014). Based on that we decided to study NMJ in *Gdap1*$^{-/-}$ and WT mice at adult age.

We selected gastrocnemius as distal skeletal muscle because its NMJ characteristics. As gastrocnemius is a ‘Delayed Synapsing’ (DeSyn) muscle, NMJ maintenance depends critically on nerve-derived factors (Pun et al. 2002). NMJ were imaged labelling axons and receptors in muscle fibres (Figure R15). More than 100 NMJ were analysed for each genotype and age and no differences in the total number of plates were found between knockout and wild type mice either at 5 or 12 months old (Figure R14).

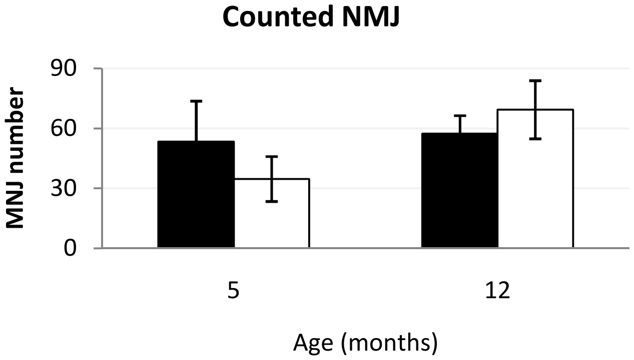

Figure R14. Bar chart showing number of NMJ counted in wild type (black) and *Gdap1*$^{-/-}$ (white) mice along time. Average of NMJ counted per animal ± SEM are represented (n=3).

Labelled receptors in muscle fibres were similar in shape and distribution in *Gdap1*$^{+/+}$ and *Gdap1*$^{-/-}$ mice (Figure R15). Reduction in the complexity of the NMJ morphology as a mark of muscular plate damage (Murray et al. 2014) was not observed.

In contrast, irregular labelled axon terminals were found in knockout muscles. These atypical axon ends didn't take over the postsynaptic folds (asterisk in Figure R15). In order to quantify these abnormalities we classified NMJ into occupied and non-occupied according to whether the muscular part of the plate was completely filled by the axon terminal or not (see Materials&Methods for more details).

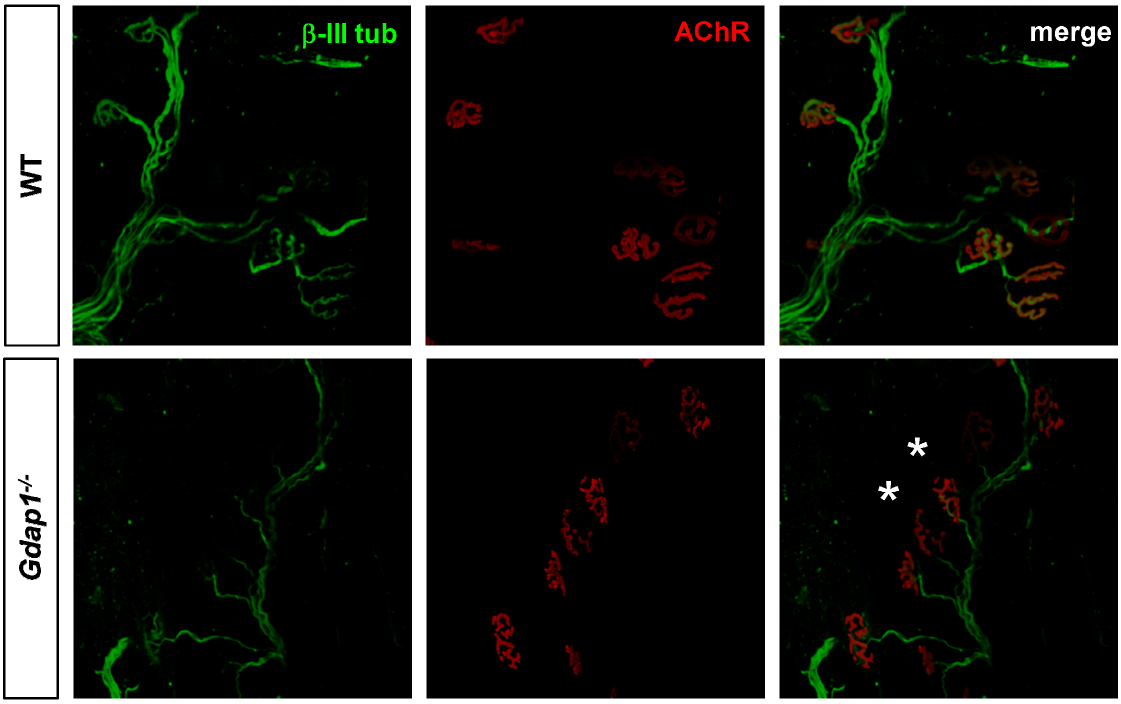

Figure R15. Representative confocal 3D rendering stack of images of NMJs from the gastrocnemius muscle of 12 months old mice. Axons were immunostained with anti-β-III tubulin (β-III tub, green) and the postsynaptic acetyl-choline receptor was stained with rhodamine-coupled α-bungarotoxin (AChR, red). Denervated or non-occupied NMJ are marked with asterisks. Note that in non-occupied NMJ, axon doesn't take over the postsynaptic folds.

Occupancy study revealed no differences at 5 months old where control mice showed completely occupied NMJ (99%±1%) as well as *Gdap1*$^{-/-}$ mice (92%±6%). In contrast, NMJs from 12 months old wild type mice were fully occupied (98%±0%) the percentage of occupancy in *Gdap1*$^{-/-}$ muscle was significantly reduced (70%±1%) (p<0.001) (Figure R16).

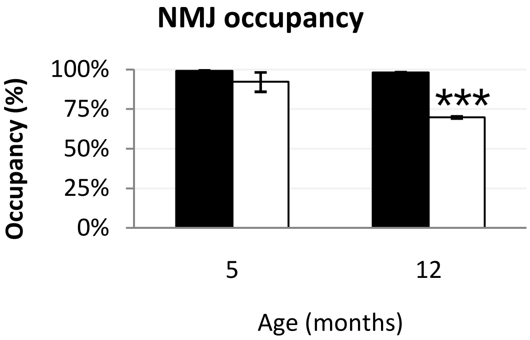

Figure R16. Bar chart representing percentage of occupied NMJ along mice age. Average percentage ± SEM for control mice are showed in black and for *Gdap1*$^{-/-}$ in white. (n=3, Student t Test p value ***< 0.001)

Typical fragmented appearance as seen during Wallerian degeneration upon nerve transection or crush (Coleman & Freeman 2010) was not detected. However, we observed abnormal tangle-like structures and focal swellings near to axon terminals of 12 months knockout animals; that were not present in control mice (Figure R17). This feature, a swollen axonal segment with a protruding axonal process, was commonly seen in retreating axons (Bishop et al. 2004).

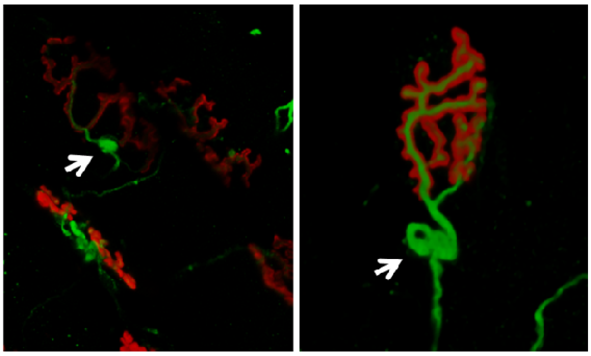

Figure R17. Confocal stack images of NMJs from the gastrocnemius muscle of 12 months *Gdap1*$^{-/-}$ mice. Axons were immunostained with anti-β-III tubulin (β-III tub, green) and the postsynaptic acetyl-choline receptor was stained with rhodamine-coupled α-bungarotoxin (AChR, red). Arrows mark abnormalities like a retraction bulb (left) and terminal tangle (right).

2.2- Sciatic nerve studies

Electrophysiology abnormalities.

The observed defects in motor behaviour in mice lacking GDAP1 prompted us to further investigate their electrophysiological properties along the sciatic nerve. Therefore, we measured the motor nerve conduction velocity (MNCV) and compound motor action potential (CMAP).

In line with the absence of detectable behavioural phenotype, we were not able to detect any electrophysiological differences between *Gdap1*$^{-/-}$ and WT mice at 2-months of age. At 5 months, a reduction of MNCV was found in GDAP1 lacking mice that showed a velocity of 37.5±0.8m/s in comparison with 40±0.7m/s of wild type (Figure R18). Slight reductions in MNCV can be associated with axonal neuropathies (Sevilla et al. 2003) while more considerable reductions are associated with demyelinating neuropathies (Tazir et al. 2014).

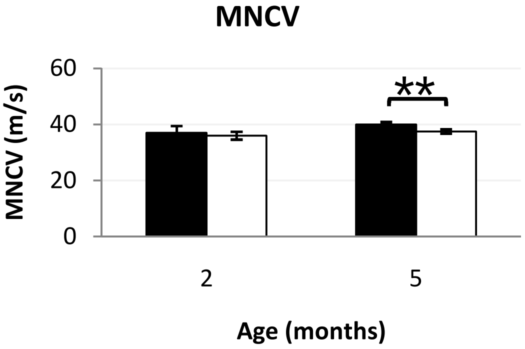

Figure R18. Motor Nerve Conduction Velocity measurement in wild type and *Gdap1*$^{-/-}$ mice at 2 and 5 months old. Average velocity (±SEM) from wild type mice are represented in black and *Gdap1*$^{-/-}$ in white (n≥4). Asterisks are indicative of the t test p-values (**p≤0.01).

In addition, we also studied the CMAP. The CMAP is a summated voltage response from the individual muscle fibre action potentials. Several parameters were measured from CMAP responses: latency, duration, amplitude and area (Mallik & Weir 2005).

Interestingly, 5-months *Gdap1*$^{-/-}$ mice revealed a significant reduction of CMAP amplitude and area obtained for distal (at the ankle) and proximal (at the hip) stimulation (Figure R19). Amplitude and area reflect the number and size of muscle fibres that ultimately fire. Lower values results from loss of motor axons or neurons; less often a NMJ disorder (Katirji et al. 2013).

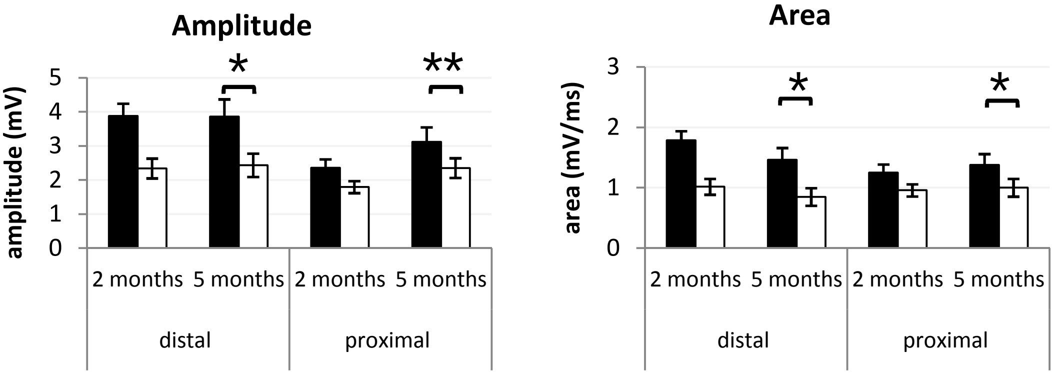

Figure R19. Compound Muscle Action Potential (CMAP) amplitude and are analysis in wild type and *Gdap1*$^{-/-}$ mice at 2 and 5 months old. Average amplitude and area (±SEM) from wild type mice are represented in black and *Gdap1*$^{-/-}$ in white (n≥4). Asterisks are indicative of the t test p-values (*p<0.05; **p≤0.01).

Duration was also altered in 5 months *Gdap1*$^{-/-}$ mice. Proximal stimulated duration was significantly increased in comparison with wild type animals (figure R20). CMAP duration is primarily a measure of synchrony. Duration increases in conditions which result in selective slowing of some motor fibres (Katirji et al. 2013).

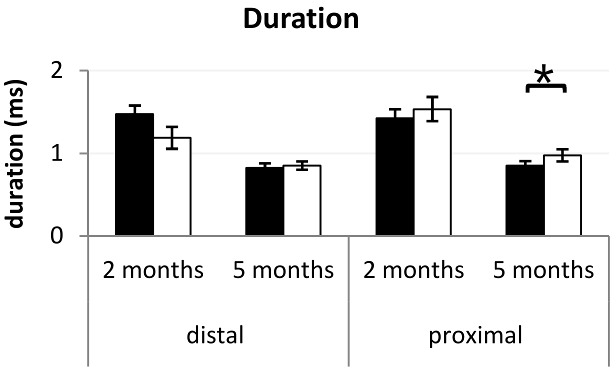

Figure R20. Compound Muscle Action Potential (CMAP) duration analysis in wild type and *Gdap1*$^{-/-}$ mice at 2 and 5 months old. Average duration (±SEM) from wild type mice are represented in black and *Gdap1*$^{-/-}$ in white (n≥4). Asterisks are indicative of the t test p-values (*p<0.05).

Strikingly, 5 months old knockout animals also revealed a significant reduction of CMAP latency obtained for distal (at the ankle) and proximal (at the hip) stimulation (Figure R21). Latency includes three separate times: nerve conduction time from the stimulus site to the NMJ, the time delay across the NMJ and the depolarization time across the muscle fibres (Katirji et al. 2013). Opposing to our data, an increase in latencies reflects the nerve conduction slowing of the fastest fibres (Tankisi et al. 2012).

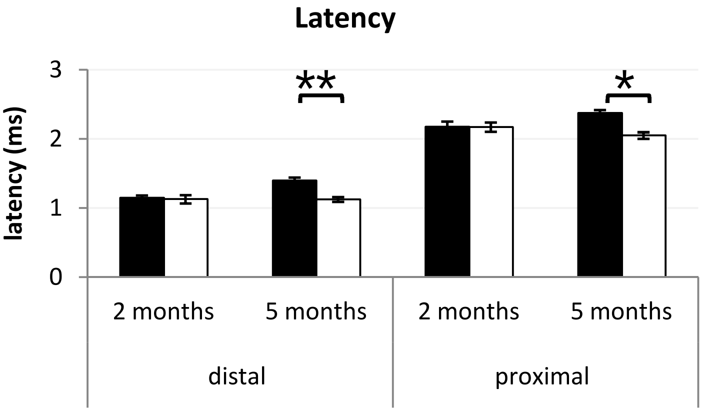

Figure R21. Compound Muscle Action Potential (CMAP) latency analysis in wild type and *Gdap1*$^{-/-}$ mice at 2 and 5 months old. Average latency (±SEM) from wild type mice are represented in black and *Gdap1*$^{-/-}$ in white (n≥4). Asterisks are indicative of the t test p-values (*p<0.05;**p<0.01).

Morphometric analysis.

Generally, myelinated nerve fibres suffer from different degrees of atrophy with age. Analysis of the myelinated nerve fibres of the sciatic nerve pointed to the significant atrophy and loss of large myelinated nerve fibres with age. An increase in the number of small nerve fibres with a thinner myelin sheath might point to the regeneration of nerve fibres during the aging process (Ugrenović et al. 2015). Specifically, in CMT caused by mutations of *GDAP1*, sural nerve biopsy reveals axonal atrophy, absence of onion bulbs, axonal loss and absence of demyelinated fibres (Sevilla et al. 2003). To investigate if these features found in CMT patients were present in our mouse model sciatic nerve from 5 month old mice were dissected.

Semi-thin sections didn't reveal any marked loss of myelinated fibres or the presence of onion bulbs or other anomaly. Ultrathin sections were used in order to better characterize axon population (Figure R22).

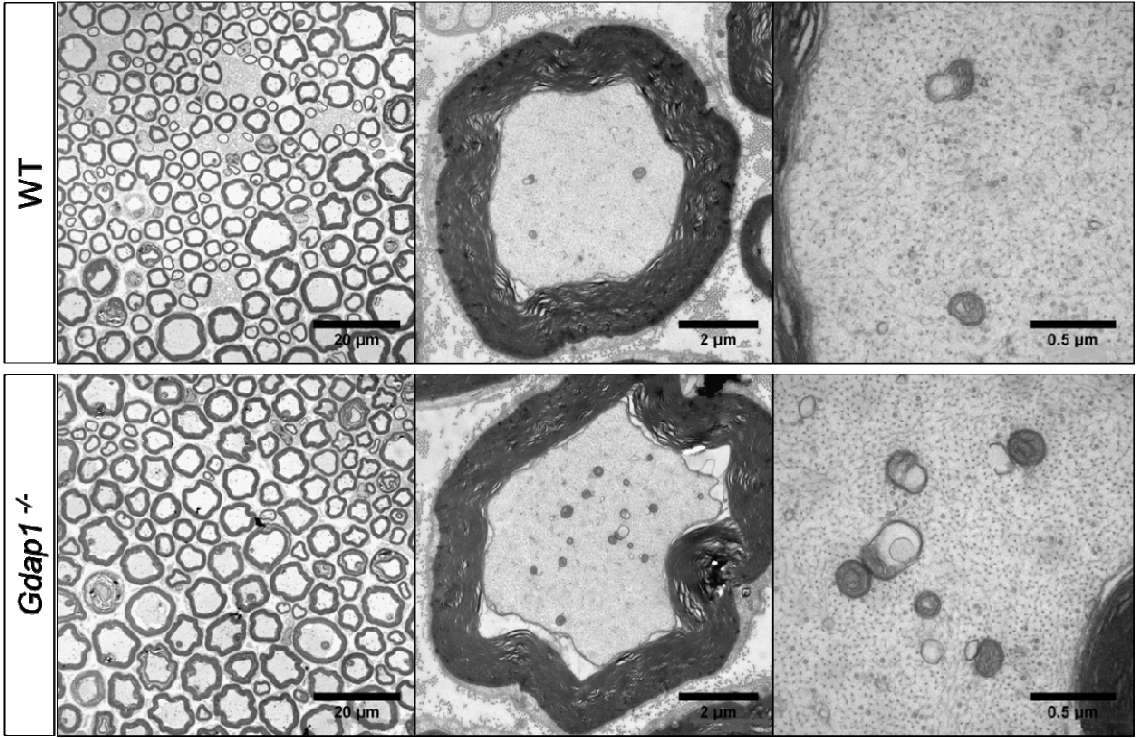

Figure R22. Representative ultrathin sections of Wild type and *Gdap1*$^{-/-}$ sciatic nerve from 5 month old mice. Scale bars represented 20, 2 and 0.5 µm respectively.

Ultrathin sections images allowed us to calculate myelinated fibre density in proximal and distal sciatic nerve. Density of myelinated fibres was lower in distal part of *Gdap1*$^{-/-}$ sciatic nerve at 5 months old in comparison with control mice (Figure R23). In *GDAP1*-CMT patients, axonal neuropathy is associated with loss of axons in sural nerve biopsies (Sevilla et al. 2008).

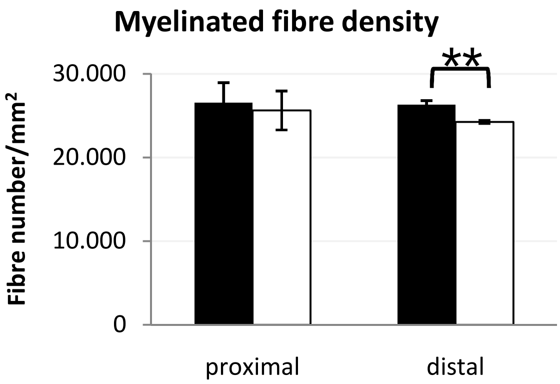

Figure R23. Myelinated fibre density quantification from 5 month old mice. Average density (±SEM) of wild type mice are represented in black and *Gdap1*$^{-/-}$ in white. Values for proximal and distal part of sciatic nerve are represented. Asterisks are indicative of student t test values test (**$p<0.01$). More than 1100 axons were counted for each condition (n=4).

Same ultrathin sections were used to measure g-ratio and axon diameter. Both parameters remain significant tools for the analysis of the myelinated nerve fibres in ''healthy'' peripheral nerves as well as in different types of neuropathies. Rushton in 1951 correlated axon and myelin sheet diameter by g-ratio. Value of 0.6 seems to be optimal for the conduction velocity of nerve impulses (Ugrenović et al. 2015).

Lacking GDAP1 mice had not affected g-ratio, neither in proximal nor distal part of sciatic nerve (table R3). Measures for both part of the nerve were similar and close to the optimal value.

g-ratio	Proximal	Distal
Wild type	0,68 (±0,01)	0,65 (±0,01)
Gdap1$^{-/-}$	0,68 (±0,01)	0,63 (±0,01)
P value	0,883	0,300

Table R3. g-ratio quantification from 5 month old mice sciatic nerve fibres. Average g-ratio (±SEM) of wild type and *Gdap1*$^{-/-}$ mice are shown. Data for proximal and distal part of sciatic nerve are represented. Student's t test p-values are exposed (n=4).

Studying myelinated fibres size revealed no differences in the average of axon diameter at 5 months old mice (Table R4). Average diameter was around 3µm for both genotypes either in proximal as in distal part of sciatic nerve.

Table R4. Myelinated fibre axon diameter quantification from 5 month old mice. Average diameter (±SEM) of wild type and *Gdap1*$^{-/-}$ mice are shown. Data for proximal and distal part of sciatic nerve are represented. Student's t test p-values are exposed (n=4)

Axon size	Proximal	Distal
Wild Type	3,18 (±0,14)	3,00 (±0,10)
Gdap1$^{-/-}$	3,19 (±0,14)	3,12 (±0,04)
P value	0,791	0,286

Nevertheless, we analysed myelinated fibre size distribution and detected higher density of large axons in distal nerve from *Gdap1*$^{-/-}$ mice (Figure R24). Deficient GDAP1 mice also showed lower density of axons of 2µm diameter. No fibres larger than 9µm were found, yet both genotypes displayed a population of very small myelinated fibres (1-3µm).

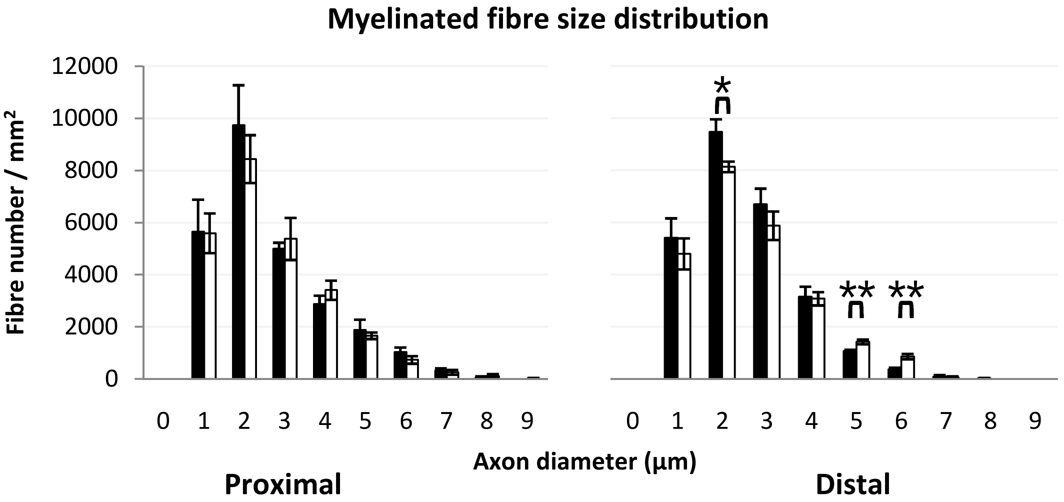

Figure R24. Axon diameter distribution of myelinated fibre from 5 month old mice. Average density (±SEM) for each diameter is shown. Wild type is represented in black bars, and *Gdap1*$^{-/-}$ mice density in white. Data for proximal and distal part of sciatic nerve are represented. Asterisks are indicative of Student's t test p-values (*p<0.01,**p<0.01, n=4).

Since GDAP1 is a mitochondrial protein (Pedrola et al. 2005; Niemann et al. 2005)we were also interested to perform the characterization of this organelle inside sciatic nerve fibres. Shape, morphology and localization was similar between knockout and control mice at 5 months old (Figure R22).

Surprisingly, when we analysed the number of mitochondria at proximal and distal sections of sciatic nerve, a higher number of mitochondria were counted in knockout animals at 5 months old (Figure R25).Even so, with this parameter we cannot affirm a higher number of mitochondria. It could be possible that longer mitochondria in sciatic nerve axons cause a higher number of mitochondrial sections in electron microscopy slices.

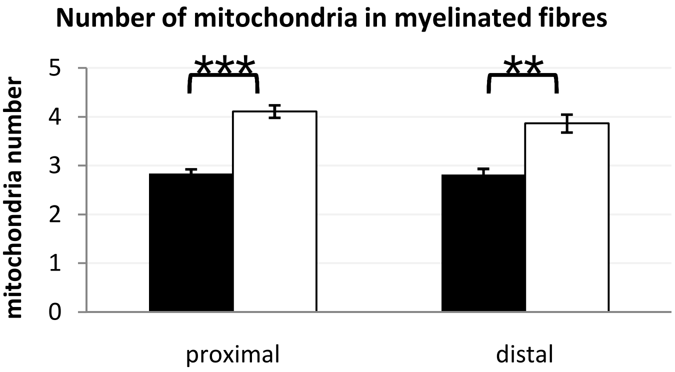

Figure R25. Number of mitochondria in myelinated fibres. Average number (±SEM) from wild type mice are represented in black and *Gdap1*$^{-/-}$ in white. Values for proximal and distal part of sciatic nerve are represented. Asterisks are indicative of Student's t test p-values (**p<0.01, ***p<0.001, n=4).

Mitochondrial DNA content.

To distinguish between the increment in number of mitochondria or the increase in their size, mtDNA/nuclear DNA ratio is used. Increased mitochondrial/nuclear DNA ratio is associated with increased mitochondrial biogenesis which could contribute to further oxidative stress leading to damaged mtDNA, mitochondrial dysfunction and oxidative damage (Malik & Czajka 2013).

Similar mitochondrial DNA copy number -normalized dividing by nuclear DNA copy number- was found in sciatic nerve of both WT and *Gdap1*$^{-/-}$ mice (

Figure R26). Since no difference in mitochondrial biogenesis was observed we reasoned that increase of the number of mitochondria within *Gdap1*$^{-/-}$ mice axons represent elongated mitochondria (Figure R25).

Figure R26. Quantification of mitochondrial DNA copy number by real-time PCR (16S/ANG1) in sciatic nerve samples from 5 month old mice. Average ±SE of a mix of 3 Sciatic nerve by genotype. Wild type data are shown in black bar and *Gdap1*$^{-/-}$mice results in white.

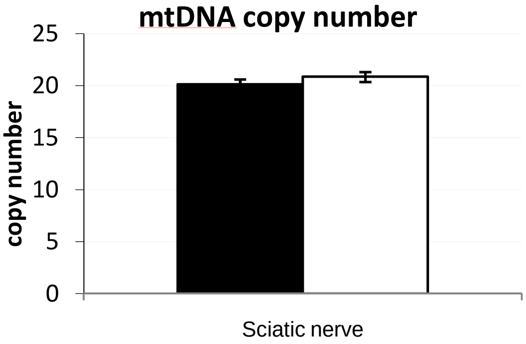

2.3- Histopathology of Spinal Cord

Motor neuron.

On account of the denervation observed at neuromuscular plates, we were interested in studying the soma of these motor neurons axons. The α motor neurons (MN) that send their axons to voluntary muscles have their soma in the Redex lamina IX in the ventral horn of the spinal cord. Specifically, MNs that control legs muscles contraction have their soma in the ventral horn of lumbar spinal cord (Stifani 2014).

In agreement with loss of properly occupied NMJ, we found alterations in MNs located in Redex lamina IX of ventral horn of lumbar spinal cord. A simple glance at Nissl stained paraffin embedded slices (Figure R27), indicated abnormalities in αMNs. While wild type αMNs had a "healthy" appearance, *Gdap1*$^{-/-}$ αMNs were pyknotic, without visible nucleolus. Moreover, some neurons from 12 months CMT mice had vacuoles.

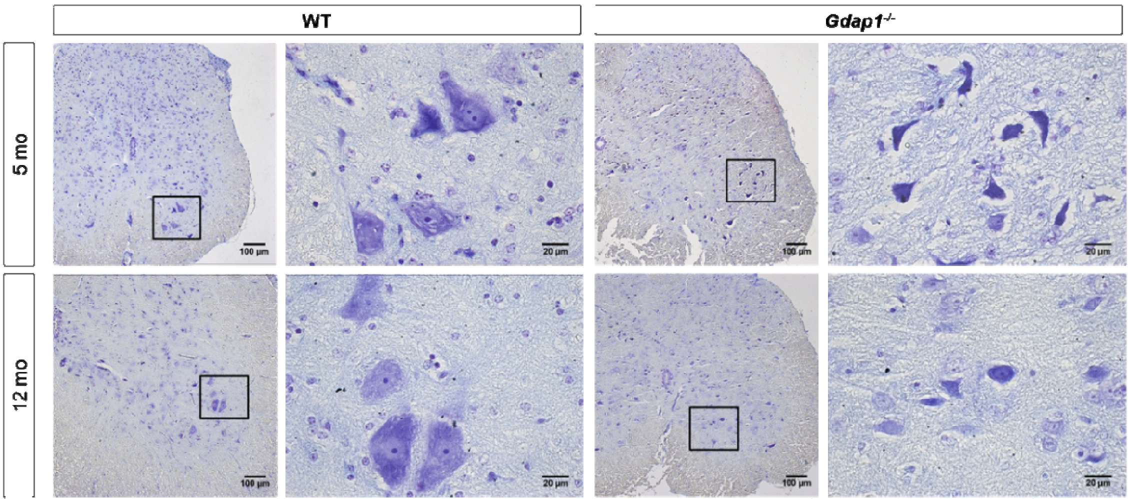

Figure R27. Representative images of lumbar spinal cord from *Gdap1*$^{+/+}$ (WT) and *Gdap1*$^{-/-}$ mice at different age (5 and 12 months old). Nissl staining of paraffined spinal cord sections. Scale bars represents 100µm and 20µm.

With the aim of quantify this abnormalities, healthy appearance MNs were counted. Less number of "healthy" MNs was found in *Gdap1*$^{-/-}$ mice at 5 and 12 months of age. However, while in control mice the number of healthy MNs per section underwent a progressive reduction over time (2-months vs 12-months WT animals, p-value<0.05), this process is enhanced in *Gdap1*$^{-/-}$ mice as indicated by the slopes of neuron loss between 2 and 5-months (*Gdap1*$^{-/-}$: 0.71 versus WT: 0.333). By contrast, slopes were equal between 5 and 12-months, which suggest that loss of neurons occurs early in the first months of life in the Gdap1-null mice (Figure R28).

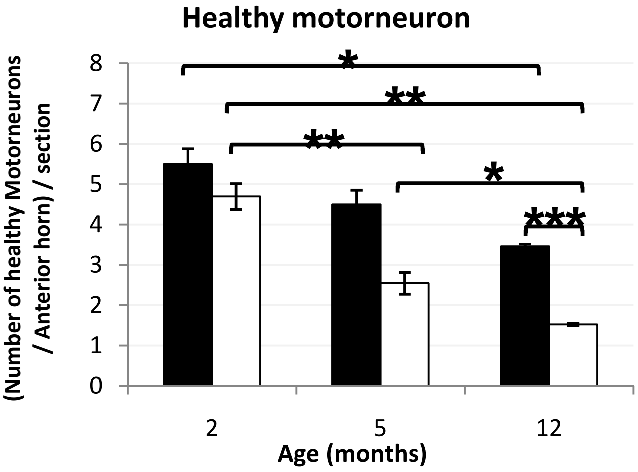

Figure R28. Number of "healthy" MNs in anterior horn per section in lumbar spinal cord. Average number (±SEM) from wild type mice are represented in black and *Gdap1*$^{-/-}$ in white. Asterisks are indicative of Student's t-test p-values (*p<0.05; **p<0.01, ***p<0.001).

Due to the histopathological features found in spinal cord, we were interested in investigate possible altered pathways in order to explain MNs pyknosis and vacuoles. Morphologically, apoptotic cells are characterized by the following classical changes: cell shrinkage, pyknosis, karyorrhexis, and the formation of apoptotic bodies. As potent regulators of the intrinsic apoptotic machinery, Bcl-2 family members, such as anti-apoptotic Bcl-2/Bcl-xL and pro-apoptotic Bax, can orchestrate the procedure of cell death (Wu et al. 2015).
By western blot we checked expression of principal pro-apoptotic (Bax) and anti-apoptotic (Bcl2) proteins in lumbar spinal cord lysates at three time points of both genotypes. (Figure R29). Surprisingly, *Gdap1*$^{-/-}$ mice presented increased of pro-apoptotic Bax at younger age (2 and 5, only significant at 2 months old). By contrast, in older age, 12 months old, CMT mice showed increased anti-apoptotic Bcl2.

Lack of GDAP1 has been related with increase of oxidative stress (Noack et al. 2012). In order to better understand oxidative stress we focused on determining catalase expression, the major hydrogen peroxide reducing enzyme.
Westerns blot revealed an increased expression of catalase in younger *Gdap1*$^{-/-}$ animals (Figure R29). Western blot at 12 months couldn't be performed.

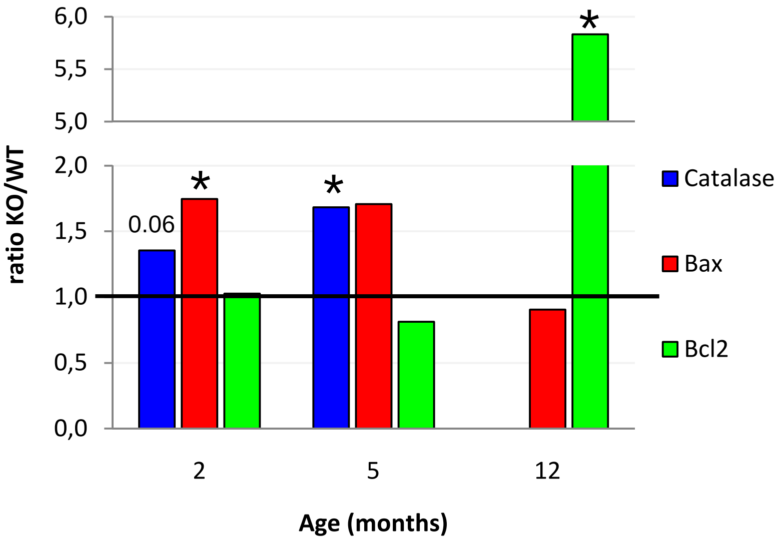

Figure R29. Oxidative-stress and apoptosis quantification in spinal cord along age. Quantification of western blot detection of Catalase, Bax and Bcl2. protein expression in wild type and *Gdap1*$^{-/-}$ (KO) spinal cord. Average ratio KO/WT is represented. Asterisks are indicative of Student's t-test p-values (*p<0.05, n≥3).

2.4- Histopathology of Dorsal Root Ganglia

Sensory neuron.

Mild to severe sensory loss is observed in *GDAP1*-CMT patients; particularity affecting to proprioception, vibration and touch (Baxter et al. 2002; Cuesta et al. 2002; Sevilla et al. 2003). We chose Dorsal Root Ganglia (DRG) to identify sensory defects in our mouse model.

Paraffin-embedded sections of DRGs from 5 and 12 months old mice were analysed and compared between wild type and *Gdap1*$^{-/-}$ mice. No abnormalities compared to control tissues were found in CMT mouse model even in old animals (figure R30). Appearance and distribution of sensory neurons didn't show any symptom of damage.

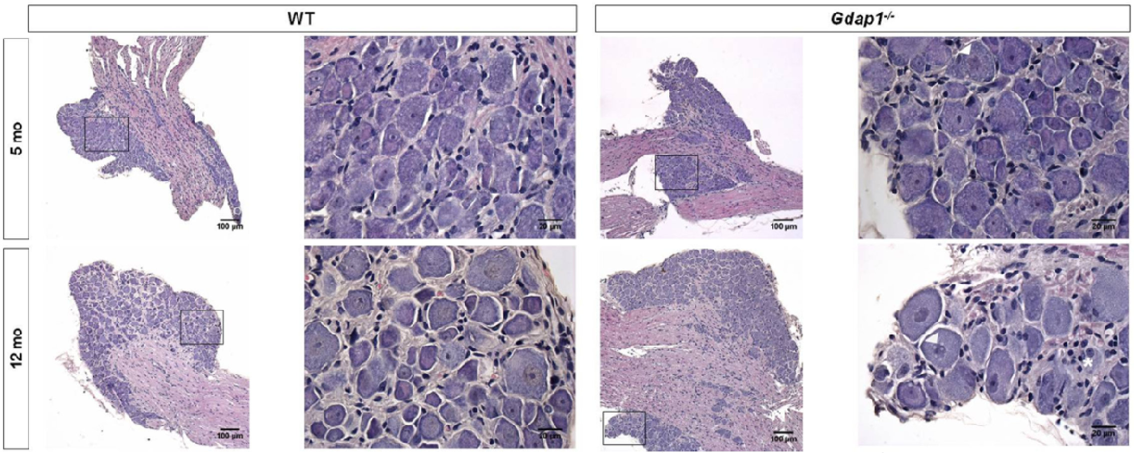

Figure R30. Representative images of DRGs from *Gdap1*$^{+/+}$ (WT) and *Gdap1*$^{-/-}$ mice at different age (5 and 12 months old). Haematoxylin-Eosin staining of paraffined DRG sections. Scale bars represents 100µm and 20µm.

3.-Pathogenic mechanisms

3.1- Adult Dorsal Root Ganglia (DRG) primary cultures

Mitochondria distribution inside neurites.

As a neurodegenerative disease, we were interested in having an adult primary cell culture model in order to study several CMT hallmarks associated with ageing. Dorsal Root Ganglia (DRG) primary culture has been widely used in neural diseases due to its easy dissection and maintenance. Although histology of DRG somas did not reveal any abnormality in our mouse model, sensory loss has been observed in *GDAP1*-CMT patients (Baxter et al. 2002; Cuesta et al. 2002; Sevilla et al. 2003). Dissociated DRG cultures allows us to study the grown of their processes in culture.

As GDAP1 is a mitochondrial protein (Pedrola et al. 2005; Niemann et al. 2005), our first attempt consisted of detecting defects in mitochondrial size or pattern, as was reported previously in *GDAP1* knock-down SH-SY5Y cell line (Pla-Martín et al. 2013). We tried different techniques to label mitochondria (immunodetection of cytochrome *c*, complex V of the respiratory chain and Tom20, and Mitotracker dye) but none of them gave us the specificity for axonal neurites we required. In adult mice (5 and 7 months old mice DRG cultures are shown in figure R31) neurites formed a net between neurons after 5 days "in vitro" (div) and it was very difficult to distinguish mitochondria from neurons from those mitochondria coming from non-neuronal cells of the culture. Also neurites from neighbouring neurons build up a network which makes it impossible to follow a single process.

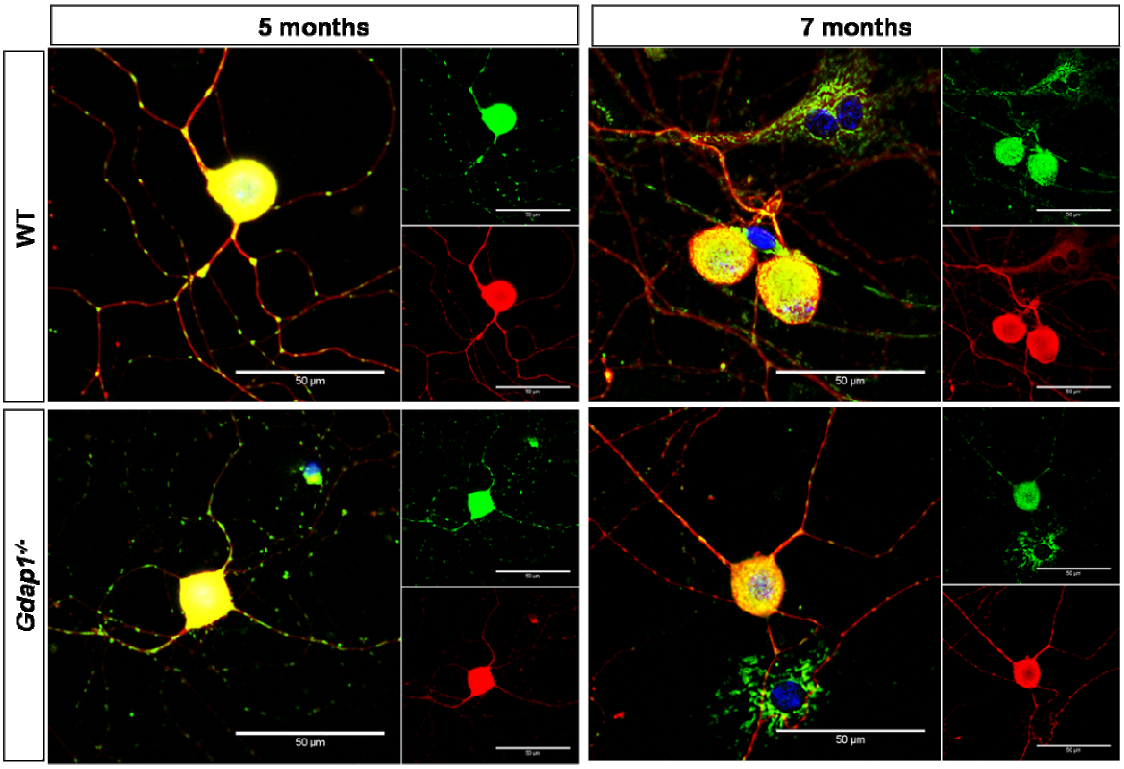

Figure R31. Neuron (βtubulinIII in red) and mitochondria (Cytochrome C in green) labelling in DRG culture from 5 and 7 month old mice. Representative images for mitochondria characterization in the DRG culture 5div. Red channel (βtubulinIII) and green channel (Cytochrome C) are showed in smaller images. Merge of both channels plus DAPI (in blue), for nuclei labelling, is showed in larger images. 50µm are represented in all scale bars.

Neuron morphology.

While we were trying to characterize mitochondria in DRG neurons in culture we noticed that *Gdap1*$^{-/-}$ neurons seemed to have fewer neurites than the control ones. In order to test this hypothesis we performed this quantification counting the number of processes that were outgrowing from DRG somas from 5 and 7 months old mice cultures. However, no difference was found between wild type and *Gdap1*$^{-/-}$ cultures, either at 5 or 7 months old mice (Figure R32).

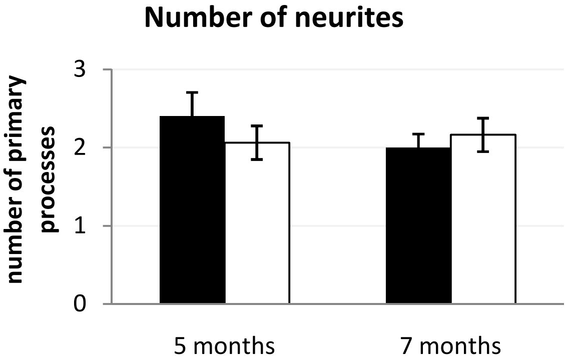

Figure R32. Number of primary neurites quantification in DRG culture from 5 and 7 month old mice. Average number (±SEM) of wild type mice cultures (5div) are represented in black and *Gdap1*$^{-/-}$ in white.

Soma area.

When we started to study DRG's cells in culture we also noticed that *Gdap1*$^{-/-}$ neurons seemed to be smaller than the control ones. As toxic effects can produce neurite retraction and soma atrophy (Zhu et al. 2007) we performed area quantification of soma in DRGs cultures from 5 and 7 months old mice. We could conclude that lack of *Gdap1* produce neurons with smaller soma (Figure R33).

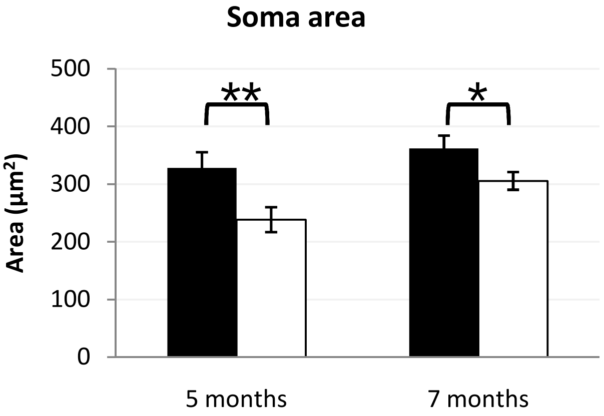

Figure R33. Soma area quantification in DRG culture from 5 and 7 month old mice. Average area (±SEM) of wild type mice cultures are represented in black and *Gdap1*$^{-/-}$ in white. Asterisks are representing the Student's t test p-values (*<0.05; **<0.01; ***<0.001).

Neurite length.

As in 5div cultures we observed smaller soma in *Gdap1*$^{-/-}$ cultures, we were interested in measure neurite length in order to check whether this was reduced due to the lack of *Gdap1*. To analyse neurite length we worked with 1div cultures, so we could follow a single process. Measurements were performed in two ways, calculating the average length of the three longest neurites per neuron and also counting only the longest one.

Shorter neurites were found in *Gdap1*$^{-/-}$ neurons in comparison with wild type ones using both methods (Figure R34). Growing defects or toxics effects can produce neurite retraction (Zhu et al. 2007).

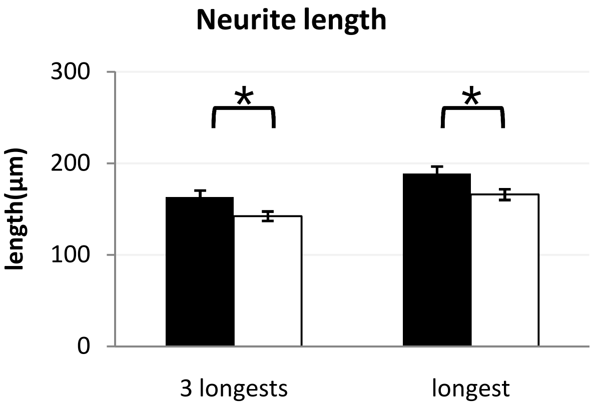

Figure R34. Neurite length quantification in DRG culture from 5 month old mice. Average length (±SEM) of wild type mice cultures are represented in black and *Gdap1*$^{-/-}$ in white. Three longest neurites and only the longest one were measured. Asterisks are representing the Student's t test p values (*<0.05).

Microtubule stability.

Remodelling of the microtubule cytoskeleton is essential to successfully complete all the different stages of neuronal development. Microtubules can provide tracks for intracellular transport, set up local cues to position organelles, act as signalling devices or generate cellular forces (Kapitein & Hoogenraad 2015).

Acetylation of α-tubulin or enzymatic removal of its C-terminal tyrosine residue (detyrosination) gradually occurs in the microtubule polymer and is therefore found in long-lived, stable microtubules, i.e., microtubules with a low turnover that undergo few catastrophic events (Witte et al. 2008). Moreover, mitochondria are mainly transported along microtubules consisting of polymerized tubulin. Therefore, we first decided to study acetylation of α-tubulin, as this process is considered to be a recognition signal for the anchoring of molecular motors and decreased levels of acetylated α-tubulin have been associated with neurodegenerative diseases (d'Ydewalle et al. 2011).

Using DRG primary cultures at 1div from 5 months old mice we observed a decrease in the fluorescence of acetylated α-tubulin in neurons lacking *Gdap1* (Figure R35), which was confirmed by fluorescence quantification of the 3 longest and the longest neurite (Figure R36).

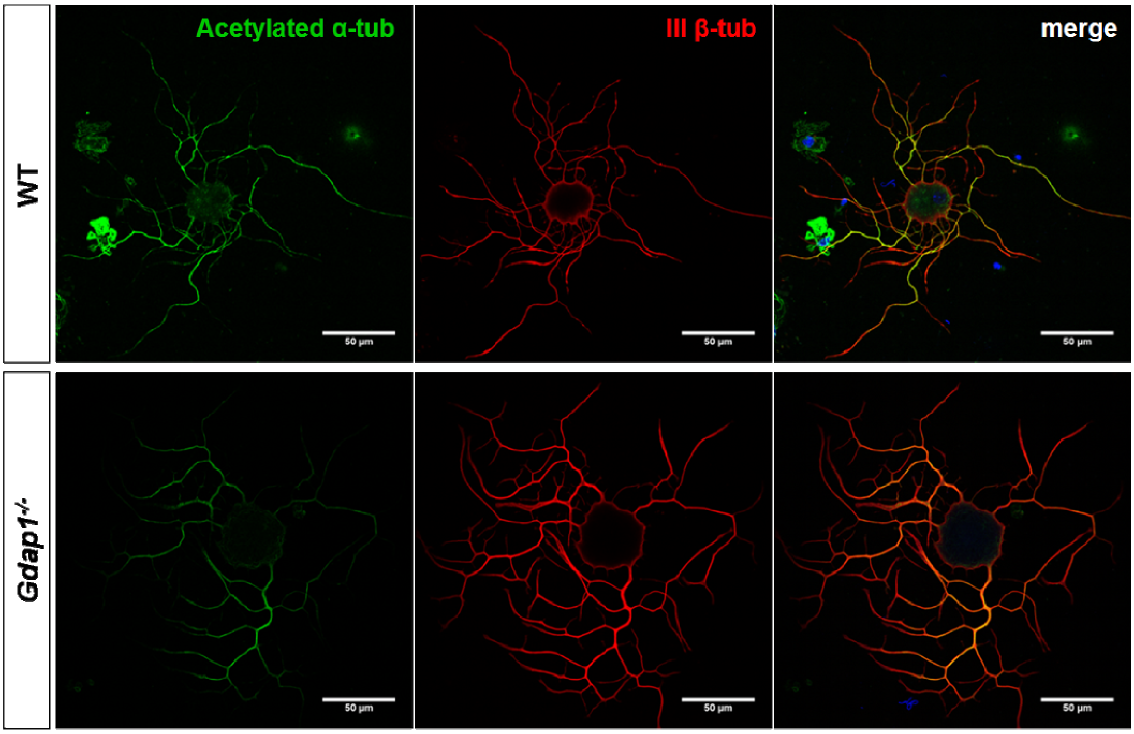

Figure R35. Representative images of cytoskeleton stability of DRG cultures from 5 months old animals. Acetylated α-tubulin (in green) and III β-tubulin (as neuron marker in red) labelling in DRG culture 1 DIV. Green and red channels are shown independently. In addition, merge of both channels plus DAPI (in blue), for nuclei labelling, is also showed. Scale bars represents 50µm.

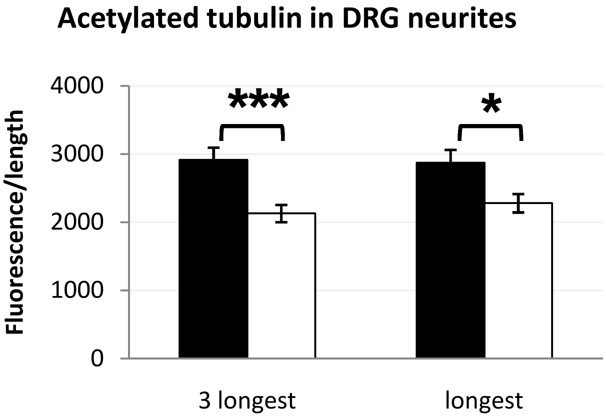

Figure R36. Acetylated α-tubulin quantification in DRG culture from 5 month old mice. Average of fluorescence/ length (±SEM) of wild type mice cultures are represented in black and *Gdap1*$^{-/-}$ in white. Three longest neurites and only the longest one were measured. Asterisks are representing the Student's t test p values (*<0.05; **<0.01; ***<0.001).

In addition, we also studied tyrosinated α-tubulin (Figure R37). No significant differences between wild type and *Gdap1*$^{-/-}$ neurons were observed in tyrosinated α-tubulin (Figure R38) but there was a trend towards an increase (p values 0.09 and 0.13 for 3 longest and the longest neuron) in *Gdap1*$^{-/-}$ cultures. Presence of tyrosinated α-tubulin in microtubules that has not yet undergone detyrosination denotes a recent assembly, that is, tyrosinated α-tubulin is found in dynamic microtubules with a high turnover (Witte et al. 2008).

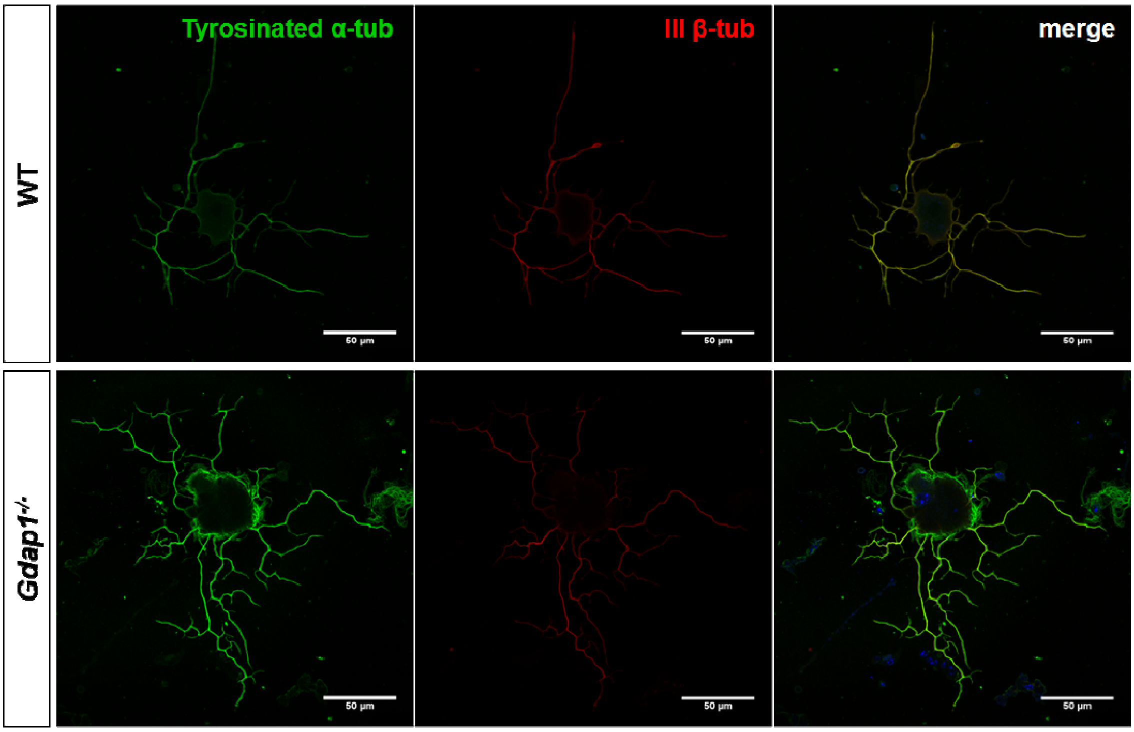

Figure R37. Representative images of cytoskeleton stability of DRG cultures from 5 months old animals. Tyrosinated α-tubulin (in green) and III β-tubulin (as neuron marker, in red) labelling in DRG culture 1 DIV. Green and red channels are shown independently. In addition, merge of both channels plus DAPI (in blue), for nuclei labelling, is also showed. Scale bars represents 50µm.

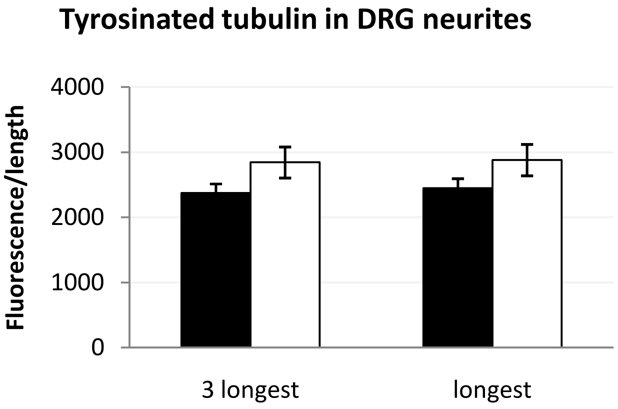

Figure R38. Tyrosinated α-tubulin quantification in DRG culture from 5 month old mice. Average of fluorescence/ length (±SEM) of wild type mice cultures are represented in black and *Gdap1*$^{-/-}$ in white. Three longest neurites and only the longest one were measured. Asterisks are representing the Student's t test p values (*<0.05; **<0.01; ***<0.001).

3.2- Postnatal DRG and SCG primary cultures

Working with postnatal cultures allows us to use new techniques, such as microinjection (Gilley & Coleman 2010), in order to better understand GDAP1 function. Microinjection of mitochondrial markers in several neurons allowed us to label all mitochondria along neurites only in selected neurons from total cultured cells (figure R39). This technique avoids labelling non-neuronal mitochondria and also permits to follow a single neurite to its end without having a complicated net. Studying labelled mitochondria during a period of time give useful parameters as percentage of moving organelle or velocity of movement (Andrews et al. 2010; Gilley et al. 2012) (figure R40).

All this work was done under Dr Coleman's supervision in The Babraham Institute (Cambridge, UK) were microinjection and imaging of SCG were already set up (Gilley & Coleman 2010). We compare two distinct types of neurons: DRG (peripheral, sensitive, affected in CMT) and SCG (sympathetic, non-affected in CMT but frequently used in the Coleman group because of their suitability for microinjection). Primary culture of both tissues were obtained from same animals and maintained in culture for these experiments. Microinjection of DRG was done at 4div and SCG at 6div. In both cases, imaging was done the day after microinjection. Data from wild type, *Gdap1*$^{-/-}$ and *Gdap1*$^{-/-}$ rescued cultures are presented below.

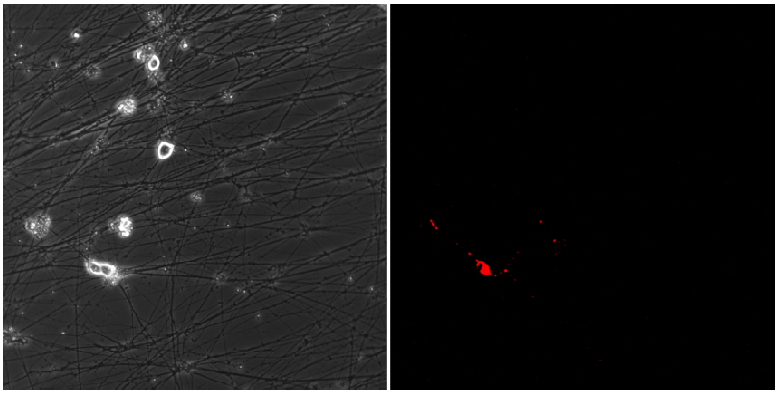

Figure R39. Microinjection of mitochondrial markers in SCG culture. Both images show same field. In left image we observe all neurons and its neurites in bright field. In right image we observe mito-DsRed expression only in microinjected neuron and its neurites.

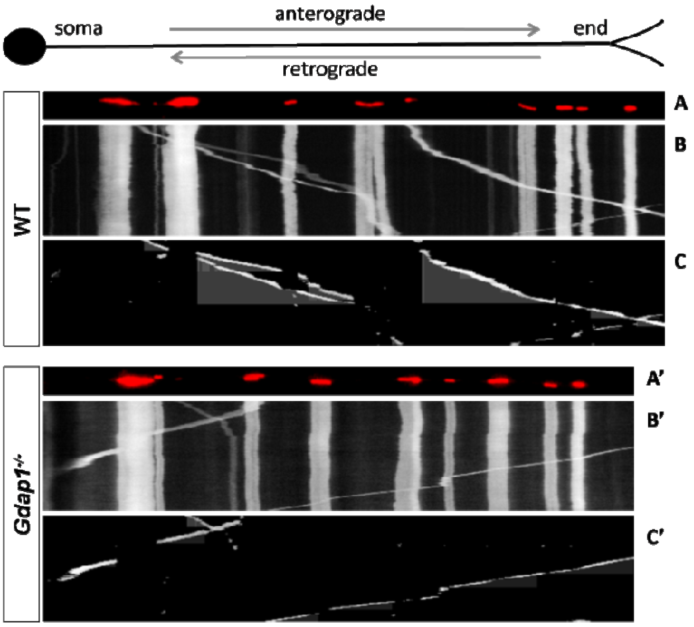

Figure R40. Representation of mitochondrial movement study in cultured sensory neurons. Representative images of WT and *Gdap1*$^{-/-}$ microinjected DRG neurons: (a) Representative straightened neurite (b) kymograph (time-distance graph) of mitochondria transport; static organelles appears as vertical bars while moving velocities correspond to horizontal bars slopes (c) Moving mitochondria from this kymograph identified using ImageJ plugin 'Difference tracker' (Andrews et al. 2010) were slopes are calculated. Soma reference is draw on top.

Mitochondrial movement.

First we analysed the percentage of moving mitochondria in both cultures. DRG neurites presented a trend but non-significant (p-value 0.08) towards and increased percentage of moving mitochondria (figure R41, left graph). There was no changes in mitochondrial moving inside neurites from SCG cultures (Figure R41, right graph).

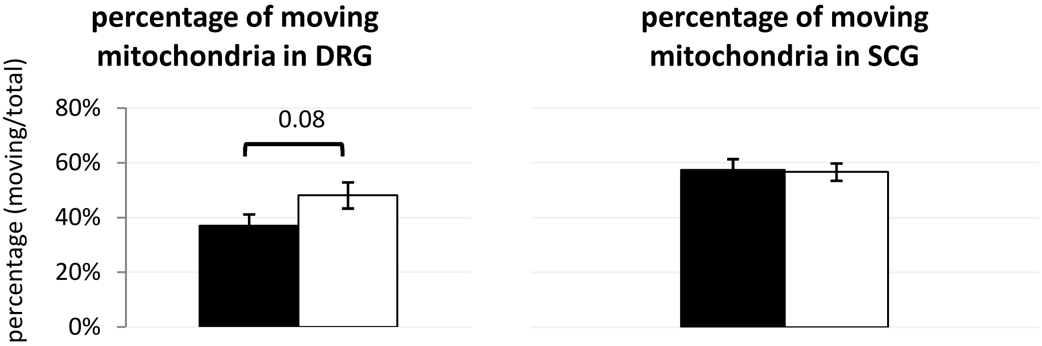

Figure R41. Percentage of total moving mitochondria in both DRG (left graph) and SCG cultures (right graph). The percentage was obtain by counting the number of moving mitochondria divide by the total number of mitochondria (static + moving). Average percentage (±SEM) of wild type cultures are represented in black and *Gdap1*$^{-/-}$ data in white.

Other parameter to take into account was the number of moving mitochondria in 100µm in one second. This parameter is different from the percentage; the mitochondria that were moving were counted but not the stationary ones (Andrews et al. 2010).

When we studied the number of mitochondria that moved in 100µm in one second, we observed a statistically non-significant trend (p-value 0.06) to increased retrogradely moving mitochondria in DRG cultures of *Gdap1*$^{-/-}$ animals (Figure R42, left graph). No differences were found in SCG neurons (Figure R42, right graph).

In addition, we could observe what happens when we rescued *Gdap1*$^{-/-}$ cultures by microinjection with a plasmid containing wild type *Gdap1* (Pedrola et al. 2008). When we rescued the deficient culture with GDAP1, we found a decrease in the retrograde moving mitochondria in both, DRG and SCG neurites that was not observed in the anterograde movement (Figure R42, grey bar).

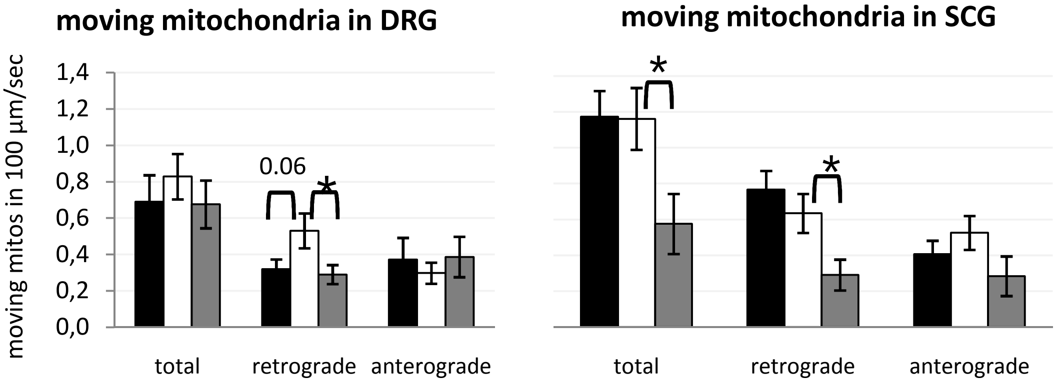

Figure R42. Number of moving mitochondria in 100µm per second in both DRG (left graph) and SCG cultures (right graph). Wild type data are represented in black, *Gdap1*$^{-/-}$ in white and rescued (microinjection of GDAP1-Wild type plasmid in *Gdap1*$^{-/-}$ neurons) in grey. Asterisks are representing the p-values of proper statistic test (*<0.05; **<0.01; ***<0.001).

With the same cultures, we were interested to investigate in detail velocities of moving mitochondria. We studied two parameters, average velocity and maximum velocity (Andrews et al. 2010).

Lack of GDAP1 did not affect to DRG neurons but produced slower mitochondria in null mice SCG cultures when we analysed average speed (Figure R43). In contrast, the rescue by reinsertion of GDAP1 in null mice neurons increased the velocity in DRG cultures but not in SCG. This increase was only in anterograde direction (Figure R43, gray bar).

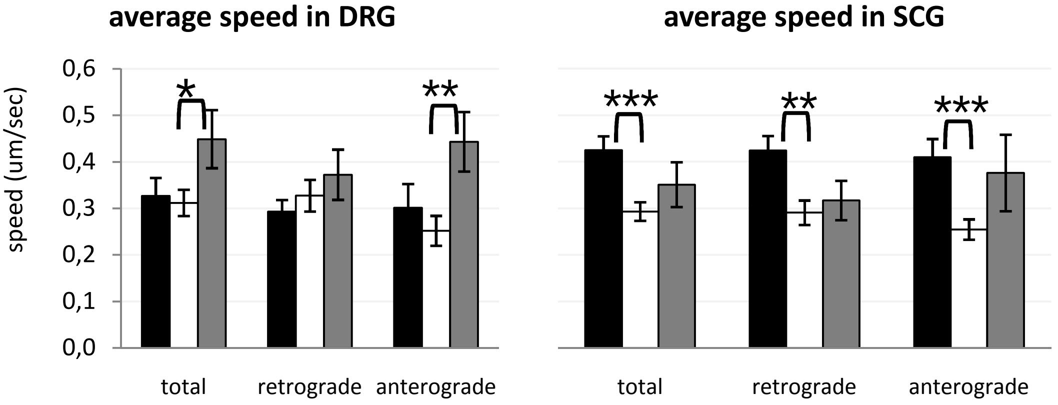

Figure R43.Average speed in both DRG (left graph) and SCG cultures (right graph). Wild type data are represented in black, *Gdap1*$^{-/-}$ in white and rescued (microinjection of GDAP1-wild type plasmid in *Gdap1*$^{-/-}$ neurons) in grey. Asterisks are representing the p-values of proper statistic test (*<0.05; **<0.01; ***<0.001).

In agreement, DRG neurons did not seem to be affected while SCG neurons from *Gdap1*$^{-/-}$cultures had a decreased maximum speed in comparison with wild type cultures (Figure R44). Also in concordance, rescued neurons by GDAP1 expression increased the mitochondrial maximum velocity in DRG cultures in anterograde direction while the rescue has no effect in SCG cells (Figure R44, gray bar).

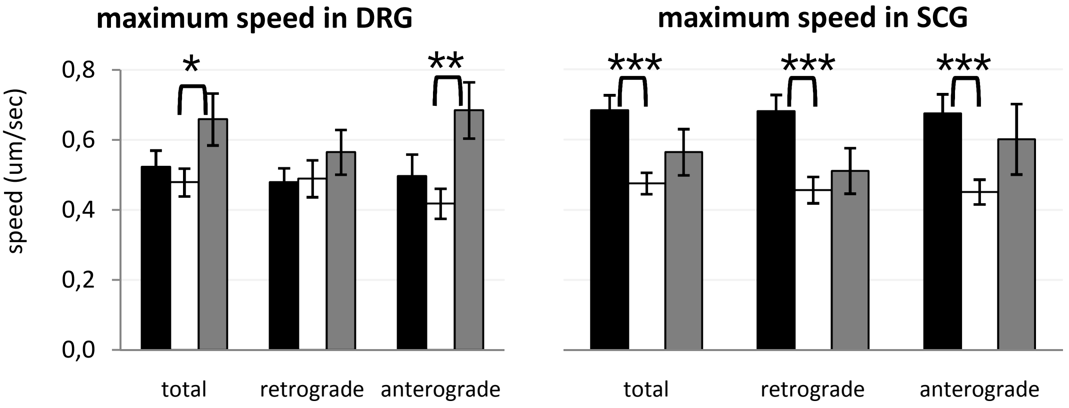

Figure R44. Maximum speed in both DRG (left graph) and SCG cultures (right graph). Wild type data are represented in black, *Gdap1*$^{-/-}$ in white and rescued (microinjection of GDAP1-wild type plasmid in *Gdap1*$^{-/-}$ neurons) in grey. Asterisks are representing the p-values of proper statistic test (*<0.05; **<0.01; ***<0.001).

Mitochondrial size.

As GDAP1 has been linked with mitochondria fusion and fission events (Niemann et al. 2005; Pedrola et al. 2008; Burté et al. 2014), size of moving mitochondria was also an interesting parameter to study. The images from mitochondrial movement experiments in postnatal DRG and SCG cultures were also used to characterize moving and static mitochondria size.

Retrogradely moving mitochondria from *Gdap1*$^{-/-}$ DRG cultures were longer than wild type ones (Figure R45, left graph). Interestingly, rescue of deficient cultures with GDAP1 caused shorter mitochondria moving in both, retrograde and anterograde direction (Figure R45, left graph, gray bar).

In contrast, SCG's moving mitochondria showed a statistically non-significant trend to be shorter in *Gdap1*$^{-/-}$ neurons (p value 0.07). Expressing GDAP1 in SCG cultures produced no effect in the size of these moving mitochondria (Figure R45, right graph).

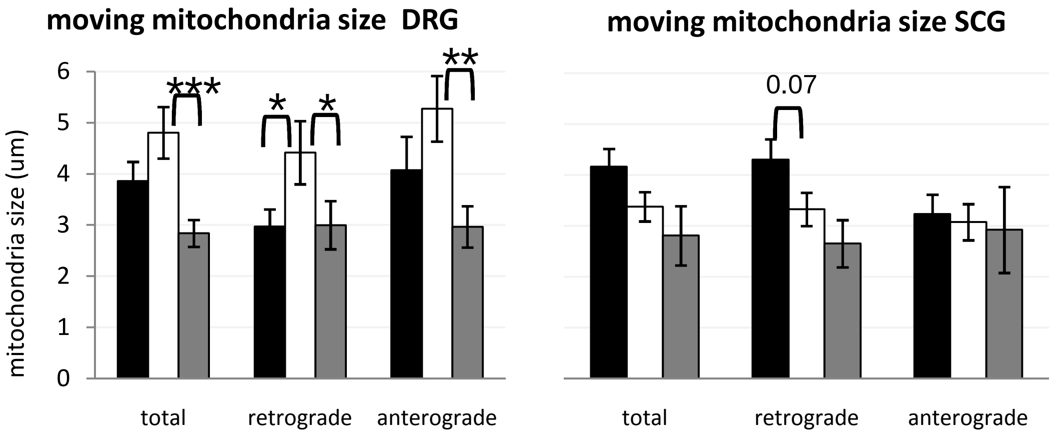

Figure R45. Moving mitochondria size in both DRG (left graph) and SCG cultures (right graph). Wild type data are represented in black, *Gdap1*$^{-/-}$ in white and rescued microinjection of GDAP1-wild type plasmid in *Gdap1*$^{-/-}$ neurons) in grey. Asterisks are representing the p-values of proper statistic test (*<0.05; **<0.01; ***<0.001).

In addition, we have also studied size of static mitochondria. DRG cultures did not reveal any difference between wild type and deficient mice cultures (Figure R46, left graph). On the other hand, in SCG cultured neurons, static mitochondria were longer in deficient mice cultures that in wild type (Figure R46, right graph).

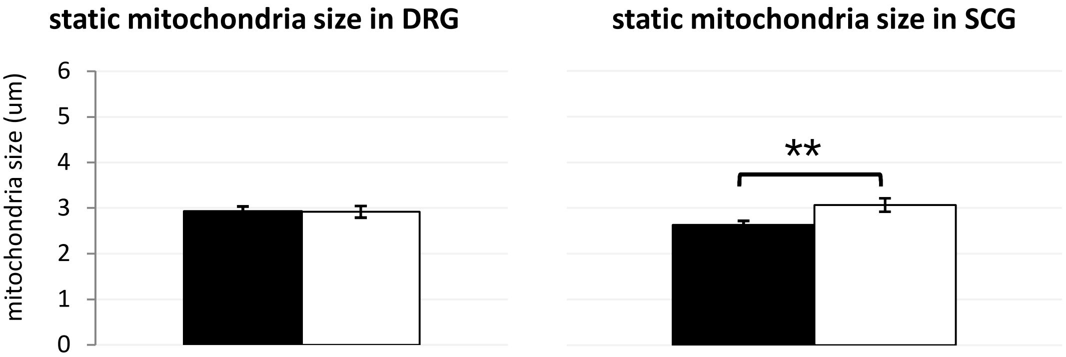

Figure R46. Static mitochondria size in both DRG (left graph) and SCG cultures (right graph). Wild type data are represented in black and *Gdap1*$^{-/-}$ in white. Asterisks are representing the p-values of proper statistic test (*<0.05; **<0.01; ***<0.001).

Effect of GDAP1 mutations in DRG primary cultures.

As we had already studied effects of the lack of *Gdap1* in postnatal DRG cultures (previous data), we were also interested in studying effects of *GDAP1*-CMT patient mutations in similar cultures. To investigate the effect of several *GDAP1* missense mutations (Figure R47) we used site-directed mutated cDNAs previously developed in our laboratory (Pedrola et al. 2008; Pla-Martín et al. 2013). Wild type (cDNA) *GDAP1* was also used in order to study the effect of overexpression (when it was microinjected in wild type neurons) and rescue (when it was microinjected in *Gdap1*$^{-/-}$ neuron cultures) in comparison with mutation effects. All plasmids were sent to Babraham Institute (Cambridge, UK) where maxiprep and sequencing were done prior to microinjection to confirm the point mutations.

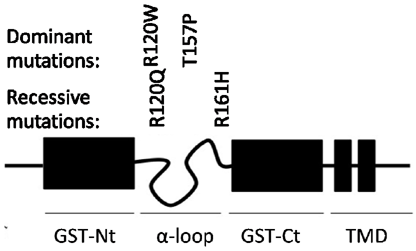

Figure R47. *GDAP1* missense mutations studied in this work. Used *GDAP1* dominant and recessive missense mutations and its localization along the protein (Adapted from Estela et al. 2011).

Next, we show results of three parameters comparing the effects of mutations in postnatal DRG cultures: number of moving mitochondria in 100µm, maximum speed and moving mitochondria size.

The first parameter, number of moving mitochondria in 100µm per one second, was not significantly altered by overexpression of *GDAP1* or missense mutations, either dominant or recessive, in wild type neurons (Figure R48, left graph).

In contrast, in *Gdap1*$^{-/-}$ DRG cultures the only mutation that was not able to cause any effect was *GDAP1* pR120Q (Figure R48, right graph, red bar). Apart from this, *GDAP1*-wildtype (+GDAP1 in graph, gray bar) and all rest of missense mutations altered the number of moving mitochondria. Rescue with *GDAP1*-wildtype decreased retrogradely moving mitochondria to wild type levels in *Gdap1*$^{-/-}$ cultures (black line). A decrease was also caused by introducing *GDAP1* pT157P and pR161H mutations; pT157P expression (purple bar) caused a decrease in moving mitochondria in both directions while pR161H (orange bar) expression only affected retrograde movement. Finally, an increase in anterogradely moving mitochondria was found when we expressed *GDAP1* pR120W (blue bar).

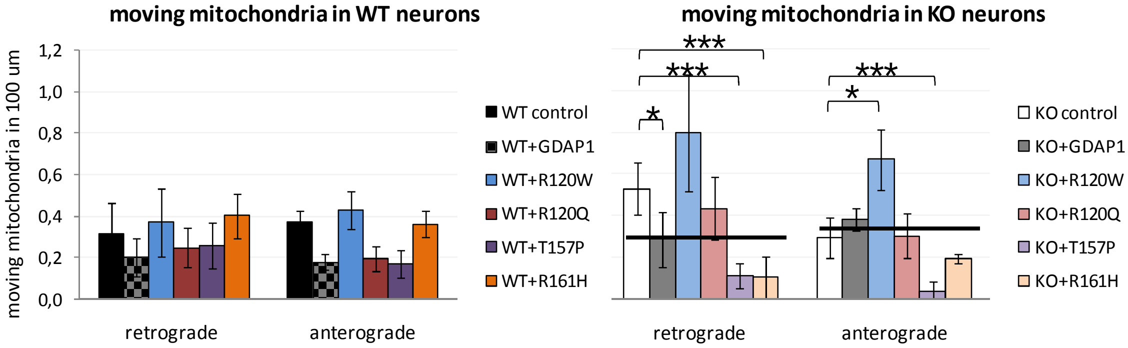

Figure R48. Number of moving mitochondria in 100µm per second in both Wild Type (left graph) and *Gdap1*$^{-/-}$ DRG cultures (right graph) when several *GDAP1* missense mutations were expressed. Each column colour represents microinjection of wild type or missense construct according to labels in wild type (WT) or *Gdap1*$^{-/-}$ (KO) neurons. Black lines are marking control wild type values. Asterisks are representing the p-values of proper statistic test (*<0.05; **<0.01; ***<0.001).

To investigate mitochondrial velocity we only show maximum speed although as we observed the same behaviour on average speed. In wild type neurons (Figure R49, left graph) maximum speed was only affected by *GDAP1* overexpression (squared black-gray bar), increased values were found in retrograde movement. Missense constructs did not induce any effect.

By contrast, rescued *Gdap1*$^{-/-}$neurons presented an increase in anterograde mitochondria velocity (Figure R49, right graph, gray bar). In addition, *GDAP1* pR161H (orange bar) mutation induced a change, decreasing retrograde velocity in *Gdap1*$^{-/-}$ cultures. The rest of mutations didn't have any effect on maximum speed of moving mitochondria.

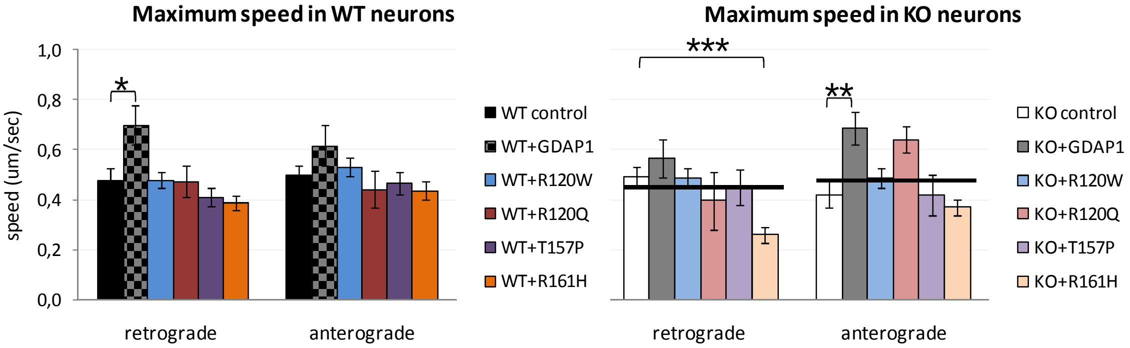

Figure R49. Maximum speed in both Wild Type (left) and *Gdap1*$^{-/-}$ DRG cultures (right) when several *GDAP1* mutations were expressed. Each column colour represents microinjection of wild type or missense construct according to labels in wild type (WT) or *Gdap1*$^{-/-}$ (KO) neurons. Black lines are marking control wild type values. Asterisks are representing the p-values of proper statistic test (*<0.05; **<0.01; ***<0.001).

Similarly to previous parameters, moving mitochondria size was not affected by expression of missense mutations neither by overexpression of *GDAP1* (squared black-gray bar, Figure R50, left graph).

Rescued *Gdap1*$^{-/-}$ neurons showed shorter moving mitochondria than deficient neurons in both directions (gray bar, Figure R50, right graph). The values of rescued neurons were close to wild type values (black line). In addition, missense recessive mutation *GDAP1* p.R161H (orange bar) caused shorter moving mitochondria in both directions, similar to recued neurons. Dominant mutation *GDAP1* p.R120W (blue bar) led also to shorter moving mitochondria but only in anterograde direction. Nevertheless, recessive mutation *GDAP1* p.R120Q (red bar) caused shorter moving mitochondria only in retrograde direction. On the other hand, expression of *GDAP1* p.T157P (purple bar) had no effect on moving mitochondria size.

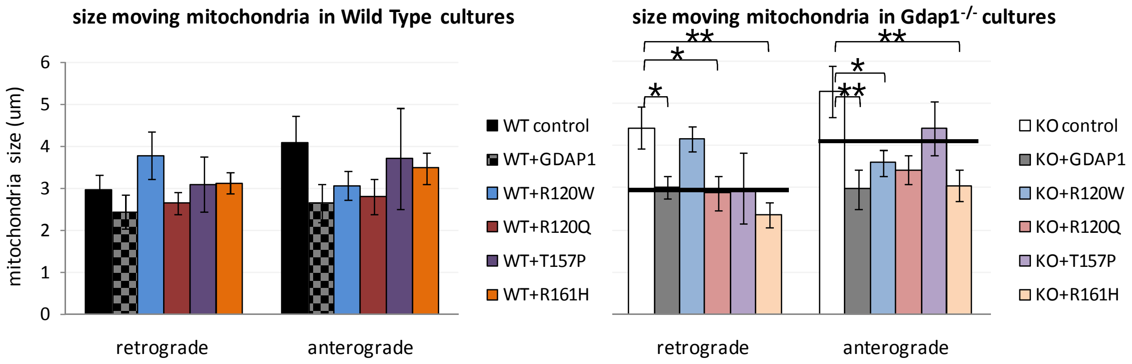

Figure R50. Moving mitochondria size in both Wild Type (left graph) and *Gdap1*$^{-/-}$ DRG cultures (right graph) when several *GDAP1* mutations were expressed. Each column colour represents microinjection of wild type or missense construct according to labels in wild type (WT) or *Gdap1*$^{-/-}$ (KO) neurons. Black lines are marking control wild type values. Asterisks are representing the p-values of proper statistic test (*<0.05; **<0.01; ***<0.001).

Taking together all the parameters we detected different profiles depending on DRG genotype (*Gdap1*$^{+/+}$ or *Gdap1*$^{-/-}$) and also on mutation.

In wild type neurons, *GDAP1* mutations had no effect on mitochondria in motion, velocity and mitochondria size (table R5). Neither dominants mutations.

In contrast, overdose of *GDAP1* caused a trend (p value 0.082) to decrease moving mitochondria (wt on the table R5). Excess of *GDAP1* also increased retrograde velocity and decreased anterograde size of those mitochondria in motion (wt on the table R5). Our results agree with previous data (Niemann et al. 2005; Pedrola et al. 2008).

WT neurons:	**+GDAP1**	**+GDAP1 pR120W**	**+GDAP1 pR120Q**	**+GDAP1 pT157P**	**+GDAP1 pR161H**
Retrograde Moving mitochondria in 100µm					
microinjected/WT	64%	n.s.	n.s.	n.s.	n.s.
p_value	0,082				
Anterograde Moving mitochondria in 100µm					
microinjected/WT	n.s.	n.s.	n.s.	n.s.	n.s.
p_value					
Retrograde Maximum speed					
microinjected/WT	146%	n.s.	n.s.	n.s.	n.s.
p_value	0,019				
Anterograde Maximum speed					
microinjected/WT	n.s.	n.s.	n.s.	n.s.	n.s.
p_value					
Retrograde Size moving mitochondria					
microinjected/WT	n.s.	n.s.	n.s.	n.s.	n.s.
p_value					
Anterograde Size moving mitochondria					
microinjected/WT	65%	n.s.	n.s.	n.s.	n.s.
p_value	0,072				

Table R5. Moving mitochondria parameters in wild type mice DRG cultures when different *GDAP1* mutations are microinjected. Percentage to wild type data has been calculated for each microinjection, either *GDAP1* or mutated *GDAP1*. p-values appear below percentage; n.s. means no significant value. This table is a summary of figures R48, R49, R50.

In *Gdap1*$^{-/-}$ DRG neurons all the *GDAP1*-mutations altered one or several parameters. In order to classify the mutations that caused same effects, percentages to null neurons and also to wild type neurons data were calculated for each microinjection (table R6). Null mice parameters are also show in the first column (blue).

Those mutations that corrected the defects produced by lack of GDAP1 in null mice are showed in green. Of course, *GDAP1* was able to restore them: it decreased the higher number of mitochondria moving retrogadely and decreased the size of mitochondria that were longer in null mice. In addition, *GDAP1* increased anterograde speed (yellow). Also in green, *GDAP1* pR120Q and pR161H restored only the mitochondrial size.

The mutation that had the same effect that loss of protein is highlighted in blue. *GDAP1* pR120W increased number and size of mitochondria moving in a retrograde direction. Additionally, pR120W mutation increased anterograde moving mitochondria and decreased size of these mitochondria in comparison with lack of protein.

Gain of function is labelled in red. *GDAP1* pT157P abolished the mitochondrial movement in an aggressive way (compared to wild type also) without modifying velocity or size of mitochondria.

Finally, a rare phenomenon is highlighted in purple. *GDAP1* pR161H decreased retrograde speed despite this was no altered in null mice. Moreover, pR161H mutation also abolished mitochondria in retrograde motion and, unexpectedly, mitochondria in motion size.

KO neurons:	**KO**	**+GDAP1**	**+GDAP1 pR120W**	**+GDAP1 pR120Q**	**+GDAP1 pT157P**	**+GDAP1 pR161H**
Retrograde Moving mitochondria in 100µm						
microinjected/KO	-	55%	n.s.	n.s.	22%	20%
microinjected/WT	166%	n.s.	250%	n.s.	36%	33%
Anterograde Moving mitochondria in 100µm						
microinjected/KO	-	n.s.	226%	n.s.	14%	n.s.
microinjected/WT	n.s.	n.s.	n.s.	n.s.	11%	n.s.
Retrograde Maximum speed						
microinjection/KO	-	n.s.	n.s.	n.s.	n.s.	53%
microinjected/WT	n.s.	n.s.	n.s.	n.s.	n.s.	54%
Anterograde Maximum speed						
microinjected/KO	-	162%	n.s.	n.s.	n.s.	n.s.
microinjected/WT	n.s.	138%	n.s.	n.s.	n.s.	n.s.
Retrograde Size moving mitochondria						
microinjected/KO	-	68%	n.s.	65%	n.s.	53%
microinjected/WT	149%	n.s.	140%	n.s.	n.s.	n.s.
Anterograde Size moving mitochondria						
microinjected/KO	-	56%	68%	65%	n.s.	58%
microinjected/WT	n.s.	n.s.	n.s.	n.s.	n.s.	n.s.

Table R6. . Moving mitochondria parameters in null mice DRG cultures when different *GDAP1* mutations are microinjected. Percentages to null neurons and also to wild type neurons data has been calculated for each microinjection. First column refers KO/WT (without any microinjection) percentage in order to compare the effect of mutations with the completely lack of protein. Colour data groups are explained on the text. n.s. means no significant differences. This table is a summary of figures R48, R49, R50.

3.3- Sciatic nerve explants

Mitochondrial movement.

Inference from primary cultures data is limited by dissociation of the cells, which eliminates tissue properties, the artificial culture environment, the short duration of the cultures and short axons. That is the why when possible it is preferable to study these mechanisms in the context of a live nerve.

To investigate the same mitochondrial parameters as above, we took advantage of mito-Dendra2 mice strain. All tissues isolated from these animals exhibit bright green fluorescence localized specifically at the mitochondrial compartment (http://jaxmice.jax.org/strain/018397.html). Breeding this strain with *Gdap1*$^{-/-}$ mice allowed us to assay axonal transport in the sciatic nerve of these animals, so no dissociation or culturing is necessary (see more detailed explanation in Material&Methods).

For this experiment we excised sciatic nerve carefully from presymptomatic 1 month old mice in order to avoid thick myelin sheet. Excised nerve was immediately located under the microscope, for no more than 1 hour, (Figure R51) to perform time lapse study. Imaging was carried out in the mid region of the excised nerve to avoid the effects of calcium influx through cut endings of the nerve.

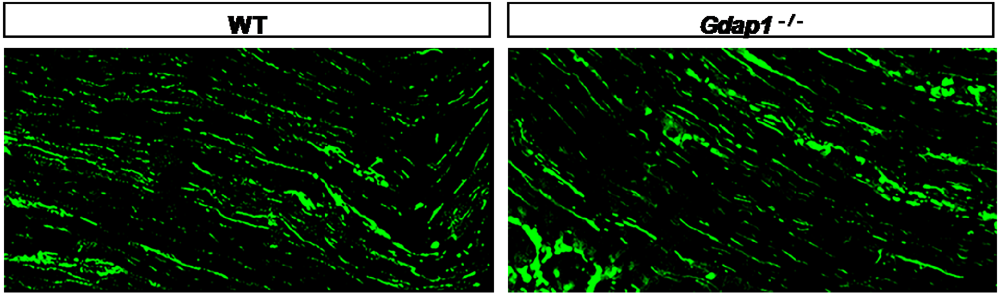

Figure R51. Representative images of sciatic nerve from WT/*mitodendra* and *Gdap1*$^{-/-}$*/mitodendra* mice. Mitochondria are fluorescent, easy to follow inside axons. Several individual axons were straightened from each time lapse (see next image).

Time lapse images from "ex vivo" mitochondria in sciatic nerve (Figure R52) were used to analyse the same parameters as those studied in postnatal DRG and SCG culture study (Andrews et al. 2010; Gilley et al. 2012).

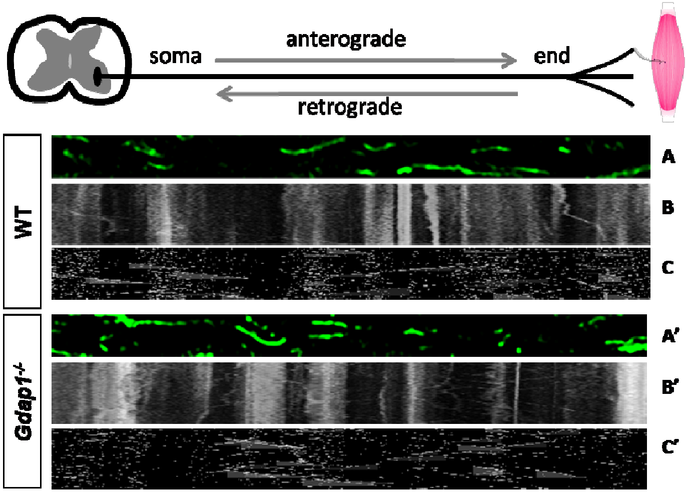

Figure R52. Representative images of sciatic nerve from WT/*mitodendra* and *Gdap1*$^{-/-}$ */mitodendra* mice. (a) Representative straightened axon (b) kymograph (time-distance graph) of mitochondria transport (c) Moving mitochondria from this kymograph identified using ImageJ plugin 'Difference tracker' (Andrews et al. 2010). Soma reference is draw on top

The number of mitochondria in movement inside peripheral axons of *Gdap1*$^{-/-}$ mice was similar to wild type. The percentage of moving mitochondria (moving mitochondria/total mitochondria) was equal between wild type and *Gdap1*$^{-/-}$mice (Figure R53, left graph). Moreover, there was no difference between genotypes in the number of moving mitochondria in 100 µm per second (Figure R53, right graph).

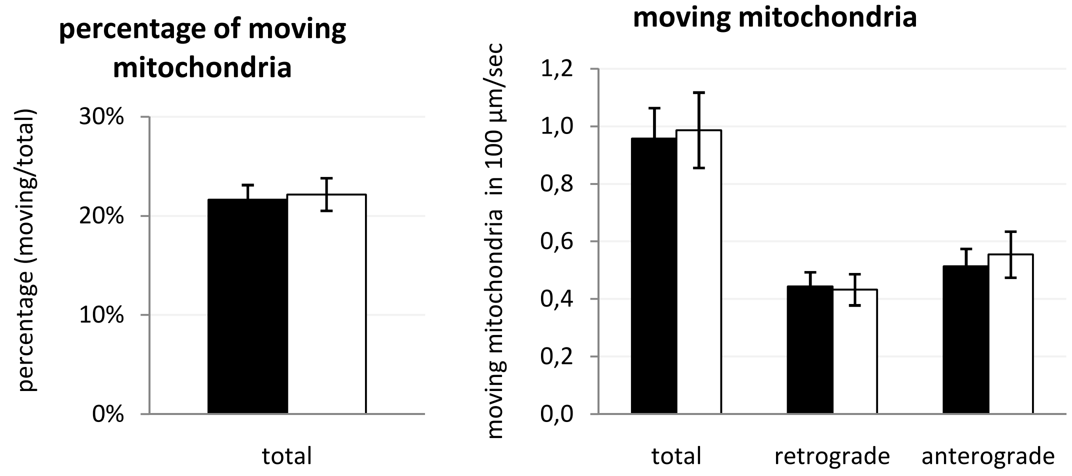

Figure R53. Percentage of total moving mitochondria (left graph) and number of moving mitochondria in 100µm per second (right graph) in sciatic nerve from 1 month old mice. The percentage was obtained by counting the number of moving mitochondria and dividing this number by the total number of mitochondria (static + moving). Average data (±SEM) of wild type mice are represented in black and *Gdap1*$^{-/-}$ in white.

These results were in agreement with previous data obtained in SCG cultures (table R7). However, they contrasted with those from DRG cultures (table R7) where we detected increased mitochondria in motion as well as increased retrograde moving mitochondria in 100µm.

	SCG	DRG	Sciatic nerve
Percentage of moving mitochondria			
KO/WT	n.s.	130% 0,082	n.s.
Retrograde Moving mitochondria in 100µm			
KO/WT	n.s.	166% 0,061	n.s.
Rescued/KO	46% 0,017	55% 0,033	
Anterograde Moving mitochondria in 100µm			
KO/WT	n.s.	n.s.	n.s.
Rescued/KO	53% 0,098	n.s.	

Table R7. Moving mitochondria parameters in *Gdap1*$^{-/-}$ SCG and DRG cultures and sciatic nerve. Percentage *Gdap1*$^{-/-}$/*Gdap1*$^{+/+}$ and Rescued/*Gdap1*$^{-/-}$ has been calculated for cultured neurites and axons inside nerve. p-values are shown besides percentage; n.s. means no significant value. This table is a summary of figures R41, R42, R53.

When we analysed average (total displacement of a particle / time tracked) and maximum (furthest displacement of each tracked particle between two frames) mitochondria velocities, we detected slower mitochondria in *Gdap1*$^{-/-}$ animals. However, the decrease is only detected in anterograde direction (Figure R54).

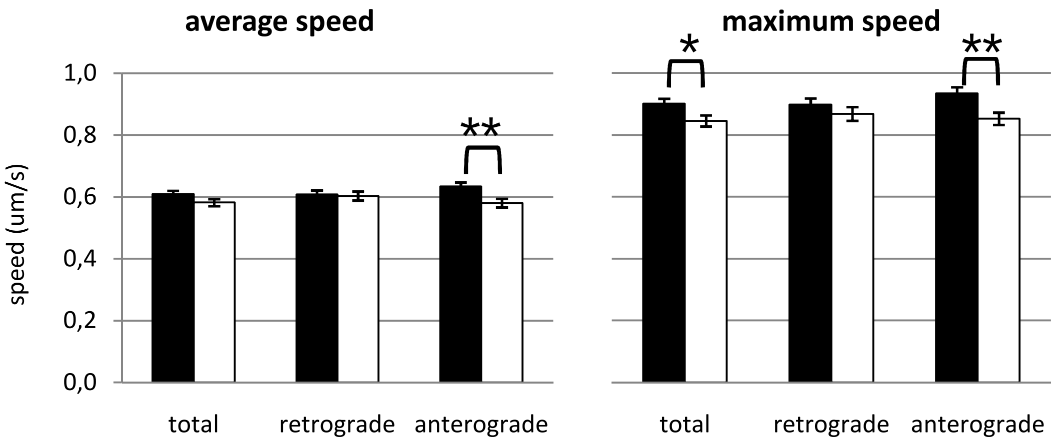

Figure R54. Average speed (left graph) and maximum speed (right graph) in sciatic nerve from 1 month old mice. Mean of average and maximum speed (±SEM) of wild type mice are represented in black and *Gdap1*$^{-/-}$ data in white. Asterisks are representing the p-values of proper statistic test (*<0.05; **<0.01; ***<0.001).

These results were in agreement with previous data obtained in SCG and DRG cultures (table R8). Retrograde velocities were in agreement with SCG data while anterograde velocities were similar to DRG neurons.

Table R8. Moving mitochondria velocities in *Gdap1*$^{-/-}$ SCG and DRG cultures and sciatic nerve. Percentage *Gdap1*$^{-/-}$/*Gdap1*$^{+/+}$ and Rescued/*Gdap1*$^{-/-}$ has been calculated for cultured neurites and axons inside nerve. p-values are shown besides percentage; n.s. means no significant value. This table is a summary of figures R43, R44, R54

	SCG	DRG	Sciatic nerve
Retrograde Average speed			
KO/WT	69% 0,002	n.s.	n.s.
Rescued/KO	n.s.	n.s.	
Anterograde Average speed			
KO/WT	61% 0,001	n.s.	92% 0,005
Rescued/KO	n.s.	176% 0,004	
Retrograde Maximum speed			
KO/WT	68% 0,000	n.s.	n.s.
Rescued/KO	n.s.	n.s.	
Anterograde Maximum speed			
KO/WT	67% 0,001	n.s.	91% 0,003
Rescued/KO	n.s.	162% 0,006	

Mitochondrial size.

In addition, we examined the size of moving mitochondria. *Gdap1* deficient mice showed longer mitochondria in the retrograde direction in their sciatic nerves than wild type animals (Figure R55, left graph). In contrast, such an increase in mitochondria size was not detected in static mitochondria (Figure R55, right graph).

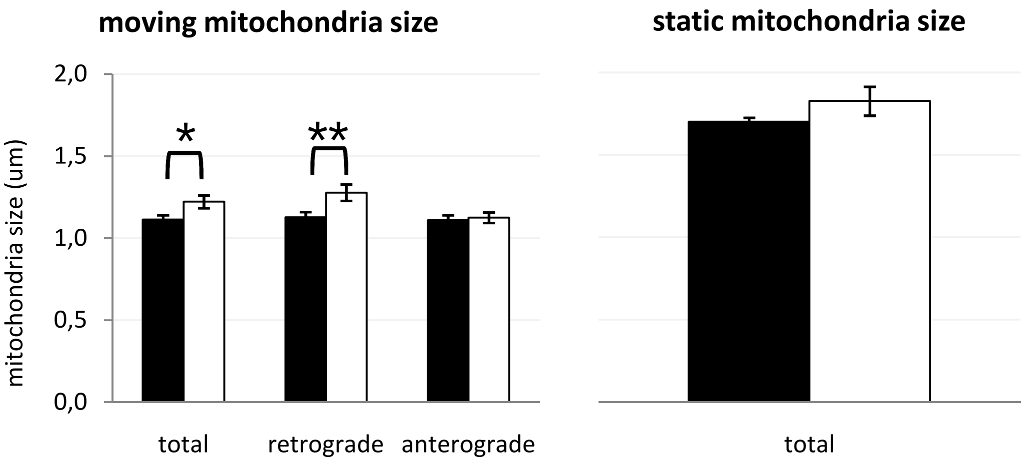

Figure R55. Moving mitochondria size (left graph) and static mitochondria size (right graph) in sciatic nerves from 1 month old animals. Wild type data are represented in black and $Gdap1^{-/-}$ in white. Asterisks are representing the p-values of proper statistic test (*<0.05; **<0.01).

These results were in agreement with previous data obtained in DRG cultures (table R9) where longer mitochondria were found in null mice neurons. However, in SCG cultures from $Gdap1^{-/-}$ mice we observed shorter ones.

Table R9. Mitochondria size in $Gdap1^{-/-}$ SCG and DRG cultures and sciatic nerve. Percentage $Gdap1^{-/-}$/$Gdap1^{+/+}$ and Rescued/$Gdap1^{-/-}$has been calculated for cultured neurites and axons inside nerve. p-values are shown besides percentage; n.s. means no significant value. This table is a summary of figures R45, R46, R55.

	SCG	DRG	Sciatic nerve
Retrograde Size moving mitochondria			
KO/WT	77% 0,067	149% 0,046	113% 0,013
Rescued/KO	n.s.	68% 0,049	
Anterograde Size moving mitochondria			
KO/WT	n.s.	n.s.	n.s.
Rescued/KO	n.s.	56% 0,004	
Size Static mitochondria			
KO/WT	117% 0,011	n.s.	n.s.

Discussion

1.- Mouse model suitable for *GDAP1*-CMT disease

There are few animal models for the *GDAP1* form of CMT. Several fly models have been developed by Dr Galindo group (Del Amo et al. 2015), demonstrating that specific overexpression and knockdown of *Gdap1* in retinal cells induce neuronal loss in an age-dependent fashion.

Regarding mouse specifically, apart from our *Gdap1* null model there is just one other developed by Dr Suter group and reported during the course of this project (Niemann et al. 2014). In contrast to our null mouse model, which was generated by deleting the first of six exons of *Gdap1* in order to ablate the expression, Niemann *et al*. generated a mouse deleting the fifth exon. This led to a truncated protein that was unstable. Both *Gdap1*$^{-/-}$ mouse models are fertile, with no disability and healthy offspring. This contrasts with mice lacking other mitochondrial fusion-fission proteins, such as *Drp1* (Wakabayashi et al. 2009), *Opa1*(Alavi & Fuhrmann 2013) and *Mfn1* or *Mfn2* (Chen et al. 2003) null mice models, which have embryonic lethality.

To be useful as a model, it is important that animals mimic disease hallmarks although we know that sometimes this is particularly difficult in mouse models of neuropathies. *GDAP1*-CMT patients suffer a chronically progressive motor neuropathy beginning in early childhood and resulting in severe disability at the end of their first decade (Baxter et al. 2002; Cuesta et al. 2002; Sevilla et al. 2003). Our *Gdap1* null mouse presents motor deficits in an age-dependent trend and those deficits are easily quantifiable by rota-rod test (figures R8, R9) and walking track analysis (figure R11, tables R1, R2). In addition, our mouse model also shows the "pes cavus" phenotype (figure R6). However, muscle wasting is not present at 12 months old (figure R12) whereas damaged muscle fibres have been detected (figure R13).
The Niemann mouse model showed no signs of peripheral neuropathies. In 13 month old mice, same motor studies, which allowed us to detect the locomotion disability, revealed no significant differences between mutant and control animals (Niemann et al. 2014).

In addition to motor disability, mild to severe sensory loss is observed in *GDAP1*-CMT patients; particularly affecting proprioception, vibration and touch (Baxter et al. 2002; Cuesta et al. 2002; Sevilla et al. 2003). Looking for these impairments in our mouse model we studied the histology of DRG where the soma of neurons that innervate skin and muscle spindles are located (Lallemend & Ernfors 2012). DRGs were studied by histology and no abnormalities have been found even in old mice (figure R30). However, the molecular and cellular environment is disrupted when DRG cells are disaggregated and cultured and cultures are maintained for a limited duration with much shorter axons than *in vivo* (discussed below in points 5 to 8). So far, no sensory tests were studied in our mouse model. However, Dra Satrustegui's group is doing sensory test to our mouse model and they have found disabilities of Gdap1$^{-/-}$.
In 13 month old mice of the Niemann model, sensory studies revealed no significant differences between mutant and control animals (Niemann et al. 2014).

	Niemann_2014	**Present work**
Mouse Generation:		
- exon deleted	Exon 5	Exon 1
- expected product	Transpliced mRNA	No mRNA
Phenotype:		
- motor behaviour	No phenotype at 13 mo	Rota-rod defects at 3mo
- NCV	75% at 19 mo	94% at 5mo
- CMAP proximal stimulation	66% Amplitude at 19mo Duration not affected	76% Amplitude at 5mo 115% Duration at 5mo
- CMAP distal stimulation	No alteration in amplitude	63% Amplitude at 5mo

Table D1. *Gdap1* mice models comparison. Principal features in mouse generation and phenotype of both Gdap1 mice already published. Percentages represent null mice data divided by control mice data.

2.-*GDAP1*$^{-/-}$ mice model the axonal form of CMT

As in patients studies (Cuesta et al. 2002) *Gdap1* null mice present slightly slower MNCV at 5 months old (a decrease of 6%, figure R18) and reduction in CMAP amplitude and area (figure R19). In addition, lower density of fibres was found (figure R23) in agreement with axonal CMT forms (Cuesta et al. 2002; Sevilla et al. 2003). Other CMT2 models corroborate these findings. As an example, HSPB1^{S135F} and HSPB1^{P182L} neuron expressing mice also present a significant decrease in the number of axons in distal parts of the sciatic nerve at 10 months old (d’Ydewalle et al. 2011).

In contrast, onion blubs were not observed in electron microscopy images of sciatic nerve (figure R22) and g-ratio was equal to controls (table R3) at 5 months old, discarding demyelinating form (Tazir et al. 2014).

3.-*Gdap1* family genes are expressed in mouse

GDAP1 is expressed in neuronal mouse tissues (figure R2) in agreement with previous studies (Niemann et al. 2005). No protein expression was detected in skeletal muscles (figure R2).

Deletion of first of six exons of *Gdap1* (figure R1) is enough to ablate its expression. Even short transcript couldn't be detected in null mouse model (figure R5). In contrast, deletion of fifth exon in Niemann model results in a transcript form with a transplicing form exon 4 to exon 6 (Niemann et al. 2014).

Protein expression is dependent on genetic charge, heterozygous animals presents less protein amount that wilt types (figure R3).

Gdap1 family member *Gdap1L1* is also expressed mainly in CNS (figure R5). Although we didn´t check protein expression, reverse transcriptase analysis agree with similar studies that don't find expression in PNS (Niemann et al. 2014).

4.- Lack of *Gdap1* produces axonopathy

Motor defects already discussed in the first point need to be due to problems in long distal peripheral nerves as GDAP1 is not expressed in muscles (figure R2). In mice, sciatic nerve is the longest nerve (Krinke et al. 2014) that innervates hind limb muscles.

Detailed electrophysiological analysis of *Gdap1*$^{-/-}$ sciatic nerve revealed alterations in MNCV and CMAP parameters (figures R18, R19, R20, R21). As discussed above, a slight reduction of MNCV as we find here, together with reduced CMAP amplitude and area are signs of an axonal form of CMT. In addition, longer durations reflect selective slowing of some motor fibres (Katirji et al. 2013). Shorter latencies are more difficult to explain, as normally an increase in latencies reflects the nerve conduction slowing of the fastest fibres (Tankisi et al. 2012).

It's important to remark that all these alterations were found in 5 months old mice but not in 2 month old. This indicates that the neurodegenerative part of the axonopathy is progressive, again similar to the phenotype in patients.

Alterations in electrophysiological outcomes can be explained by loss of fibre density in sciatic nerve (figure R23). In addition, asynchrony reflected by increasing CMAP duration may be explained by the change in the fibre size distribution found in CMT mice (figure R24). Although average axon size is no statistically different between control and CMT mice (table R4), we found a slightly loss of small fibres and gain in bigger ones when we studied deeply (figure R24). This fact could also explain why smaller CMAP latencies were found in null animals.

Interestingly opposite findings have been reported for another fusion related protein mouse model. MFN2 p.R94Q mice, which develop locomotor impairments and gait defects at 5 months old, presents an age-related shift in the size of myelinated axons leading to an over-representation of axons smaller than 3.5 um (Cartoni et al. 2010).

No other axonal extrinsic abnormalities as demyelination (table R3 and figure R22) were found in our CMT mouse model. However, when we studied axons in more depth, intrinsic alterations were found. Mitochondria inside *Gdap1*$^{-/-}$ mouse sciatic nerve axons were longer that the controls (figures R25, R26, R55). This fact will be discussed more extensively in point 5.

Both proximal and distal ends of sciatic nerve axons were also studied in detail. In the distal part, terminal ends of axons start to die back leading to denervation in the gastrocnemius muscle at some point between 5 and 12 months. Although the total number of NMJ endplates was not altered (figure R14), their occupation by axonal terminals was lower (figures R15, R16).It is well established that the synaptic connections between motor axons and muscle are shaped by nerve activity; impaired post-synaptic activity at neuromuscular synapses delays the withdrawal of presynaptic terminals and synapse elimination (Bloch-Gallego 2015). In addition, abnormalities such as retraction bulbs in the most distal part of the nerve, near to NMJ, were found only in old CMT mice (figure R18).

Interestingly, denervation of NMJ was also observed in adult zebra fish expressing MFN2 pL285X mutant, along with clear alterations in swimming (Chapman et al. 2013).

Denervation of leg muscles is consistent with the increase of plantar length (PL) and decrease of toe spreading (TS) observed in footprint records (figure R11 and table R2) (Wiethölter et al. 1990). The absence of more severe findings in muscles could be explained by the short length of mouse leg nerves relative to humans.

At the proximal end of the axon, the somas of motor neurons located in ventral horn of lumbar spinal horn are also affected as suggested the pyknotic aspects of neuronal somas in *Gdap1*$^{-/-}$ animals (figure R27). Loss of "healthy" MNs (figure R28) can be attributed to increased catalase and Bax expression (figure R29). However, western blot experiments were done with the whole lumbar spinal cord protein extracts, so it is difficult to correlate apoptosis and oxidative stress, revealed by Bax and catalase increase, with pyknotic motor neurons.

In addition, new roles for Bcl2 family have been described linking those proteins with mitochondrial dynamics (Saez-Atienzar et al. 2016). Apoptosis and mitochondrial dynamics are related: 1) BAX interacts with components of the mitochondrial fission/fusion machinery; 2) deficiencies in mediators of mitochondrial fission/fusion and cristae remodelling influence the kinetics of apoptosis; mitophagy is related to mitochondrial dynamics: (a) since a fragmented mitochondrial network is necessary (though not sufficient) for efficient mitophagy, DRP1 and MFN1/2 indirectly regulate mitophagy, both positively and negatively; (b) PINK1/Parkin targets MFN1 and 2 for degradation to promote mitochondrial fission. At the same time, mitophagy is related to apoptosis (Li & Dewson 2015).

An alternative explanation for increased catalase and Bax will be discussed in point 9.

5.- GDAP1 is implicated in mitochondrial dynamics

It has been demonstrated that GDAP1 is a fission-inducing factor which promotes mitochondrial fragmentation without inducing cell apoptosis, changes in mitochondrial transmembrane potential or interfering in mitochondrial fusion. Moreover, transfections with *GDAP1*-specific RNAi led to an increase of cells with a tubular mitochondrial morphology compared with untransfected or control transfected cells (Niemann et al. 2005; Pedrola et al. 2008; Niemann et al. 2009). Also fly models confirmed that overexpression of *Gdap1* caused small mitochondria and interference of Dm*Gdap1* produced longer mitochondria (Del Amo et al. 2015).

To test if lack of *Gdap1* also alters mitochondrial dynamics in our mouse model we performed experiments to check mitochondrial morphology in different tissues. As already mentioned in point 4, the sciatic nerve ultrastructure analysis by electron microscopy showed a higher number of mitochondria per section in null mice axons (figure R25). As there was no increase of mitochondrial biogenesis in sciatic nerve extracts we concluded that the increase of mitochondria number per section is due to elongated mitochondria that could be sectioned several times(figure R26). In addition, confirmation of the presence of longer mitochondria due to deficiency of *Gdap1* in sciatic nerve axons was performed in sciatic nerve explants using mice with fluorescently-labelled mitochondria. *Gdap1*$^{-/-}$mice presented longer mitochondria moving back to soma -in retrograde direction- (increase of 13%, figures R52, R55 and table R9). Static mitochondria were not different form controls.

We also observed longer mitochondria in retrograde motion in DRG cultures from null animals relative to wild type (increase of 49%, figures R40, R45, R46 and table R9). In addition, when we rescued those sensory neurons by microinjecting *Gdap1* mitochondria became shorter than in non-rescued null cultures (KO), travelling in both directions (decrease of 32% in retrograde way and 44% anterogradely, (figure R45 and table R9). Again, static mitochondria were not different form controls.

Interestingly, when we studied moving mitochondria in SCG cultures we found the opposite. Shorter mitochondria were moving in a retrograde direction in null neurons (decrease of 23%, trend in figure R45 and table R9) and longer ones were found to be increased in the static pool (increase of 17%, figure R46 and table R9). The relevance to pathogenesis is that SCG are not affected in CMT. In addition, SCG belongs to sympathetic nervous system (SNS) (Jackson & Tourtellotte 2014). Impairments in mitochondrial dynamics affect different cell types in different individuals in a different way depending on the individual's unique profile of intracellular and extracellular stress factors (Alavi & Fuhrmann 2013). It maybe that SCGs have a mechanism to avoid the formation of longer mitochondria and this is why these neurons are not affected in the same way. Smaller mitochondria moving in a retrograde direction could represent a mitophagy marker.

In agreement with our results, opposite findings has been described for fusion related proteins. As an example, DRG cultures from MFN2$^{R94Q/R94Q}$ mice presents shorter mitochondria than control ones (Misko et al. 2010).

Mitochondrial fission and fusion occupies a central position in mitochondrial quality control and it processes different intracellular and extracellular parameters in order to accommodate cell homeostasis and cell fate by several measures: a) Mitochondrial network morphology changes to either a more filamentous or more fragmented state to adapt mitochondrial function to actual energetic and metabolic demands of the host cell. b) Fusion of dysfunctional mitochondria to functional mitochondria can attenuate damage to mitochondrial proteins, lipids, and mtDNA. c) Inhibition of mitochondrial fusion targets single dysfunctional mitochondria to the mitochondrial autophagy pathway. d) Mitochondrial fragmentation, mitochondrial outer membrane permeabilization, and cytochrome *c* release signals severely impaired host cells to undergo cell death. According to this, mitochondrial fusion maintains mitochondria by attenuating mitochondrial damage as well as by protecting from mitochondrial autophagy. Moreover mitochondrial fusion antagonizes cell death signalling (Alavi & Fuhrmann 2013).

6.- GDAP1 is implicated in mitochondrial transport

GDAP1 has been also linked with mitochondrial motility. Depletion in human neuroblastoma cells induced the increase of organelle motility but without increase of tubular mitochondrial morphology (Pla-Martín et al. 2013).

Similar results were obtained when we studied mitochondria motility in DRG cultures. An increased percentage of moving organelles were found in null neurons (30% more, trend in figure R41 and table R7). In detail, the increase was due to a higher number of mitochondria moving retrogadely in *Gdap1*$^{-/-}$ cultures in comparison to wild type ones (increase of 66%, trend in figure R42 and table R7). This data is supported by the opposite effect found when we rescue *Gdap1*$^{-/-}$ neurons. Microinjection of *Gdap1* into null neurons decreased the number of mitochondria that were moving in retrograde direction (decrease of 45%, figure R42 and table R7).

In contrast, no alteration in motile mitochondria was found either in sciatic nerve explants (figure R53 and table R7) or in SCG cultures from null mice (figure R41, R42 and table R7). However, a decreased number of moving mitochondria in both directions was found in rescued SGC cultures in comparison with null not rescued ones (decrease of 54% retrogadely and a trend of 47% anterogradely, figure R42 and table R7).

In agreement with our results, opposite findings has been described for fusion related proteins. DRG neurons derived from MFN2 knockout mice transfected with MFN2$^{R94Q/R94Q}$had disrupted both anterograde and retrograde mitochondrial transport (Misko et al. 2010). In MFN2$^{L285X/L285X}$ zebra fish neurons only retrograde transport was selectively impaired (Chapman et al. 2013).

In addition to studying motile mitochondria, we were also interested to determine moving velocities in our mouse model at diverse levels. Sciatic nerve explants from *Gdap1*null mice showed lower velocities than controls, average (decrease of 8%, figure R54 and table R8) and maximum (decrease of 9%, figure R54 and table R8), in anterograde direction.

Despite SCG not being affected in CMT patients, same findings were replicated in sympathetic ganglion cultures from null mice. Reduction of around 31-39% in average and maximum velocities was observed in retrograde and anterograde direction (figure R43, R44 and table R8). However, those alterations were not detected in *Gdap1*$^{-/-}$ DRG cultures but rescued cultures presented opposite values; showing a increase in anterograde velocities, average (increase of 76%, figure R43 and table D5) and maximum (increase of 62%, figure R44 and table R8).

Interestingly, similar findings have been described for fusion related proteins. DRG neurons derived from MFN2 knockout mice transfected with MFN2$^{R94Q/R94Q}$moved at slower velocities in the anterograde and retrograde directions (Misko et al. 2010). In MFN2$^{L285X/L285X}$ zebra fish neurons only retrograde speed was reduced (Chapman et al. 2013).

Mitofusins has been described as adaptor of Miro (Tang 2015). In *Drosophila*, the Milton/Miro complex mediates the binding of microtubule-based motors to mitochondria. Miro associates with the outer mitochondrial membrane via a transmembrane domain and recruits Milton, which binds directly to KHC (kinesin heavy chain). Recently, the mammalian homologs of Milton, TRAK1 and TRAK2, were shown to associate with the retrograde motor complex via dynactin. Interestingly, N-terminal TRAK binds to both dynactin and KHC, and this potentially mediates bidirectional transport of mitochondria. By contrast, depletion of TRAKs results in arrest of the anterograde and retrograde moving pools of mitochondria in both axons and dendrites, suggesting that TRAKs mediate processive transport in a regulated manner that remains to be elucidated fully (Fu & Holzbaur 2014). NDE1 and GSK3β associate with TRAK1. NDE1 promotes retrograde axonal mitochondrial movement and GSK3β promotes anterograde mitochondrial transport (Ogawa et al. 2016).

As defective fusion -MNF2- and fission -GDAP1- produce slower mitochondria in retrograde and anterograde direction respectively; it is no absurd thinking that both proteins are involve in transport mitochondria along axons apart from its role mitochondrial dynamics. GDAP1 knock-down clones (with 40% and 80% protein reduction) of the human neuroblastoma SH-SY5Y cell line have problems to differentiate due to lack of GSK3β phosphorylation (Pla-Martín 2012). Perhaps GDAP1 interacts and/or activates GSK3β by interaction with TRAK in a similar way to mitofusins. This idea will be discussed in point 9.

7.-*GDAP1* mutations affect to mitochondrial dynamics and transport

A high number of mutations has been found along GDAP1 gene; some of them has been reported as CMT causing mutations and some as a non pathogenic (table A2 and A3).

With the aim of better understanding the pathogenic effect of mutated *GDAP1* in CMT patients, we investigated the effect of several *GDAP1* missense mutations (Figure R47) (Pedrola et al. 2008; Pla-Martín et al. 2013) on mitochondrial parameters depending on neurons genotype.

When we express mutations of *GDAP1* in wild type DRG cultures (table R5) only overexpression of *GDAP1* alters the parameters decreasing number of mitochondria in retrograde way (trend with a p value of 0.082). In addition, *GDAP1* increases retrograde velocity and decreases anterograde size of those mitochondria that are moving. It is interesting how the overdose of non-mutated protein also causes alterations.
A increase in fragmented mitochondria were found in similar experiments on COS-7 cells which doesn't express GDAP1 (Niemann et al. 2005; Pedrola et al. 2008).

The absence of effect by dominant mutations pR120W and pT157P was unexpected. However, it is possible that the presence of wild type GDAP1 in neurons avoid any effect of microinjected mutation.

When we express mutations of *GDAP1* in *Gdap1*$^{-/-}$ DRG there are more parameters altered. There are mutations that correct the defects produces by lack of GDAP1 in null mice (green highlighted on table R6) . Of course, *GDAP1* is able to restore all of them: it decreases the higher number of mitochondria moving retrogradely and decreases the size of mitochondria that were longer in null mice. In addition, non mutated protein also increases anterograde speed although speed is not reduce in DRG cultures of *Gdap1*$^{-/-}$ mice (green highlighted on table R6).
Surprisingly, *GDAP1* pR120Q expression in null neurons also is able correct one defect due to lack of GDAP1. This mutated protein reduce the increased size of retrograde moving mitochondria (green highlighted on table R6) as well as also reduce the size of anterograde moving mitochondria that were not altered in knockout cultures.
These data contrast with the early and severe form of CMT that develop patients harbouring this recessive mutation (Boerkoel et al. 2003).

We also decide to study another mutation at the same position but with dominant inheritance, pR120W. CMT patients harbouring this mutation have a mild phenotype (Claramunt et al. 2005) and even are asymptomatic (Zimon et al. 2012).
Although mild phenotype, *GDAP1* pR120W seems to doesn't restore any defect on mitochondrial movement when it is express in DRG cultures of *Gdap1*$^{-/-}$ mice. Its data are quite similar to lack of protein (blue highlighted on table R6) but also increases velocity and reduces size of anterograde mitochondria in motion.

Dominant mutation pT157P has a "arresting" effect on mitochondria. This mutation decreases so abruptly the increased retrograde moving mitochondria in null neurons and also anterograde moving that were not altered. The decrease is so strong that there is a lower percentage of mitochondria in motion even if we compare with control mice neurons (red highlighted on table R6). However no effect on velocity or size was found.

That "arresting" effect on mitochondria could explain the severe phenotype presented in *GDAP1* pT157P patients (Claramunt et al. 2005).

Another severe form of *GDAP1* related CMT is caused by the recessive inherited mutation pR161H (Baxter et al. 2002). The expression of mutated protein in null neurons also stops retrograde moving mitochondria in a similar way to pT157H mutation. In addition, pR161H decreases retrograde speed and also it is able to restore mitochondria in motion size.

8.- GDAP1 is implicated in microtubule cytoskeleton stabilization

Loss of GDAP1 produces cytoskeleton instability due to interfering to correct PMTs. Decreased acetylation (figures R35, R36) and increased tyrosination state (trend, figures R37, R38) may be the reason because DRG cultured neurons are not able to grow properly, presenting smaller soma (figure R33) and shorter neurites (figure R34) than the controls. Even so, this instability doesn't affect to neurites output (figure R32).

Other CMT mouse models, CMT2F HSPB1^{S135F} and HSPB1^{P182L} neuron expressing mice as CMT2F model, also show a marked decrease in acetylated α-tubulin abundance in peripheral nerves (d'Ydewalle et al. 2011).

Interestingly, an increase of a-tubulin acetylation induced by pharmacological inhibition of histone deacetylase 6 (HDAC6) corrected the axonal transport defects caused by HSPB1 mutations and rescued the CMT phenotype (d'Ydewalle et al. 2011).

Lysine acetylation is a key post-translational modification known to regulate gene transcription, signal transduction, cellular transport and metabolism. Lysine deacetylases (KDACs) superfamily in mammals currently holds eighteen members. A core division based on homology with yeast KDACs separates 'classical HDACs' (zinc-dependent, Rpd3/Hda1 homologues) from 'sirtuins' (NAD+-dependent, Sir2 homologues) (Matsushima & Sadoshima 2015).

Cytosolic HDAC6 deacetylates tubulin, cortactin and HSP90, regulating axonal trafficking, cell motility and degradation of misfolded proteins. SIRT2 shares α-tubulin deacetylase activity with HDAC6, and has been suggested as the main microtubule deacetylase in mature neurons. SIRT1 deacetylates and activates the transcriptional co-activator PGC-1α, a master regulator of mitochondrial biogenesis (Guedes-Dias & Oliveira 2013).

A mouse model of another neurodegenerative disease, Amyotrophic lateral sclerosis, also presents a reduction in neurite length as well as mitochondrial fragmentation and impairment of mitochondrial transport. In this model, SIRT3 and PGC-1α protect against mitochondrial fragmentation and neuronal cell death by mutant SOD1^{G93A} (Song et al. 2013).

SIRT3 is the main deacetylase in the mitochondria, where it regulates oxidative phosphorylation, protein synthesis and multiple metabolic pathways (Guedes-Dias & Oliveira 2013). Effects of Sirt3 are mediated by the activation of FoxO3-dependent transcription of catalase and MnSOD, suppression of ROS-induced Ras activity, MAPK/ERF, and Akt/PI3Ksignalling (Matsushima & Sadoshima 2015).

It would be interesting testing Sirt3 activation in *Gdap1*$^{-/-}$ mice. Activation of Sirt3 could explain why motor neurons in spinal cord are nor dying (figure R29). Activation of Bcl-xL could blocks the increased Bax (figure R) and deacetylation of FoxO3a would increase catalase (figure R29).

9.- Role of GDAP1 in mitochondrial transport, homeostasis and pathology in neurons

As *GDAP1* was identified in a Neuro2a mouse neuroblastoma cell line differentiated by transfection of GD3 synthase (a2,8sialyltransferase) cDNA (Cassereau et al. 2011), there is another mouse model to take into account for comparisons with *Gdap1* null mice. Complex ganglioside knockout mouse (*GalNAcT*$^{-/-}$) was engineered to lack a key enzyme in complex ganglioside biosynthesis (GM2/GD2 synthase) and express only the simple ganglioside molecular species GM3 and GD3. *GalNAcT*$^{-/-}$mice develop significant and progressive behavioural neuropathies, including deficits in reflexes, strength, gait, coordination and balance (Chiavegatto et al. 2000). *GalNAcT*$^{-/-}$mice also display decreased myelination, axonal degeneration in both the central and peripheral nervous systems (Ma et al. 2003; Sheikh et al. 1999).

	GalNAcT$^{-/-}$mouse model	***Gdap1*$^{-/-}$ mouse model**
Phenotype:		
- motor behaviour	Limb clasping at 8mo Rota-rod defects at 8mo	Limb clasping at 3mo Rota-rod defects at 3mo
- walking defects	Reduced Stride Length at 8mo Increased Plantar Length at 8mo	Reduced Stride Length at 5mo Increased Plantar Length at 5mo
- MNCV	Slightly reduced at 3mo	Slightly reduced at 5mo
Electron microscopy		
- CNS**:**	Degenerating fibres Increased unmyelinated fibres and axon size (3mo)	
- PNS	Degenerating fibres Decreasing neurofilament spacing (3mo)	Loss of myelinated fibres. Shift in axon sizes (5mo)

Table D2. Mice models comparison. Principal features in phenotype of both Complex ganglioside knockout mouse (*GalNAcT*$^{-/-}$) and Ganglioside-induced differentiation-associated protein-1 knockout mouse (*Gdap1*$^{-/-}$)

Early studies on isolated neurons indicated an enrichment of gangliosides in terminal axons and synaptic endings, suggesting a role in formation, development and maintenance of the nervous system. The importance of gangliosides in normal functioning and integrity of the nervous system and in neurodevelopment and neural regeneration has since been demonstrated.

At the cellular level, the ability of exogenously applied gangliosides to potentiate neurite outgrowth in primary neurons, sensory ganglia and neuroblastoma cell lines, and axonal sprouting in regenerating axons has long been established. The ganglioside 9-*O*-acetyl *GD3* has been implicated in glial-guided neuronal migration and neurite outgrowth in both the developing and adult rat nervous system, and in facilitation of axonal growth and Schwann cell-induced myelination during both development and regeneration of mouse peripheral nerve. Additionally, gangliosides can enhance or regulate cell survival. They have been shown to be neuroprotective against toxic insult, anti-apoptotic during neural cell differentiation, and pro-apoptotic during neural cell proliferation (Palmano et al. 2015).

Human neuroblastoma GDAP1 knock-down clones has also problems to differentiate properly (Pla-Martín 2012). Maybe *GDAP1* is necessary to orchestrate all this change in cell morphology.

If we look for one studied protein that could orchestrate big changes in cell morphology, mitochondria distribution and dynamics the proteins Miro/Milton come to our mind. Indeed, Miro1 KO axons exhibit a reduction in overall retrograde velocity compared with WT (Nguyen et al. 2014).

The evolutionarily-conserved mitochondrial Rho (*MIRO*) small GTPase which is specifically associated with the mitochondria and via a hydrophobic transmembrane domain. At the mitochondria, *MIRO* regulates mitochondrial homeostasis and turnover. In metazoans, *MIRO* regulates mitochondrial transport and organization at cellular extensions, such as axons, and, in some cases, intercellular transport of the organelle through tunnelling nanotubes. Recent findings have revealed a myriad of molecules that are associated with *MIRO*, particularly the kinesin adaptor Milton/TRAK, mitofusin, *PINK1* and Parkin, as well as the endoplasmic reticulum-mitochondria encounter structure (*ERMES*) complex. The mechanistic aspects of the roles of MIRO and its interactors in mitochondrial homeostasis and transport are gradually being revealed. On the other hand, *MIRO* is also increasingly associated with neurodegenerative diseases that have roots in mitochondrial dysfunction (Tang 2015).
The next table (table D3) summarizes all known partners of MIRO involved in different functions: anterograde and retrograde motors o adaptors, mitochondrial fusion (*MFN*), mitosis segregation, neural development and signalling pathways, stress response and protein degradation.

Interacting protein	**Nature of partner**	**Function/remarks**
Milton (Dm) TRAK1 and 2	Mitochondrial kinesin motor adaptors	Microtubule-based mitochondrial transport
Kinesin 1/KIF5	Kinesin family, microtubule-based motor protein	Microtubule-based transport (anterograde)
Dynein	Microtubule-based motor protein	Microtubule-based transport (retrograde)
Mitofusin 1 and 2	Dynamin-like GTPases	Mitochondrial fusion
Cenp-F	Centromeric protein	Kinetochore function and chromosome segregation in mitosis
DISC1	Multifunctional scaffold protein	Neural development and multiple signaling pathways, such as Wnt and mTOR; associated with schizophrenia & depression
HUMMR	Hypoxia-inducible protein	Axonal mitochondrial transport, particularly in response to hypoxia
PINK1	Ser/Thr protein kinase that phosphorylates ubiquitin	Regulator of mitochondrial stress response and mitophagy
Parkin	E3 ubiquitin ligase	Important component of the ubiquitin-proteasome system of protein degradation; MIRO is a substrate of Parkin

Table D3. Summary of known MIRO interacting partners and their functions. Adapted from Tang 2015).

Similar with MIRO, GDAP1 also have potential partners (tableD4) with a wide range of functions which could explained all the alterations found in *Gdap1*$^{-/-}$.

Interacting protein	Nature of partner	Function/remarks	clons
Microtubule-based transport (anterograde)			
Caytaxin	Kinesin binding	apoptosis, mitochondrial distribution	3
Microtubule-based transport (retrograde)			
RAB6B	GTPase activiy	retrograde transport endosome to Golgi and Golgi to ER	5
PIKFYVE2	ATP binding	retrograde transport endosome to Golgi	3
TUBB	GTPase activiy. Ubiquitin protein ligase binding	microtubule-based process	1
Actin-based organization			
WASP	actin binding	actin cytoskeleton organization	1
Neurofilament-based organization			
INA	neurofilament	neurofilament cytoskeleton organization, development	1
Segregation in mitosis			
CEP250	protein kinase binding	centriole-centriole cohesion	3
CCDC123	cetrosomal protein	organelle organization	2
Signalling pathways and neuronal development			
MESDC2	chaperone	Wnt signalling pathway	4
BMPR2	ATP-binding; metal-binding	BMP pathway, brain development	1
ADCY8	membrane-bound	Ca2+-stimulable adenylyl cyclase	2
GABBR1	receptor activity	synaptic transmission	2
ARX	cromatin binding	axon guiance	2
Plexin	semaphorin receptor	axon guiance	1
NFASC	cell adhesion, ankyrin-binding	axonal guidance, neurite extension	1
BAI3	GTPase activator	dendrite morphogenesis, synapse assembly	1
CENTB2	GTPase activator	cellular response to nerve growth factor stimulus	1
Cellullar stress			
msrA	oxidoreductase	protein repair; response to oxidative stress	2
EIF2B5	translation iniciation factor	ER stress, astrocite diferenciation	1
ANKS4B	ankyrin repeat	response to ER stress	1
IL8	Cytokine	ER stress,calcium singalling,	1
Ubiquitin-proteasome			
GABARAP	beta-tubulin binding; Ubiquitin protein ligase binding	synapatic transmission, mitophagy, extrinsec apoptosis	13
ARRDC3	beta-3 adrenergic receptor binding	regulator of ubiquitin-protein transferase activity	2
SUMO4	ubiquitin-like protein	protein sumoylation	1
ASB11	ankyrin repeat	protein ubiquitination	1

Table D4. Summary main GDAP1 partners. Two hybrid data from Pla-Martín 2012.

The idea is that GDAP1 interacts with wide range of proteins in a similar way to MIRO.

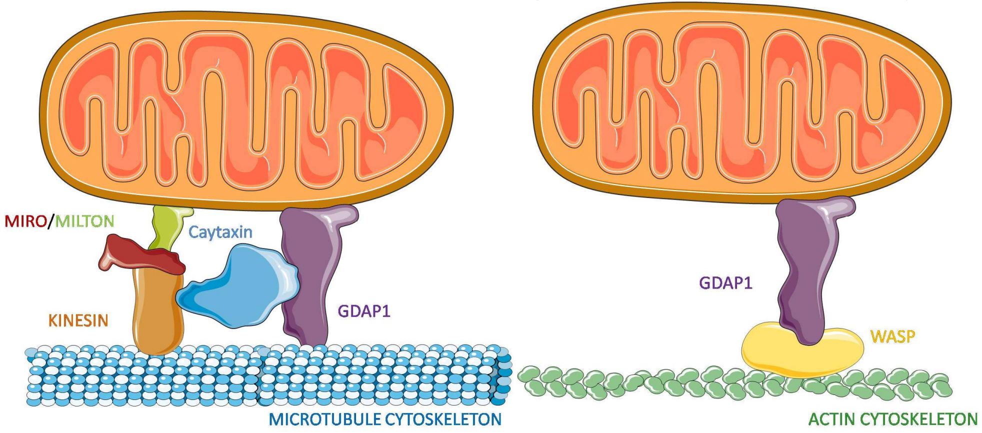

Figure D1. GDAP1 interacting proteins in relation with mitochondrial transport. Representative pictures of GDAP1 and its interacting proteins which are related with mitochondrial transport through microtubule and actin cytoskeleton (drawn from www.servier.com).

As GDAP1 interact with microtubule transport proteins as well as with SUMO4 and EIF2B5, among others ones, lack of GDAP1 affects to several processes in mice (figure D2).

Absence of GDAP1 causes in some way that SUMO4 does not activate DRP1 (Ong et al. 2015). As a consequence fission is blocked producing elongated mitochondria.

In addition, as GDAP1 cannot bind to EIF2B5, EIF2 has a not properly conformation and cannot block Bcl-xL by CHOP (Iurlaro & Muñoz Pinedo 2015). Bcl-xL blocks DRP1 (Saez-Atienzar et al. 2016) and as a consequence fission is blocked again. Bcl-xL also blocks tubulin acetylation (Saez-Atienzar et al. 2016) and, as a consequence, mitochondrial movement is impaired.

Finally, as GDAP1 also interact with Caytaxin, Gdap1 null mice have slower anterograde mitochondria in motion.

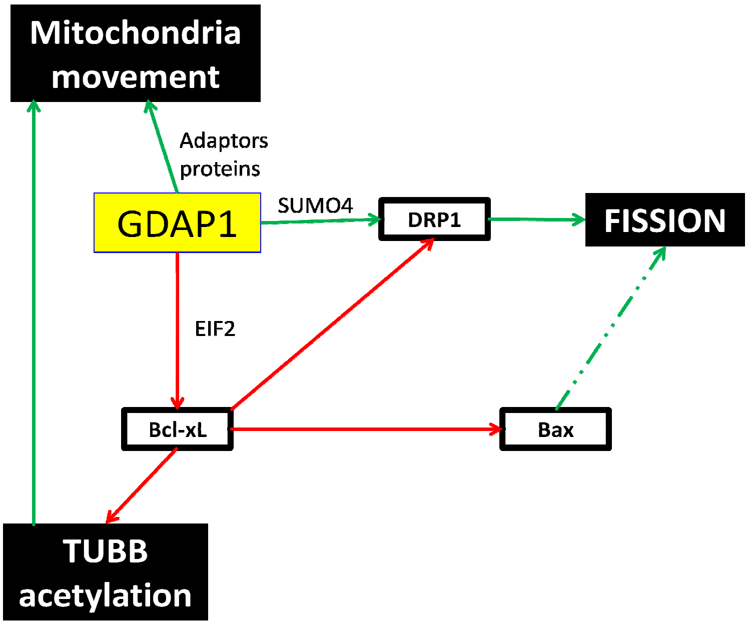

Figure D2. Workflow of *GDAP1* involved processes. Activation or facilitation is represented as green arrows. Red arrows showed inactivation or blocking action**.**

As a consequence of slower anterograde velocity, distal axons denervate at NMJ level. Slower velocity also causes no correct position of mitochondria near to ER, so ER stress proteins that interact with GDAP1 cannot interact.

Longer mitochondria in retrograde direction are caused by DRP1 impairment to fission defective mitochondria, as well as, ubiquitin binding proteins cannot interact with GDAP1**.**

Conclusions

1º: Murine *Gdap1* is expressed in central nerve system as well as in peripheral nerve system. Non neuronal tissues do not express GDAP1.

2º: Other member of Gdap1 family, GDAP1L1, is also expressed in mice neuronal tissues, mainly in central nervous system.

3º: Eliminating exon 1 of *Gdap1* in mice is enough to generate a mouse model for *GDAP1* related Charcot-Marie-Tooth (CMT). Mice lacking *Gdap1* ubiquitously are viable and fertile. As a model, *Gdap1*$^{-/-}$ mice mimics the principal hallmarks of the disease: "pes cavus", motor defects, decreased motor nerve conduction velocity and alterations in compound muscle action potential.

4º: Use of this mouse model allowed us to determinate *GDAP1* related CMT as an axonal neuropathy rather than demyelinating.

5º: The sciatic nerve, which has motor and sensory axons, is altered in 5 months old *Gdap1*$^{-/-}$ mice. Loss of fibre density as well as a switch in axon size has been detected. Demyelinating signs have not been observed.

6º: In the muscle, loss of *Gdap1* produces a dennervating process. Neuromuscular junctions are not fully occupied by nerve ends in 12 months old mice. In addition, we have detected abnormal structures in this axon terminals. Neuromuscular plates from 5 months old mice are indistinguishable between control and null animals.

7º: In the ventral horn of the spinal cord, lack of *Gdap1* produces a progressive loss of healthy motor neurons. Signs of damage have been also found in protein lysates form the whole spinal cord.

8º: In the dorsal root ganglia, the absence of GDAP1 seems to does not alter sensory neurons at least at histological level until 12 months old.

9º: Adult dorsal root ganglia cultures are compromised by the lack of GDAP1. Smaller soma and shorter neurites has been observed in sensory neurons from *Gdap1*$^{-/-}$ mice. Microtubule cytoskeleton destabilization may explain this defects.

10º: Mitochondrial transport and dynamics are the main processes disrupted by the loss of GDAP1. CMT affected tissues from *Gdap1*$^{-/-}$ mice, as dorsal root ganglia and sciatic nerve, have longer retrograde moving mitochondria. In addition, anterograde speed was reduced on this tissues. Non affected tissues, as superior cervical ganglia, presented shorter retrograde moving mitochondria and reduced retrograde speed.

11º: *GDAP1* missense mutations harboured in CMT patients have different effects on mitochondrial transport in cultured sensory neurons. These wide variety of effects can be correlated with the wide range of phenotypes presented in patients.

Materials & Methods

Genetic characterization experiments

Generation of *Gdap1*$^{-/-}$mice.

*Gdap1*heterozigous knock-out mouse model was created by genOway (Lyon, France). With this propose, targeting vector containing two loxP sites flanking the first of six exons of *Gdap1*gene, a neomycin positive selection cassette, and a diphtheria toxin A (DTA)negative selection was used. This loxP-exon 1 Gdap1-FRT-PGK-Neo^{R}-FRT-loxP cassette was introduced into the mouse genome by homologous recombination in 129Sv embryonic stem (ES) cells. The targeting vector was integrated into the ES cell genome and the neomycin cassette located between exons 1 and 2 of the *Gdap1*gene allowed for selection of ES cells that had successfully integrated the vector by the appropriate homologous recombination. The negative selection DTA cassette located outside the region of homology to the gene ensured that the ES cells in which random integration died. The DNA from the targeted ES cells was then analysed by Southern blot analysis.
Correctly targeted ES cells were microinjected into C57BL/6J blastocysts and transferred to the pseudopregnant CD1 females. Pregnant mice were carrying pups to term and born chimaeras were identified by agouti coat colour contribution (characteristic of 129Sv mice). For the germ-line transmission, chimera mice were crossed with C57Bl/6J mice to obtain F1 mice carrying the recombined allele containing the floxed*Gdap1* allele and Neo selection cassette. These mice were mated with Flp recombinase-expressing C57Bl/6J Flp mice to remove the Neo resistance cassette and generate a line of Neo-excised floxed mice.

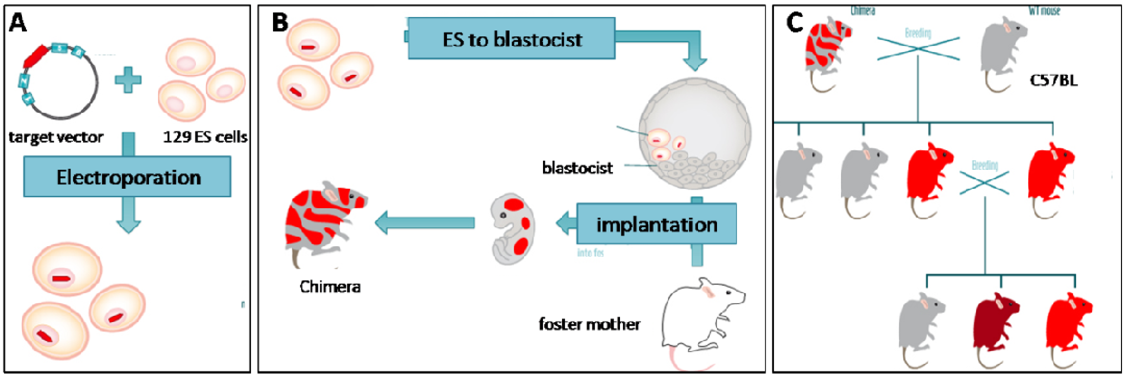

Figure M1. null mice generation with genOway technology. A)Target vector is electroporated into mice ES cells where homologous recombination takes place. B) Correctly targeted ES cells are injected into a blastocyst which is transferred into a pseudopregnant foster mother and chimeras get born. C)To germ-line transmission chimera are crossed with C57BL mice and successfully some offspring will be heretrozogous for DNA change. Crossing heterozygous mice, the three possible genotypes are obtained.

Chimera heterozygous offspring (*Gdap1*$^{+/floxed}$) were confirmed by Southern blot analysis and tested by PCR for the presence of the targeted allele. Cre-mediated excision was performed in vivo by cross-breeding mice harbouring a cytomegalovirus promoter (CMV) driven Cre transgene resulting in the genomic deletion of Gdap1 exon 1 from the floxed allele during the early stages of embryonic development. The heterozygous Gdap1-deficient founder mice (*Gdap1*$^{+/-}$) were further crossed to obtain *Gdap1*$^{+/+}$, *Gdap1*$^{+/-}$ and *Gdap1*$^{-/-}$ mice.

All the breeding from heterozygous Gdap1-deficient founder mice were done in Instituto de Biomedicina de Valencia (IBV) with the approval of Bioethics Committee of the Consejo Superior de Investigaciones Científicas (CSIC) and carried out in accordance with the Real Decreto 1201/2005. All mice were maintained at 21 ± 2°C on a 12 h light/dark cycle with food and water *ad libitum*.

Genotyping.

Mice genotyping was performed on tail tip DNA extracted with Maxwell® 16 mouse Tail DNA purification kit (Promega) in a Maxwell® 16 Magnetic Particle Processor (MX3031. Promega) according to the manufacturer's instructions.

Polymerase chain reaction (PCR) was performed using Expand High Fidelity PCR System (Roche) a two different approaches were designed. Primers with melting temperatures are shown in table M1.

PCR strategy 1 allowed to distinguish floxed*Gdap1* (with loxP sequences around deleting sequence), endogenous gene (without loxP sequences) and deleted gene (*Gdap1*$^{-/-}$). Endogenous gene amplified a product of 379pb, floxed*Gdap1* a 490pb product and deleted gene produced no amplification.

PCR strategy 2 allowed to distinguish*Gdap1*$^{+/+}$ and*Gdap1*$^{+/-}$when presence of endogenous *Gdap1* in detected previously. Wild type gene amplified single product of 2700pb and exon 1 deleted gene amplified a 600pb product. So *Gdap1*$^{+/+}$mice presented one longer band (2500pb), *Gdap1*$^{-/-}$animals a shorter one (550pb) and *Gdap1*$^{+/-}$mice both of them (2500 and 550pb).

RT-PCR for *Gdap1* and *Gdap1L1* expression.

Gdap1 and *Gdap1L1* expression was studied using reverse transcriptase polymerase chain reaction (RT-PCR). RNA from tissues was extracted using TRI Reagent (Sigma) according to the manufacturer's instructions. One microgram of RNA was treated with Dnase I (Sigma) to eliminate DNA contaminations and transformed into cDNA using M-MLV reverse transcriptase enzyme (Sigma) and random hexamer primers. With this product a normal PCR with Taq polymerase (Netzyme, Fermentas) was performed to study *Gdap1*and *Gdap1L1* expression. *Gapdh* was used as a housekeeping gene. Primers with melting temperatures are shown in table M1.

All PCR's products obtained after 35 cycles were load in an agarose gel and stained with ethidium bromide in order to detect DNA bands.

Gene	**direction**	**sequence**	**Tm**
Gdap1 mice genotyping			
PCR1	Forward	5'-TCATGCGAAATGGCTCGGAGG-3'	65ºC
	Reverse	5'-GGAACCCCTTCTCTCACTTTCCAGG-3 '	
PCR2	Forward	5'-CCTTGTTTCTCATCTACTCCTATTATCCGTAGG-3'	67ºC
	Reverse	5'-GGAACCCCTTCTCTCACTTTCCAGG-3 '	
Reverse Transcription			
Gdap1	Forward	5'- ATGCGCTTGAACTCAGCTGG -3'	58ºC
	Reverse	5'- GCCAGTGTAAAGGATTCTCC -3'	
Gdap1L1	Forward	5'-ATGCGGCTCAACCTGGGTGAGG-3'	68ºC
	Reverse	5'-GGCAAAGCGTCTCTGGACCCTC-3'	
Gapdh	Forward	5'-ATGGTGAAGGTCGGTGG AAC-3'	60ºC
	Reverse	5'-GCGGAGATGATGACCCTTTTGG-3'	

Table M1. Primers used in *Gdap1* null mice genetic characterization. Primers sequences and melting conditions are shown for *Gdap1* genotyping by PCR and for *Gdap1* and *Gdap1L1* expression by RT.

Real Time PCR for mitochondrial DNA copy number.

This work was done in Genomics and Translational Genetics service of Centro de Investigación Principe Felipe (CIPF) in collaboration with Laura Ramírez.

Briefly, mitochondrial DNA copy number analysis by 16S gene and genomic DNA of a nuclear housekeeping gene ANG1 (Assay Applied Biosystems: Mm00833184_s1) were quantified using the same amount of DNA input (Perier et al. 2013).

Western blotting.

Tissues were snap frozen on dry ice and homogenized in lysis buffer (50mM TrisHCl pH 7.4, 1.5mM $MgCl_2$, 5mM EDTA, 1% Triton X-100, 50mM NaF, 1mM Na_2VO_3) containing protease inhibitors (Roche). Tissue lysates were quantified by Bradford reaction (Bio-Rad) and 50µg were use to the westerns blots. When it was necessary Amicon® Ultra-0.5 Centrifugal Filter Devices (Millipore) were use in order to concentrate lysates, mainly for sciatic nerve extracts.

Denatured protein extracts were resolved sodium docecylsulfate polyacrylamide gels (SDS-PAGE) in a Mini-PROTEAN® Electrophoresis System(Bio-Rad).

After electrophoresis, proteins were transferred onto a PVDF membrane (BioTrace PVDF, Pall Corporation) using Mini Trans-Blot® Cell (Bio-Rad) in a transfer buffer consisting in 25mM Tris, 192mM Glycine and 20% methanol at 4ºC.

After transferring, membranes were stained with Ponceau Red (Ponceau S 0,1%, 5% acetic acid) to visualize transference.

Subsequent to several washes in water and one hour on blocking solution (5% dry milk in T-TBS) incubation at room temperature, primary antibodies were also added.

Latter than several washes in T-TBS (20mM TrisHCl pH 7,5; 150mM NaCl and 0,1% Tween-20, a final incubation with the appropriate secondary antibodies was done. Finally, protein bands were detected using a Fujifilm Las-3000 after incubation with the ECL Plus Western Blotting Detection System (GE Healthcare).

The following antibodies were used to study GDAP1 expression in mouse tissues: actin (Sigma); β-tubulin (Invitrogen), ATP synthase (Invitrogen), GDAP1 (Abnova) and GDAP1 (Sigma). To study spinal cord damage catalase (Sigma) for oxidation; and Bax (Santa Cruz) andBcl2 (Cell Signalling) for apoptosis were used in combination with actin (Sigma) as load charge control. All antibodies references and dilutions are shown in table M2

Density of the bands was quantified by Multi Gauge V2.1 software using. Normalization using actin band quantification was done for each protein quantification. At list 3mice per condition were used to calculate the mean value and do comparisons between wild type and *Gdap1*$^{-/-}$mice.

name	**comercial**	**reference**	**dilution**
GDAP1	Abnova	H00054332-A01	1/1000
GDAP1	Sigma	HPA014266	1/1000
ATPsynthase	Invitrogen	459240	1/500
Actin	Sigma	A2066	1/4000
β-tubulin	Invitrogen	32-2600	1/500
catalase	Sigma	C0979	1/500
Bax	Santa Cruz	N-20 sc-493	1/500
Bcl2	Cell Signaling	50E3	1/1000

Table M2. Antibodies used in western blotting experiments. References and dilutions are shown.

Phenotypic characterization experiments

Rota-rod test.

Motor performance and balance were tested using an accelerating rotarod (UGO Basile Accelerating Rotarod). Each mouse underwent for 4 days the same procedure. The first 2 days were used to train the mice (five sessions of 1 min each, walking at 4 r.p.m.). The test sessions were run on day 3 and 4. Each test day, 2 series of 3 trials with a 2 hours rest period between the 2 series and a 15 min rest period between consecutive trials was performed. During the test the speed of the rotarod was accelerated from 4 to 40 r.p.m. over a 5 min period. A different group of animals was used for each time point of the study. At list 35 mice were use for each experiment.

Two small group of littermates (6 null mice and 3 controls) passed the test monthly in order to better characterize the heterogeneity and the progression of the disease. This rota-rod test was named follow-up.

Time to animal fall each trial was measured. Average by animal (or animal each time point in follow up experiments) was calculated for genotype comparisons.

Balance beam test.

The beam apparatus consists of 1 meter beams with a flat surface or round surface of 12 mm or 5 mm width resting 50 cm above the table top on two poles. A black box is placed at the end of the beam as the finish point. Nesting material from home cages is placed in the black box to attract the mouse to the finish point. The time to cross 80 cm is measured

On training days, each mouse has to cross the flat beam 3 times, then 12 mm beam 3 times and then the 5 mm beam 3 times. On the test day, times to cross each beam are recorded. Two successful trials in which the mouse did not stall on the beam are averaged (Luong et al. 2011).

Mean by animal (n=5) was calculated for genotype comparisons.

Pole test.

For performing this test the mouse is placed on a vertical wooden pole with its head facing upwards. A normal mouse will grip the pole before turning through 180° and slowly climbing down to the base of the pole, latencies to turn to descend once turned and to complete the task are primary measured (Brooks & Dunnett 2009).

Mean by animal (n=5) was calculated for genotype comparisons.

Gait and footprint analysis.

Footprint analysis was modified from that described for rats by De Medinaceli et al. (1982). This test allows assessing limb coordination and body weight support (rotation, stride length, base of support. Mice crossed an illuminated alley, 70 cm length, 9 cm width, and 6 cm height, before entering a dark box at the end. Their hindpaws were coated with nontoxic water-soluble ink and the alley floor was covered with sheets of white paper. To obtain clearly visible footprints, at least 3 trials were conducted (Wiethölter et al. 1990; Klapdor et al. 1997). The footprints were then scanned and analysed with ImageJ software version 1.48a (Rasband, W.S., ImageJ, U. S. National Institutes of Health, Bethesda, Maryland, USA, http://imagej.nih.gov/ij/, 1997-2015).

For the morphometric gait analysis the following parameters were measured in centimetres or degrees:

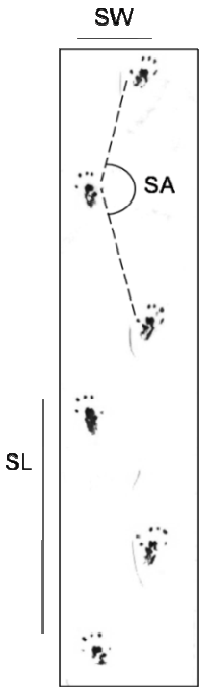

Stride Length (SL): The line connecting the footpads of each side were drawn, yielding the stride trajectory (Wiethölter et al. 1990). Stride Length was measured as distance between the third toe from one print and the same position in the next step of the same paw.
Stride Angle (SA). The line connecting the first toe of opposite paws in one step side were drawn, yielding the stride trajectory. The Stride Angle was the angle formed in between two consecutive connecting lines.
Stride Width (SW). The lines connecting the footpads of each side were drawn, yielding the stride trajectory (Wiethölter et al. 1990). The perpendicular distance of the opposite footpad to that line is the Stride Width.

Figure M2. Representative scanned walking track from a Wild type 12 months old mice. Only hind paws are displayed. Gait print parameters are shown: Stride Length (SL), Stride Angle (SA) and Stride Width (SW).

For the morphometric footprint analysis the following parameters were measured in centimetres:
*Plantar or Print length (PL).*This is the distance between the print of the third toe and the most proximal part of the foot visible on the paper (cuneiform or cuboid bone) (Wiethölter et al. 1990).
*Toe spreading (TS).*This is the distance between the prints of the first and the fifth toe (Wiethölter et al. 1990).
Intermediate Toes (TS). This is the distance between the prints of the second and the forth toe (Klapdor et al. 1997).

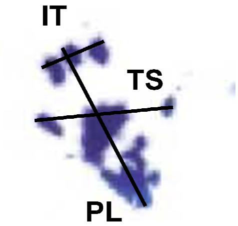

Figure M3. Representative footprint from a WT 12 months old mice. Only left hind paw is displayed. Footprint parameters are shown: Plantar Length (PL), Toe Spreading (TS) and Intermediate Toes (IT).

The average from four (two from left and two from right paw, for the footprint) or six measurements (three for each side step, for gait print) were obtain for each animal. Average were calculated for each group of 5 mice to do comparisons.

Histological procedures

Tissue fixation and sections obtaining.

Mice were sacrificed by gentle cervical dislocation. Distal big muscles (Soleus& Gastrocnemius and Quadriceps), lumbar spinal cord and DRG were dissected and immediately fixed in 4% paraformaldehyde (PFA) in PBS. For muscles and lumbar spinal cord, fixation on PFA was done over night at room temperature, for DRG only 20min were necessary.

After fixation, a 70% ethanol step was added prior to mount tissues in cassettes and introducing them in the tissue processor (Spin Tissue Processor STP 12, Myr) where tissues were included in paraffin. Tissue processor protocol was: 1h in 70% ethanol, 3h in 96% ethanol, 90 min in a new container with 96% ethanol, 2 h in 100% ethanol, 6 h more in a new 100% ethanol, 90 min in xylene, 150 min in xylene again, 150 min in liquid paraffin (60ºC) and 2 h more in new paraffin.

Afterwards, tissues were embedded in paraffin blocks (Modular Tissue Embedding Center 350, Myr).

Microtome (Rotary microtome HM 340 E, Microm) was used to slice paraffin blocks in 10µm-thick sections for muscles and spinal cord, and 4µm-thick sections for DRGs. Slices were collected from a 40ºC water bath and mounted in a microscope slide.

Haematoxylin&Eosin and Nissl staining.

Haematoxylin has a deep blue-purple colour and stains nucleic acids by a complex, incompletely understood reaction. Eosin is pink and stains proteins non specifically. In a typical tissue, nuclei are stained blue, whereas the cytoplasm and extracellular matrix have varying degrees of pink staining (Fischer et al. 2008).

The Nissl-staining method is based on the interaction of basic dyes such as cresyl violet, with the nucleic acid content of cells. These dye can bind to the DNA content of the cell nuclei, but also to the RNA that is highly concentrated in rough endoplasmic reticulum and ribosomes (Nissl substance) in the cytoplasm. Since neurons are very active protein synthesizing cells, the cytoplasm of these cells contain high concentration of rough endoplasmic reticulum. Nissl staining can specifically stain the cytoplasm of neurons without recognizing the perikarya of other cellular elements in the brain (Kádar et al. 2009).

Microscope slides containing paraffin sections were placed in a slide metal holder. For deparaffinise slices, holder was kept at 64ºC for 1h, 10min in xylene and 10min more in a new xylene container.

For rehydrate sections several steps of percentage descending ethanol were done (100%, 100%, 96%, 70% and 50%) to finally keep them 2min in distilled water.

For haematoxylin staining, slices were immersed in Harris haematoxylin for 10min and then rinsed under tap water for 5min.

For eosin staining, slices were immersed in eosin for 30s and fixed in re-used 96% ethanol for 1min.

A last dehydrating step was done passing sections through an increasing ethanol percentage container (50%, 70%, 96%, 100%, 100%). Finally, holder was kept in xylene for 10min (2 times).

For Nissl staining, same protocol that for Haematoxylin& Eosin was used only changing the staining part. This time slices were immersed in 1% w/v Cresyl Violet (Sigma) plus 1% v/v Glacial Acetic Acid for 2min and then rinsed under tap water for 5min.

Slides were dry and mounted with DPX mounting medium and observed under research microscope (Leica DMRXA2 microscope plus Leica DFC300FX colour camera).

MN counting in Spinal cord.

The lumbar region of the spinal cord (L1–L5) was processed for paraffin embedding. 300 serial cross sections (10µm thickness) of the lumbar spinal cords were made (3000µm or 3mm total length), among which every fifth section (50 sections examined per animal) was processed and Nissl stained.

The anterior horn (either left of right) of stained sections were analysed microscopically (Leica DMRXA2 microscope, Leica DFC300FX colour camera, 40x 0.75NA)
All cells were counted within the ventral horn below an arbitrary horizontal line drawn from the central canal. Morphological criteria were also employed, so that only large polygonal neurons in which the nucleolus was clearly visible at high magnification were included in the counts.
At list 3 mice per condition were used to calculate the mean and do comparisons between wild type and *Gdap1*$^{-/-}$ mice.

Neuromuscular Junctions occupancy in distal large muscles

Muscle election.

First of all, it's important to remark that when analyzing neuromuscular junction (NMJ) morphology, muscle choice is of great importance. Some of the primary considerations might include muscle fibre type, body position, and comparative analysis to human conditions.

We selected gastrocnemius because is a *Delayed Synapsing* (DeSyn) muscles. In a DeSyn muscle, focal AChR clustering and maintenance depends critically on nerve-derived factors, whereas this dependence is much more limited in *Fast Synapsing* (FaSyn) muscles (Pun et al. 2002).

Often, however, muscle choice is influenced by ease of dissection. Consequently, NMJ analysis is often performed exclusively on large appendicular muscles such as Gastrocnemius. To obtain good NMJ staining in such muscles, sectioning or mechanical disruption of muscle fibres is often required. As a result, the innervation pattern may become disrupted and a comprehensive and high quality analysis of innervation patterns, sprouting and dennervation is often compromised (Murray et al. 2014). When using such muscles a technical expertise is required to dissect them without damage.

NMJ's labelling in the whole muscle.

Gastrocnemius (containing also soleus) dissection was done after mice were sacrificed by cervical dislocation. The muscle was carefully cut apart and immediately covered with 4% paraformaldehyde (PFA) for an incubation of 20 minutes at room temperature.

After washing three times in PBS for 10 minutes, acetylcholine receptor from the postsynaptic part of the neuromuscular junction was stained with α-Bungarotoxin-tetrametylrhodamine (Sigma) in PBS for 20 minutes at room temperature.

Subsequently, the muscles were washed again (three times in PBS for 10 minutes) and penetrated with ice-cold methanol for 5 minutes at −20 °C.

After a new washing, a blocking solution containing 2% bovine serum albumin (BSA, Sigma), 0.2% Triton X-100 and 0.1% Sodium Azide was applied for 1 hour at room temperature.

Spent this time, the presynaptic part of neuromuscular junction was label with a rabbit polyclonal antibody against III-β tubulin (Sigma); the antibody was applied in blocking solution over night at room temperature. All antibodies references and dilutions are shown in table M3.

After washed over again, a secondary Alexa 488-conjugated polyclonal antibody (1:100, Invitrogen) was diluted in the blocking solution and applied for 5 h at room temperature. Prior chopping the muscles, a last washing step was done.

Finally, the whole gastrocnemius was manipulate under the dissection microscope to chop it in a sagital plane. Slices were cut manually with a scalpel and mounted with a Fluoromont-G Solution (SouthernBiotech) on a microscope slide. It's important to remark that all the process was done in a rotatory shaker at room temperature apart from postfixation step with methanol that was done statically at -20ºC.

name	**comercial**	**reference**	**dilution**
BTX	Sigma	T0195	10µg/ml
β-tubulin III	Sigma	T 2200	1/500

Table M3. Antibodies used in Neuromuscular Junction labelling. References and dilutions are shown.

NMJ's imaging and quantification.

The whole gastrocnemius (with the soleus) was divided in 10 pieces that were analysed with a Leica True Confocal Scanning SP8 imaging system (DMI6000 microscope, 40x 1.3NA apochromat oil immersion objective).

Scoring of endplate occupancy was done at low power (40× objectives) magnification by digital stitching of contiguous z-series (each 0.5µm) obtained using the confocal microscope. An endplate was scored as occupied if there was evidence of contact by an overlying III-β-Tubulin nerve terminal with the α-Bungarotoxin-tetrametylrhodamine AChRs stained motor endplate area. If the AChR cluster was not fully filled by the presynaptic axon the endplate was scored as not occupied (Wong et al. 2009). All NMJ counted were positive to neuronal and muscle markers in order to avoid aneural AChR clusters (Wu et al. 2010).

Data analysis for NMJ occupancy.

For the morphological analysis of the neuromuscular endplates three control and three *Gdap1* $^{-/-}$ mice for each age were studied. More than 100 NMJ were studied for each group.

Experiments were done in parallel with WT and KO samples to reduce variability between experiments. Occupied NMJ percentage of total counted number was calculated for each animal, mean was obtained for each genotype and age (n=3) (Krieger et al. 2013).

Electrophysiology

Gdap1$^{-/-}$ and wild type mice of 2 and 5 months old (n≥4) were send from Valencia to Lausanne where motor nerve conduction studies were done in collaboration with Dr Roman Chrast from Department of Medical Genetics, University of Lausanne, Lausanne, Switzerland. Special thanks to Dr. Jennifer Zenker for performing and helping to analyse the electrophysiological experiments.

Briefly (adapted from Mallik & Weir 2005; Katirji et al. 2013), motor studies are performed by electrical stimulation of a nerve and recording the compound muscle action potential (CMAP) from surface electrodes overlying a muscle supplied by that nerve. The recording electrodes are performed using adhesive conductive pads placed onto the skin overlying the target muscle. The active electrode is placed over the muscle belly and the reference over an electrically inactive site (usually the muscle tendon). A ground electrode is also placed somewhere between the stimulating and recording electrodes providing a zero voltage reference point. The sciatic nerve motor study might involve stimulation at the ankle and the hip (figure M4).

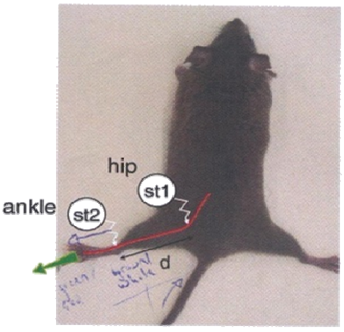

Figure M4. Representative image of motor nerve conduction study in mice. Proximal (st1, hip) and distal stimulation (st2, ankle) are represented.

The CMAP is a summated voltage response from the individual muscle fibre action potentials (figure M5). In the CAMP response we can measure several parameters: amplitude, area, duration and latency.

The CMAP *amplitude* is measured from baseline to negative peak (the neurophysiological convention is that negative voltage is demonstrated by an upward deflection) and measured in millivolts (mV). CMAP amplitude reflects the number and size of muscle fibres that ultimately fire.

The CMAP *area* is conventionally measured between the baseline and negative peak. CMAP also reflects the number of muscle fibres in the CMAP. CMAP area is measured in mv/ms. Differences between distal and proximal stimulation sites assume special significance in the determination of conduction block from a demyelinating lesion.

The CMAP *duration* is usually measured from the initial deflection to terminal deflection back to baseline (total duration). CMAP duration is a measure of synchrony (i.e., the extent to which each of the individual muscle fibres fire at the same time). Duration measurements are usually in milliseconds (ms).

The *latency* of the CMAP is the time from stimulus to the initial CAMP deflection from baseline. It is the time from stimulus artefact to onset of the response and is a biphasic response with an initial upward deflection followed by a smaller downward deflection. Latency includes three separate times: (1) nerve conduction time from the stimulus site to the NMJ, (2) the time delay across the NMJ and (3) the depolarization time across the muscle fibres. Latency measurements are usually in milliseconds (ms).

In the normal state stimulating the sciatic nerve at the ankle and the hip results in two CMAPs of similar shape and amplitude (figure M5) because the same motor axons innervate the muscle fibres making up the response. However, the latency will be greater for hip (proximal) stimulation compared with ankle (distal) stimulation because of the longer distance between the stimulating and recording electrodes.

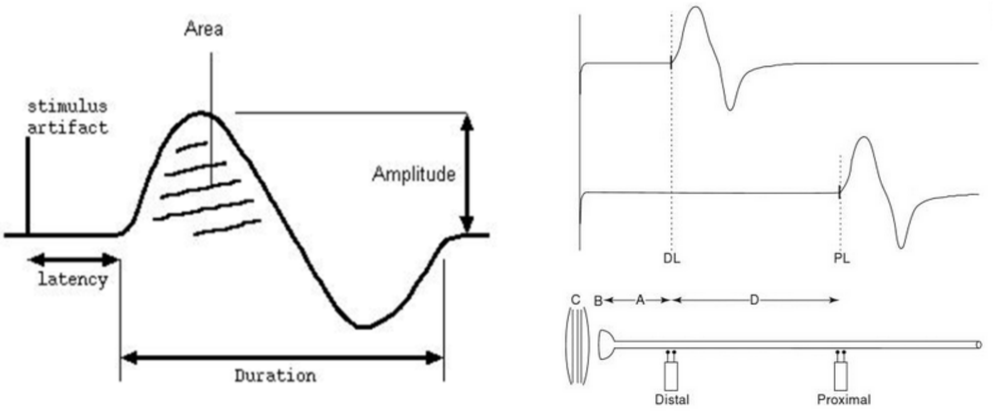

Figure M5. Representative CMAP response. Left image shows detailed all the CMAP parameters: amplitude, area, duration and latency. Right image shows CMAP response to distal and proximal stimulus (DL: distal latency; PL: proximal latency). Lower right image shows a motor axon connecting with the muscle fibre; distal and proximal stimulation sites are represented (A: the nerve conduction time from the distal stimulation site to NMJ; B: the NMJ transmission time; C: the muscle depolarization time; D: the nerve conduction time between proximal and distal stimulation sites). If distal latency (A+B+C) is subtracted from proximal latency (A+B+C+D), only the nerve conduction time between the distal and proximal stimulation sites (D) remains. Measuring the distance between these two sites we are able to calculate MNCV: distance (mm)/D(ms).

Motor Conduction Velocity is a measure of the speed of the fastest conducting motor axons, which is calculated by dividing the distance travelled by the nerve conduction time. However, motor conduction velocity cannot be calculated by performing a single stimulation. Motor latencies include nerve conduction time, NMJ transmission and muscle depolarization time. Thus, to calculate a motor conduction velocity, without including NMJ transmission and muscle depolarization times, two stimulation sites must be used: one distal and one proximal. When the distal latency is subtracted from the proximal latency, then only the nerve conduction time between the proximal and the distal stimulations remains. The distance between these two sites can then be approximated by measuring the surface distance in millimetres. Thus, conduction velocity is usually measured in meters per second (m/s):

$$\text{MNCV (m/s)} = \frac{\text{distance between distal and proximal stimulation site}}{\text{proximal latency} - \text{distal latency}}$$

Morphometric analysis of Sciatic nerve

Sciatic nerve dissection, fixation and imaging.

Same animals of 5 month old that were use to analysed nerve conduction velocity were use to study sciatic nerve ultrastructure (n=4). Dissection and fixation of sciatic nerves were done in collaboration with the laboratory of Dr. Roman Chrast (University of Lausanne). Dra. Jennifer Zenker was helping us directly by receiving and taking care of animals.

Quickly, sciatic nerves were dissected and fixed by immersion in 2,5% glutaraldehyde for 2 h at 4°C, washed in 0.1 M cacodylate buffer (pH 7.3), and osmicated for 4 h in 1% OsO_4 (Fluka). Nerves were rinsed in water, dehydrated, and embedded in Epon 812 resin (Fluka). Half-micrometer sections were stained with 1% toluidine blue and examined by light microscopy.

For electron microscopy analysis, ultrathin sections and imaging were done in collaboration with Instituto Valenciano de Patología, particularly with the laboratory of Dr. Jerónimo Forteza. Mario Soriano (biologist and technician) was helping us directly.

Briefly, sciatic nerves were post fixed with 2 % osmium and 2 % uranyl acetate, rinsed, dehydrated and embedded in epoxi resin (Durcupan). Then, resin embedded sciatic nerves were cut, collected on coated single slot grids, and stained with lead citrate. Finally, photomicrographs were obtained under a transmission electron microscope FEI Tecnai G2 Spirit (FEI Europe) using a digital camera Morada (Olympus Soft Image Solutions GmbH).

Number of mitochondria, myelinated fibre density and size.

To morphometric analysis, 10 non-overlapping images were photographed at 2,550 magnification for each sciatic nerve slice. The analysis was performed with ImageJ software version 1.48a (Rasband, W.S., ImageJ, U. S. National Institutes of Health, USA, http://imagej.nih.gov/ij/, 1997-2015). Images were binarized and all myelinated axons were count. Data from 4 mice (around 1200 axons) were counted for each condition. "Analyse Particle" tool was use to measure all axons and "Cell Counter" plugin was use to count all mitochondria inside axons.

g-ratio.

Rushton (1951) was the first to present the relationship between axonal diameter and the thickness of its myelin sheath as a g-ratio (g-ratio = axonal diameter/outer diameter of the whole nerve fibre) (Ugrenović et al. 2015; Paus & Toro 2009).

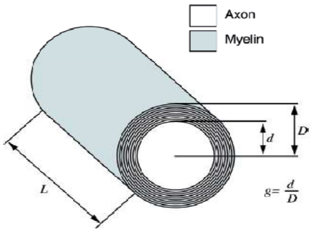

Figure M6. g-ratio representation. Drawing of g-ratio calculation in myelinated axons.

To analyse g-ratio, same images than previous experiment were used. *g-ratio* was obtained using "g-ratio" plugin from ImageJ (version 1.48a, National Institutes of Health, USA, http://imagej.nih.gov/ij/, 1997-2015) by manually tracing myelin and axons on micrographs. Computed values from 3 mice (450 randomly selected myelinated axons) were counted for each condition.

Adult Dorsal Root Ganglia (DRG) cultures experiments

Animals for adult DRG cultures.

All these experiments were done in Instituto de Biomedicina de Valencia (IBV) with the approval of Bioethics Committee of the Consejo Superior de Investigaciones Científicas (CSIC) and carried out in accordance with the Real Decreto 1201/2005.

Adult DRG cultures.

Adult mice aged 5-7 months were humanely killed by cervical dislocation. DRGs were dissected and kept in L15 medium (Gibco) over night.

Dissected DRGs were washed in F12-medium (Gibco) prior to starting the dissociation protocol. Washed DRGs were incubated with 0.2% collagenase type I for 30 min at 4°C and for 1 h at 37°C. Next incubation was done in 0.05% trypsin (Gibco) for 30 min at 37°C. Finally, 1% DNase (Sigma) was add for 5 min at RT.

After a last wash in F-12 medium, DRGs were diluted in F-12 medium supplemented with 2 mM glutamine (Gibco), 62.5 ng/ml progesterone (Sigma), 16 μg/ml putrescine (Sigma), 400 ng/ml L-thyroxine (Sigma), 337 ng/ml triiodothyronine (Sigma), 38 ng/ml sodium selenite (Sigma), 0.35% Albumax II (Gibco), 0.6% antibiotic-antimycotic (mixture of penicillin, streptomycin and amphotericin B from Gibco). DRGs were then gently dissociated using a Sigmacote (Sigma) treated Pasteur pipette.

Finally, dissociated DRG were plated on a precoated 13mm glass coverslips. Coating state was done incubating coverslips with 0.05% poly-DL-ornitine (Sigma) overnight at room temperature followed by washing and incubation with 20 μg/ml laminin (Sigma) for at list 4 hours at 37ºC. Adult DRG cultures were maintained at 37°C in a humidified incubator under 5% CO_2 at a density of 2000 cells per plate.

A mixture of neurotrophins (NT3, βNGF and BDNF all from Peprotech, at 10ng/ml each one) were added to the medium at 2 and 5 div in order to favour the neuronal growth (Valdés-Sánchez et al. 2010).

Immunostaining of DRG cultures for characterization.

For neuronal gross morphology and mitochondria characterization, 5 div DRG cultures were fixed with 4% paraformaldehyde in PBS for 20 min. After 3 rinses in PBS, permeabilization and blocking was done by incubating with 3% horse serum and 0.2% Triton X-100 in PBS for 30 min at room temperature.

Neuronal cells were stained using monoclonal rabbit anti-β-tubulin III (Sigma) for discriminate neurons and monoclonal mouse anti-Cytochrome c (Invitrogen) to mitochondria labelling. After 4ºC overnight staining in blocking solution and several washes in PBS, neurons were incubated for 1 h at room temperature, with fluorochrome- labelled secondary antibody alexa-488 and TexasRed (1:400; Sigma), also in blocking buffer.

A last staining was done with DAPI for nuclei visualization. Finally, neuronal cultures were washed again and mounted in fluoromount G.

For microtubules stability quantitative analyses, 1 div DRG cells were cultured without neurotrophins. To assess acetylated, tyrosinated, and total tubulin integrated in microtubules without unpolymerized tubulin subunits, cells were simultaneously fixed and permeabilized 24 hours after plating in PHEM buffer (60 mM Pipes, 25 mM Hepes, 5 mM EGTA, and 1 mM $MgCl_2$) containing 0.25% glutaraldehyde, 4% paraformaldehyde, 4% sucrose, and 0.1% Triton X-100 for 15 min at RT. Later than washing in PBS and quenching in 50 mM ammonium chloride for 5 min, cells were blocked for 45 min at RT. The blocking solution consisted of 10% foetal bovine serum (Gibco) and 0.1% Triton X-100 in PBS (adapted from Witte et al. 2008).

Double-staining was done. For microtubule acetylation experiments, 4ºC overnight incubation with mouse anti-acetylated α-tubulin (Sigma) and rabbit anti-β-tubulin III (Sigma) was performed. For microtubule tyrosination experiments, incubation with mouse anti-tyrosinated α-tubulin (Sigma) and rabbit anti- anti-β-tubulin III (Sigma) was performed also at 4ºC overnight. As secondary antibodies anti-mouse-Alexa-488 (1:1000; Sigma) and anti-rabbit-Alexa-633 (1:2000; Sigma) were used 1 h at RT. Finally, dissociated DRGs were mounted in DAPI-fluoromount G.

name	**comercial**	**reference**	**dilution**
β-tubulin III	Sigma	T 2200	1/1000
Cytochrome c	Invitrogen	33-8200	1/200
ATPaseV	Invitrogen	459240	1/500
Tom20	Sigma	HPA011562	1/300
acetylated α-tubulin	Sigma	T7451	1/20000
tyrosinated α-tubulin	Sigma	T 9028	1/2000

Table M4. Antibodies used in adult Dorsal Root Ganglia cultures characterization. References and dilutions are shown.

Soma area and morphology study.

Imaging of neurons for morphology study was performed on a Leica True Confocal Scanning SP2 imaging system (DMIRE2 microscope, Leica DFC280 camera, 63x 1.4NA apochromat oil immersion objective). Images were acquired with Leica Confocal Software. For morphology characterization number of processes was counted at acquiring time. Z axis was used to be sure how many neurites belonged to one neuron.

Images were scaled and binarized with ImageJ software version 1.48a (Rasband, W.S., ImageJ, U. S. National Institutes of Health, Bethesda, Maryland, USA, http://imagej.nih.gov/ij/, 1997-2015) to do the measurements.

This study was done with 5 and 7 months mice. At list 30 neurons for each condition was counted.

Mitochondria distribution inside neurites.

Imaging of neurons for morphology study was performed on a Leica True Confocal Scanning SP2 imaging system (DMIRE2 microscope, Leica DFC280 camera, 63x 1.4NA apochromat oil immersion objective). Images were acquired with Leica Confocal Software at same time as morphology study.

Neurite length and microtubule stability quantitative analysis.

For fluorescence quantification all the immunostained coverslips were kept at 4°C for 48h prior to image capture. In order to avoid variations because of the time spent to take the images, same day were imaged wild type and *Gdap1*$^{-/-}$cultures, under same conditions. This study was done with 5 months mice. At list 60 neurons form 2 mice were imaged for each condition.

Imaging of acetylated and tyrosinated tubulin was performed on a Leica True Confocal Scanning SP8 imaging system (DMI6000 microscope, 63x 1.4NA apochromat oil immersion objective plus 0,75 zoom). Stacks of z-axis were done with the purpose of collecting the fluorescence of the entire neurite instead of working only with one axis. Stacks of 6 images separated by 0.21 µm along the z-axis were acquired using multi-channel imaging on LAS AF 3 software.

All image processing was performed in ImageJ software version 1.48a (Rasband, W.S., ImageJ, U. S. National Institutes of Health, Bethesda, Maryland, USA, http://imagej.nih.gov/ij/, 1997-2015).Maximum projections for each stack was used to quantification. Neurite was select in the β-tubulin III channel and fluorescence intensity was measured in acetylated or tyrosinated tubulin channel. Data was expressed in arbitrary units of fluorescence per micron of length (AU/µm). As same time as neurite was select, length of 3 longest was quantified. Length was expressed in micron (µm).

Postnatal DRG and SCG cultures experiments

Animals for ganglia cultures.

All these experiments were done in Babraham Institute, under the supervision of Dr. M.P. Coleman (Gilley 2010; Milde 2014). Head and spinal column of 1 *Gdap1*$^{+/+}$ (wild type) and 3 *Gdap1*$^{-/-}$ mice were sent from Valencia. The same tissues from 3 C57BL/6J Babr control animals were obtained in Babraham and subject to the same time on ice.

Postnatal DRG and SCG cultures.

SCG and DRG were dissected from P1-P2 pups and keep in L15 medium at 4ºC until dissociation. For ganglia cultures from Valencia mice, head and spinal column of each animal were shipped in Hibernate A medium (Gibco) plus2 mM glutamine, 1% penicillin/streptomycin, 100 ng/ml 7S NGF (all Invitrogen), and 2% B27 50X (Gibco) in a low temperature box (cool but not frozen). When the tissues arrived to Babraham, dissection of SCG -from the head- and DRG -from the spinal column- was done.

Dissected SCG and DRG ganglia were incubated in 0.025% trypsin (Sigma) in PBS (without $CaCl_2$ and $MgCl_2$) for 30 min at RT. The following incubation was in 0.2% collagenase type II (Gibco) in PBS for 30 min at 37ºC. Ganglia were then gently triturated using a pipette. Dissociated ganglia were incubated 2 hours as a pre-plating stage in a non treated plastic dish (37ºC, 5% CO_2). After this pre-plating stage non-neuronal cells attached to plastic dish and neurons were recollected and plated in a 1 cm^2 poly-L-lysine and laminin-coated area of normal 3.5 cm dishes ibidi m-dishes (Thistle Scientific) for microinjection experiments.

SCG cultures were maintained in Dulbecco’s Modified Eagle’s Medium (DMEM) high glucose with 4,500 mg/L glucose and 110 mg/L sodium pyruvate (Sigma), 2 mM glutamine, 1% penicillin/streptomycin, 100 ng/ml 7S NGF (all Invitrogen), and 10% fetal bovine serum (Sigma). 100 ng/L Aphidicolin (Calbiochem) was used to reduce proliferation and viability of non-neuronal cells.

DRG cultures were maintained in Dulbecco’s Modified Eagle’s Medium (DMEM) high glucose with 4,500 mg/L glucose and 110 mg/L sodium pyruvate(Sigma), 2 mM glutamine, 1% penicillin/streptomycin, 100 ng/ml 7S NGF (all Invitrogen), and 2% B27 50X (Gibco). As same as SCG, 100 ng/L Aphidicolin (Calbiochem) was used to reduce proliferation and viability of non-neuronal cells (Gilley & Coleman 2010).

Plasmids for microinjection.

GDAP1 plasmids (Pedrola et al. 2008) were shipped in Watman paper from Valencia (Spain) to Babraham (United Kingdom). Watman paper was put into an eppendorf with MilliQ water for several hours prior to transform subcloning efficiency DH5alfa competent cells (Invitrogen).

QIAprep Spin Miniprep Kit (Qiagen) was used in order to obtain again plasmids. All constructs were verified by DNA sequencing (Cogenics Lark UK) to be sure that mutations of Gdap1 and Gdap1 not mutated were maintained and cloned properly.

EndoFree Plasmid Maxi Kit (Qiagen) was used to obtain endotoxin free plasmids more concentrated than the Miniprep products.

For mitochondria marker, mito-tagRFP (Milde et al. 2013) was kindly provided by Dr Stefan Milde (Brabraham, UK).

Microinjection of ganglia cultures.

Microinjection was performed on a Zeiss Axiovert 200 microscope with an Eppendorf 5171 transjector and 5246 micromanipulator system and Eppendorf Femtotips. Plasmids were diluted in 0.5xPBS and passed through a Spin-X filter (Costar). The mix of one GDAP1 plasmid plus mito-tagRFP was injected directly into the nuclei of SCG and DRG neurons in dissociated cultures (Gilley & Coleman 2010).

In order to use the same animals for SCG and DRG cultures, dissection and plating of SCG and DRG was done the same time. Microinjection of DRG was done after 4 days "in vitro"(div) and SCG after 6 div.

Thirty to sixty neurons were injected per dish. Few neurons injected per dish facilitated visualization of individual labelled neurite as it tend to cluster together in bundles.

Live imaging of mitochondria transport in ganglia cultures.

Imaging of mitochondria transport in SCG and DRG neurons in dissociated cultures was performed on an Olympus CellR imaging system (IX81 microscope, Hamamatsu ORCA ER camera, 100x 1.45 NA apochromat objective). During imaging, dissociated cultures were maintained in the proper medium at 37°C in an environment chamber (Solent Scientific). Images were captured at 1 frame per second for 2 min (Gilley & Coleman 2010; Milde et al. 2015). Five to ten individual movies (often containing multiple neurites) were captured for each primary culture. The live imaging was done one day after microinjection, 5div for DRG and 7div for SCG cultures.

Image processing and quantification of ganglia cultures mitochondria.

Individual neurites were straightened using the Straighten plugin in ImageJ software version 1.48a (Rasband, W.S., ImageJ, U. S. National Institutes of Health, Bethesda, Maryland, USA, http://imagej.nih.gov/ij/, 1997-2015). Axonal transport parameters were determined for individual axons using the Difference Tracker set of ImageJ plugins (Andrews et al. 2010). Analysis parameters were set up for those images in order to not lose fast mitochondria (Enhance Contrast, Saturated=5, Normalized all; Minimum difference=10; Difference frame offset=4; Minimum tracked intensity=20; Minimum feature size=2; Initial flexibility=15; Subsequent flexibility=7; Min track length= 4).Number of mitochondria in 1000 pixels, average speed, maximum speed and particle volume data were used to calculate number of moving mitochondria in 100µm/sec, average speed (µm/sec), maximum speed (µm/sec), moving mitochondria size (µm).

Total track count and the total particle count from binarized first image of the stack was use to calculate the percentage of moving mitochondria. With the same binarized first image of the stack we calculate the maximum diameter of static mitochondria.

Data analysis and statistics for ganglia cultures mitochondria.

At list 30-40 neurites were analysed in this experiment for each condition (Wild Type, *Gdap1*$^{-/-}$ and rescued). 15-45 neurites were analysed for mutations.

As wild type population is a mix data of one animal from Valencia and 3 animals from Babraham, normality and comparison test were done in order to check the data for each parameter were not statistically different (p-value > 0.05) in between this two group of animals.

Sciatic nerve explants experiments

Animals for Sciatic nerve explants.

All these experiments were done in Centro de Investigación Principe Felipe (CIPF). Animal work was approved by the CIPF's Experimentation Committee and carried out in accordance with the Real Decreto 53/2013.

Gdap1$^{-/-}$mice were crossed with mito-Dendra2 homozygotes (B6;129S6-Gt(ROSA)26Sortm1.1(mito-Dendra2)Dcc/J from Jackson Laboratory) in order to label sciatic nerve mitochondria for live imaging. Dendra 2 is a green-to-red irreversible photoswitchable monomeric protein, it's fusion with the mitochondrial targeting signalling of subunit VIII of cytochrome c oxidase generates "mito-Dendra2", capable of mitochondrial-specific fluorescence. In this strain mito-Dendra2 is introduced into the ubiquitously-expressed Gt(ROSA)26Sor gene downstream of a CAG (CMV-βactin) promoter. All organs isolated from these animals exhibit bright green fluorescence localized specifically to the mitochondrial compartment. . (http://jaxmice.jax.org/strain/018397.html)

Male mice of 1 month old heterozygous for mito-Dendra2 and homozygous for *Gdap1* were used for this experiment comparison. Thus, 3 *Gdap1*$^{+/+}$/mito-Dendra2$^{+/-}$ and 2 *Gdap1*$^{-/-}$/mito-Dendra2$^{+/-}$ were compared.

Sciatic nerve explants.

Mice were humanely killed by cervical dislocation. Sciatic nerves were dissected rapidly and immersed immediately into pre-warmed (37°C), pre-oxygenated Neurobasal-A medium (Gibco) (Milde et al. 2015).

Live imaging of axonal transport in Sciatic nerve.

Imaging of axonal transport in sciatic explants was performed on a Leica TCS SP2 AOBS (Leica Microsystems Heidelberg GmbH, Mannheim, Germany) inverted laser scanning confocal microscope using 63X Plan-Apochromat-Lambda Blue oil objective (1.4 N.A.)

Images were captured at 1 frame each 2 second for 2 min and all confocal images were acquired using the same settings. During imaging sciatic nerve were maintained in oxygenated Neurobasal A medium at 37ºC in an enviroment chamber (PECON System). Six to ten individual movies (containing multiple axons) were captured for each sciatic nerve explant.

The order of imaging was varied randomly between animals of different genotype.

Image processing and quantification of sciatic nerve mitochondria.

Individual axons were straightened using the Straighten plugin in software version 1.48 (Rasband, W.S., ImageJ, U. S. National Institutes of Health, Bethesda, Maryland, USA, http://imagej.nih.gov/ij/, 1997-2015).Axonal transport parameters were determined for individual axons using the Difference Tracker set of ImageJ plugins (Andrews et al., 2010).

Analysis parameters were set up for those images in order to not lose fast mitochondria (Enhance Contrast, Saturated=5, Normalized all; Minimum difference=39; Difference frame offset=1; Minimum tracked intensity=30; Minimum feature size=4; Initial flexibility=22; Subsequent flexibility=17; Min track length= 4).
Number of mitochondria in 1000pixels, average speed, maximum speed and particle volume data were used to calculate number of moving mitochondria in 100µm/sec, average speed (µm/sec), maximum speed (µm/sec), moving mitochondria size (µm).
The total particle count from binarized first image of the stack and total track count were used to calculate the percentage of moving mitochondria. With the same binarized first image of the stack the maximum diameter of static mitochondria was calculated.

A total number of axons of 143 for wild type and 130 for *Gdap1*$^{-/-}$ were analysed in this experiment.

Statistical analysis of data

Normality test were used for each evaluated parameter in order to use the proper comparison test (Student's t test or Mann–Whitney *U* test). Statistical differences were assumed when p-value of appropriate comparison test was under 0.05 (*), 0.01 (**) or 0.001(***).

Annex

Type	Gene	Age of onset	Evocative phenotypes
Autosomal dominant CMT1 (AD-CMT1)			
CMT1A	*PMP22* (dup)	All ages	Classic form. Hypertrophy of nerves
HNPP	*PMP22* (del)	2 to 64 years	Recurrent entrapment neuropathies. Multifocal neuropathies
CMT1B	*MPZ*	1st–2nd decade	Clinically more severe than CMT1A
CMT1C	*LITAF*	Childhood	Abnormal gait. Occasional nerve hypertrophy. Rarely deafness
CMT1D	*EGR2*	1st decade	DSS/CHN. Possible cranial nerve involvement. Scoliosis
CMT1E	*PMP22*	Childhood	Associated with deafness
CMT1F	*NEFL*	1–13 years	CMT1 with early onset. Severe disease
CMT ‘plus’	*FBLN5*	4th–5th decade	Skin hyperelasticity. Age-related macular degeneration
Autosomal dominant CMT2 (AD-CMT2)			
CMT2A	*MFN2*	6 months to 50 years	Prominent distal weakness. Late proximal weakness. Optic atrophy. CNS involvement
CMT2B	*RAB7*	2nd decade	Severe sensory loss. Foot ulcers. Arthropathy and amputations
CMT2C	*TRPV4*	Birth to 60 years	Younger more severe. Motor predominance. Vocal cord, diaphragm, respiratory involvement/dHMN
CMT2D	*GARS*	16 to 30 years	Distal upper limb predominance dHMN
CMT2E	*NEFL*	1st–5th decade	Hearing loss. Hyperkeratosis
CMT2F	*HSPB1*	Adult	Classic/dHMN
CMT2G	12q12-q13.2	2nd decade	Classic
CMT2I	*MPZ*	Late	Classic
CMT2J	*MPZ*	Late	Deafness and pupillary abnormalities
CMT2K	*GDAP1*	Variable	vocal paralysis and pyramidal features
CMT2L	*HSPB8*	15 to 33 years	Classic/dHMN
CMT2M	*DNM2*	1st–2nd decade	Tremor
CMT2N	*AARS*	15 to 50 years	Classic
CMT2O	*DYNC1H1*	Early childhood	Sometimes learning difficulties
CMT2P	*LRSAM1*	27 to 40 years	Mild. Sometimes asymmetry
CMT2Q	*DHTKD1*	13 to 25 years	Classic CMT
HMSN-P	*TFG*	17 to 55 years	Proximal involvement. Tremor. Diabetes mellitus
CMT2	*HARS*	Late onset	Sensory predominant
CMT2	*MARS*	Late onset	Motor-sensory
CMT2	*MT-ATP6*	1st–2nd decade	Motor predominant. Pyramidal signs
Dominant and recessive X linked CMT			
CMTX1	*GJB1*	1st–2nd decade	Classic. Occasional deafness
CMTX4	*AIFM1*	Early childhood	Mental retardation. Deafness
CMTX5	*PRPS1*	Childhood	Mild–moderate neuropathy. Deafness. Late optic atrophy
CMTX6	*PDK3*	Childhood	Classic CMT

Type	**Gene**	**Age of onset**	**Evocative phenotypes**
Dominant intermediate CMT			
DI-CMTA	10q24.1-q25.1	7 to 72 years	Classic CMT
DI-CMTB (CMT2M)	*DNM2*	1st-2nd decade	Classic CMT with neutropenia and early onset cataract
DI-CMTC	*YARS*	7–59 years	Classic CMT
DI-CMTD	*MPZ*	30–50 years	Sensory loss and weakness. Deafness/pupil disorders
DI-CMTE	*INF2*	5 to 28 years	Glomerulosclerosis and proteinuria
DI-CMTF	*GNB4*	5 to 45 years	Classic CMT
Autosomal recessive CMT1 AR-CMT1 (CMT4)			
AR-CMT1A	*GDAP1*	< 2 years	Severe and progressive. Vocal cord and diaphragm paralysis in some cases
AR-CMT1B1	*MTMR2*	3 years	Severe CMT1. Facial/bulbar weakness. Scoliosis
AR-CMT1B2	*MTMR13 (SBF2)*	4–13 years	Severe CMT1. Glaucoma. Kyphoscoliosis
AR-CMT1B3	*MTMR5 (SBF1)*	5–11 years	Pes planus. Scoliosis
AR-CMT1C	*SH3TC2*	Early onset 1st–2nd decade	Severe to moderate CMT1. Scoliosis. Deafness
AR-CMT1D	*NDRG1*	< 10 years	Severe CMT1. Deafness. Tongue atrophy
AR-CMT1E	*EGR2*	Birth	Congenital hypotonia. Respiratory failure. Arthrogryposis
AR-CMT1F	*PRX*	Birth to first decade	CMT1. Prominent sensory involvement
AR-CMT1G (HMSN-Russe)	*HK1*	8–16 years	Severe to moderate CMT1
AR-CMT1H	*FGD4*	< 2 years	Delayed milestones. Scoliosis. Severe course
AR-CMT1J	*FIG4*	Congenital, childhood or adult	Severe disorder. Similarities to motor neuron disease
AR-CMT1	*SURF1*	Childhood	Severe. Associated to cerebellar ataxia, brain MRI abnormalities and lactic acidosis
Autosomal recessive CMT2 AR-CMT2 (CMT2)			
AR-CMT2A (CMT2B1)	*LMNA*	2nd decade	Severe course. Distal and proximal weakness
AR-CMT2B (CMT2B2)	*MED25*	28 to 42 years	Classic CMT2
AR-CMT2C (CMT2B5)	*NEFL*	1st decade	Severe form
AR-CMT2F/	*HSPB1*	Variable	Sometimes proximal leg weakness
AR-CMT2H	*GDAP1*	1st decade	Pyramidal involvement. Vocal cord involvement
AR-CMT2K (rarely AD)	*GDAP1*	Early-onset form	Severe form. Vocal cord paralysis. Skeletal deformities. Milder dominant form
AR-CMT2P	*LRSAM1*	3rd–4th decade	Cramps. Erectile dysfunction
(HMSN VI)	*MFN2*	Early onset	Optic atrophy
ARAN-NM	*HINT1*	1st decade	Neuromyotonia
GAN	*GAN*	Childhood	Severe axonal neuropathy with early onset CNS involvement. Milder form CMT-like

Table A1. Classification of HMSN or Charcot–Marie–Tooth (CMT) diseases. Abbreviations: DEL, deletion; DUP, duplication; AARS, alanyl-tRNAsynthetase; AD, autosomal dominant; AIFM1, apoptosis-inducing factor mitochondrion-associated 1; AR, autosomal recessive; CHN, congenital hypomyelinating neuropathy; CNS, central nervous system; DHTKD1, dehydrogenase E1 and transketolase domain-containing 1; DI, dominant intermediate; DNM2, dynamin 2; DSS, DejerineSottas Syndrome; DYNC1H1, dynein cytoplasmic 1 heavy chain 1; EGR2, early growth response 2; FBLN5, fibulin 5; FGD4, actin filament-binding protein frabin; FIG4, FIG4homolog SAC1 lipid phosphatase domain containing; GAN, Giant axonal neuropathy; GJB1, gap-junction protein β-1; GARS, glycyl-tRNAsynthetase; GDAP1, ganglioside-induced differentiation-associated protein 1; HARS, histidyl-tRNAsynthetase; HK1, hexokinase 1; dHMN, distal hereditary motor neuropathy; HMSN, hereditarymotor and sensory neuropathy; HNPP, hereditary neuropathy with liability to pressure palsies; HSPB1, heat shock protein B1; HSPB8, heat shock protein B8; LITAF, lipopolysaccharide-induced tumor necrosis factor; LMNA, lamin A/C; LRSAM1, leucine-rich repeats and sterile alpha motif-containing 1; MARS, methionyl-tRNAsynthetase; MED25, meditor complex subunit 25; INF2, inverted formin 2; MFN2, mitofusin 2; MPZ, myelin protein zero; MT-ATP6, ATP6 subunit of the mitochondrial ATP synthase; MTMR2, myotubularin-related protein 2; MTMR5, myotubularin-related protein 5; MTMR13, myotubularin-related protein 13; NDRG1, N-myc downstream-regulated gene 1 protein; NEFL, neurofilament light chain; PDK3, pyruvate dehydrogenase kinase isoenzyme 3; PMP22, peripheralmyelin protein 22; PRPS1, phosphoribosyl pyrophosphate synthetase 1; PRX, periaxin; RAB7, RAS-associated protein RAB7; SBF1, SET binding factor 1; SBF2, SET binding factor 2; SH3TC2, SH3 domain and tetratricopeptides repeats 2; SURF1, Surfeit 1; TFG, TRK-fused gene; TRPV4, transient receptor potential cation channel subfamily V member 4; YARS, tyrosyltRNAsynthetase (Tazir et al. 2014).

DB-ID	DNA Change	Type	Location	Exon	Affected	Protein change	Reference
GDAP1_00001	c.27_28del	Deletion	Exon	1	Non-specific	p.(Gly10Glufs*15)	Crimella et al. (2010)
GDAP1_00009	c.92G>A	Substitution	Exon	1	GST-N	p.(Trp31*)	Baxter et al. (2002)
GDAP1_00003	c.101C>G	Substitution	Exon	1	GST-N	p.(Ser34Cys)	Crimella et al. (2010)
GDAP1_00047	c.102C>G	Substitution	Exon	1	GST-N	p.(=)	Sahin-Calapoglu et al. (2009)
GDAP1_00049	c.172_173delinsTTA	Ins/Del	Exon	2	GST-N	p.(Pro59Alafs*4)	Sevilla et al. (2008)
GDAP1_00010	c.174_176delinsTGTG	Ins/Del	Exon	2	GST-N	p.(Pro59Valfs*4)	Auer-Grumbach et al. (2008)
GDAP1_00027	c.233C>T	Substitution	Exon	2	GST-N	p.(Pro78Leu)	Bouhouche et al. (2007b)
GDAP1_00011	c.295C>T	Substitution	Exon	2	GST-N	p.(Gln99*)	Moroni et al. (2009)
GDAP1_00035	c.311-1G>A	Substitution	Intron	2	-	p.?	Kabzinska et al. (2005)
GDAP1_00053	c.332C>A	Substitution	Exon	3	GST-N	p.(Pro111His)	Chung et al. (2011)
GDAP1_00012	c.341_344del	Deletion	Exon	3	GST-N	p.(Glu114Alafs*32)	Claramunt et al. (2005)
GDAP1_00028	c.347T>C	Substitution	Exon	3	GST-N	p.(Met116Thr)	Kabzinska et al. (2006a)
GDAP1_00029	c.347T>G	Substitution	Exon	3	GST-N	p.(Met116Arg)	Di Maria et al. (2004)
GDAP1_00015	c.349dup	Duplication	Exon	3	GST-N	p.(Tyr117Leufs*13)	Senderek et al. (2003)
GDAP1_00004	c.358C>T	Substitution	Exon	3	Non-specific	p.(Arg120Trp)	Claramunt et al. (2005)
GDAP1_00031	c.359G>A	Substitution	Exon	3	Non-specific	p.(Arg120Gln)	Boerkoel et al. (2003)
GDAP1_00032	c.364C>A	Substitution	Exon	3	Non-specific	p.(Gln122Lys)	Moroni et al. (2009)
GDAP1_00055	c.368A>G	Substitution	Exon	3	Non-specific	p.(His123Arg)	Zimon et al. (2011)
GDAP1_00017	c.373C>T	Substitution	Exon	3	Non-specific	p.(Arg125*)	Fusco et al. (2011)
GDAP1_00034	c.389C>G	Substitution	Exon	3	GST-N	p.(Ser130Cys)	Kabzinska et al. (2005)
GDAP1_00018	c.439del	Deletion	Exon	3	Non-specific	p.(Thr147Leufs*5)	Georgiou et al. (2006)
GDAP1_00036	c.445G>T	Substitution	Exon	3	Non-specific	p.(Asp149Tyr)	Parman et al. (2004)
GDAP1_00037	c.458C>T	Substitution	Exon	3	α4α5 loop	p.(Pro153Leu)	Kabzinska et al. (2007)
GDAP1_00056	c.467C>G	Substitution	Exon	3	α4α5 loop	p.(Ala156Gly)	Zimon et al. (2011)
GDAP1_00005	c.469A>C	Substitution	Exon	3	α4α5 loop	p.(Thr157Pro)	Claramunt et al. (2005)
GDAP1_00038	c.482G>A	Substitution	Exon	3	α4α5 loop	p.(Arg161His)	Baxter et al. (2002)
GDAP1_00019	c.485-2A>G	Substitution	Intron	3	α4α5 loop	p.?	De Sandre-Giovannoli et al. (2
GDAP1_00013	c.487C>T	Substitution	Exon	4	α4α5 loop	p.(Gln163*)	Claramunt et al. (2005)
GDAP1_00020	c.507T>C	Substitution	Exon	4	α4α5 loop	p.(=)	Boerkoel et al. (2003)
GDAP1_00016	c.507T>G	Substitution	Exon	4	α4α5 loop	p.(=)	Senderek et al. (2003)
GDAP1_00051	c.533A>G	Substitution	Exon	4	α4α5 loop	p.(Asn178Ser)	Zhang et al. (2004)
GDAP1_00023	c.558del	Deletion	Exon	4	α4α5 loop	p.(Ile186Metfs*20)	Stojkovic et al. (2004)
GDAP1_00044	c.571C>T	Substitution	Exon	4	α4α5 loop	p.(Arg191*)	Barankova et al. (2007)
GDAP1_00050	c.579+1G>A	Substitution	Intron	4	α4α5 loop	p.?	Senderek et al. (2003)
GDAP1_00021	c.581C>G	Substitution	Exon	5	α4α5 loop	p.(Ser194*)	Cuesta et al. (2002) Sevilla et a
GDAP1_00006	c.652C>G	Substitution	Exon	5	GST-C	p.(Gln218Glu)	Chung et al. (2008)
GDAP1_00039	c.656T>A	Substitution	Exon	5	GST-C	p.(Val219Asp)	Moroni et al. (2009)
GDAP1_00054	c.656T>G	Substitution	Exon	5	GST-C	p.(Val219Gly)	Chung et al. (2011)
GDAP1_00059	c.664G>A	Substitution	Exon	5	GST-C	p.(Glu222Lys)	Kabzinska et al. (2014)
GDAP1_00025	c.668T>A	Substitution	Exon	5	GST-C	p.(Leu223*)	De Sandre-Giovannoli et al. (2
GDAP1_00007	c.678A>T	Substitution	Exon	5	GST-C	p.(Arg226Ser)	Crimella et al. (2010)
GDAP1_00040	c.679A>G	Substitution	Exon	5	GST-C	p.(Asn227Asp)	Kabzinska et al. (2010)
GDAP1_00041	c.692C>T	Substitution	Exon	5	GST-C	p.(Pro231Leu)	Xin et al. (2008)
GDAP1_00046	c.694+24C>T	Substitution	Intron	5	-	p.(=)	Sahin-Calapoglu et al. (2009)
GDAP1_00014	c.715C>T	Substitution	Exon	6	GST-C	p.(Leu239Phe)	Ammar et al. (2003)
GDAP1_00008	c.719G>A	Substitution	Exon	6	GST-C	p.(Cys240Tyr)	Cassereau et al. (2009)
GDAP1_00052	c.767A>G	Substitution	Exon	6	GST-C	p.(His256Arg)	Zhang et al. (2004)
GDAP1_00026	c.786del	Deletion	Exon	6	GST-C	p.(Phe263Leufs*22)	Nelis et al. (2002)
GDAP1_00002	c.805G>A	Substitution	Exon	6	GST-C	p.(Gly269Arg)	Crimella et al. (2010)
GDAP1_00030	c.811G>A	Substitution	Exon	6	GST-C	p.(Gly271Arg)	Ammar et al. (2003)
GDAP1_00042	c.817C>G	Substitution	Exon	6	GST-C	p.(Arg273Gly)	Kabzinska et al. (2010)
GDAP1_00057	c.821C>T	Substitution	Exon	6	GST-C	p.(Pro274Leu)	Zimon et al. (2011)
GDAP1_00045	c.836A>G	Substitution	Exon	6	GST-C	p.(Tyr279Cys)	Sahin-Calapoglu et al. (2009)
GDAP1_00043	c.844C>T	Substitution	Exon	6	GST-C	p.(Arg282Cys)	Kabzinska et al. (2010)
GDAP1_00058	c.845G>A	Substitution	Exon	6	GST-C	p.(Arg282His)	Lin et al. (2011)
GDAP1_00022	c.862dup	Duplication	Exon	6	Non-specific	p.(Thr288Asnfs*3)	Cuesta et al. (2002)Sevilla et a
GDAP1_00033	c.891C>G	Substitution	Exon	6	HD	p.(Asn297Lys)	Moroni et al. (2009)
GDAP1_00024	c.929G>A	Substitution	Exon	6	Non-specific	p.(Arg310Gln)	Azzedine et al. (2003)
GDAP1_00048	c.980G>A	Substitution	Exon	6	TMD	p.(Gly327Asp)	Kabzinska et al. (2011)

Table A2. *Gdap1* genetic variants. Cassereau database. Sequence variations are described basically as recommended by the Ad-Hoc Committee for Mutation Nomenclature (AHCMN), with the recently suggested additions (den Dunnen JT and Antonarakis SE [2000], Hum.Mut. 15:7-12); for a summary see GDAP1 DB-ID: Database Identifier. DNA change: Variation at DNA-level (cDNA). Type: Type of variant at DNA level. Location: Variant location at DNA level. Exon: Exon numbering. Affected domain: Affected domain of the protein. RNA change: Variation at RNA-level, (?) unknown but probably identical to DNA. Protein: Variation at protein level. Reference: Reference describing the variation. (Cassereu database:LOVD v.2.0 Build 36©2004-2014 Leiden University Medical Center)

606598: GANGLIOSIDE-INDUCED DIFFERENTIATION-ASSOCIATED PROTEIN 1; GDAP1		
Name	Condition(s)	Clinical significance (Last reviewed)
GDAP1, IVS4DS, G-A, +1	CMTRIA	Pathogenic(Mar 1, 2003)
GDAP1, 1-BP INS, 349T	CMTRIA	Pathogenic(Mar 1, 2003)
GDAP1, 1-BP INS, 863A	AR-CMT2 +cvp	Pathogenic(Jan 1, 2002)
GDAP1:c.92G>A (p.Trp31Ter)	CMT4A	Pathogenic(Jan 1, 2002)
GDAP1:c.169A>C (p.Ser57Arg)	CMT4A	Uncertain significance(May 22, 2015)
GDAP1:c.347T>G (p.Met116Arg)	CMT4A	Pathogenic(Sep 13, 2012)
GDAP1:c.358C>T (p.Arg120Trp)	CMT2K; CMT4A	Pathogenic(Jun 6, 2015)
GDAP1:c.368A>G (p.His123Arg)	CMT2K	Pathogenic(Aug 9, 2011)
GDAP1:c.372C>G (p.Tyr124Ter)	not provided	Likely pathogenic
GDAP1:c.373C>T (p.Arg125Ter)	CMT4A	Pathogenic(May 27, 2014)
GDAP1:c.431C>T (p.Pro144Leu)	not provided	Likely pathogenic
GDAP1:c.467C>G (p.Ala156Gly)	CMT2K	Pathogenic(Aug 9, 2011)
GDAP1:c.469A>C (p.Thr157Pro)	CMT2K	Pathogenic(Apr 1, 2005)
GDAP1:c.482G>A (p.Arg161His)	CMT4A	Pathogenic(Jan 1, 2002)
GDAP1:c.487C>T (p.Gln163Ter)	AR-CMT2 +cvp	Pathogenic(Sep 13, 2012)
GDAP1:c.556A>G (p.Ile186Val)	CMT4A	Uncertain significance(Apr 4, 2015)
GDAP1:c.581C>G (p.Ser194Ter)	CMT2K; AR-CMT2 +cvp;CMT4A	Pathogenic(Apr 1, 2003)
GDAP1:c.652C>G (p.Gln218Glu)	CMT2K	Pathogenic(Jan 1, 2008)
GDAP1:c.678A>T (p.Arg226Ser)	CMT2K	Pathogenic(Oct 1, 2010)
GDAP1:c.692C>T (p.Pro231Leu)	CMT2K	Pathogenic(Sep 1, 2008)
GDAP1:c.715C>T (p.Leu239Phe)	CMT2K; CMT4A; CMTRIA	Pathogenic(Feb 28, 2013)
GDAP1:c.719G>A (p.Cys240Tyr)	CMT2K	Pathogenic(Apr 1, 2009)
GDAP1:c.821C>T (p.Pro274Leu)	CMT2K	Pathogenic(Aug 9, 2011)
GDAP1:c.844C>T (p.Arg282Cys)	CMTRIA	Pathogenic(Dec 24, 2002)
GDAP1:c.980G>A (p.Gly327Asp)	CMTRIA	Pathogenic(May 1, 2011)

Table A3. Some *Gdap1* pathogenic variants and related CMT diseases. cvp: vocal cord paresis(OMIM® and Online Mendelian Inheritance in Man® are registered trademarks of the Johns Hopkins University. Copyright® 1966-2015 Johns Hopkins University)

References

Alavi, M. V & Fuhrmann, N., 2013. Dominant optic atrophy, OPA1, and mitochondrial quality control: understanding mitochondrial network dynamics. *Molecular neurodegeneration*, 8(1), p.32.

Alberts, B. et al., 2007. *Molecular biology of the cell*,

Del Amo, V.L. et al., 2015. Mitochondrial defects and neuromuscular degeneration caused by altered expression of Drosophila Gdap1: Implications for the Charcot-Marie-Tooth neuropathy. *Human Molecular Genetics*, 24(1), pp.21–36.

Andrews, S., Gilley, J. & Coleman, M.P., 2010. Difference Tracker: ImageJ plugins for fully automated analysis of multiple axonal transport parameters. *Journal of Neuroscience Methods*, 193(2), pp.281–287.

Bala, U. et al., 2014. Harvesting the maximum length of sciatic nerve from adult mice: a step-by-step approach. *BMC Research Notes*, 7(1), p.714.

Baxter, R. V et al., 2002. Ganglioside-induced differentiation-associated protein-1 is mutant in Charcot-Marie-Tooth disease type 4A/8q21. *Nature genetics*, 30(1), pp.21–22.

Bishop, D.L. et al., 2004. Axon branch removal at developing synapses by axosome shedding. *Neuron*, 44(4), pp.651–661.

Bloch-Gallego, E., 2015. Mechanisms controlling neuromuscular junction stability. *Cellular and Molecular Life Sciences*, 72(6), pp.1029–1043.

Boerkoel, C.F. et al., 2003. CMT4A: Identification of a hispanic GDAP1 founder mutation. *Annals of Neurology*, 53(3), pp.400–405.

Bolinches Amorós, A., 2014. Papel de la mitocondria en la neurodegeneración de las nueropatías periféricas.

Brennan, K.M., Bai, Y. & Shy, M.E., 2015. Demyelinating CMT-what’s known, what's new and what's in store? *Neuroscience Letters*, 596, pp.14–26.

Brooks, S.P. & Dunnett, S.B., 2009. Tests to assess motor phenotype in mice: a user’s guide. *Nature reviews. Neuroscience*, 10(7), pp.519–529.

Burté, F. et al., 2014. Disturbed mitochondrial dynamics and neurodegenerative disorders. *Nature Reviews Neurology*, 11(1), pp.11–24.

Cagalinec, M. et al., 2013. Principles of the mitochondrial fusion and fission cycle in neurons. *J Cell Sci*, 126, pp.2187–97.

Carlson, E.A., Rao, V.K. & Yan, S.S., 2013. From a Cell’s Viewpoint: Targeting Mitochondria in Alzheimer’s disease. *Drug Discov Today Strateg.*, 10(2), pp.91–98.

Cartoni, R. et al., 2010. Expression of mitofusin 2R94Q in a transgenic mouse leads to Charcot-Marie-Tooth neuropathy type 2A. *Brain*, 133(5), pp.1460–1469.

Cassereau, J. et al., 2009. Mitochondrial complex i deficiency in GDAP1-related autosomal dominant Charcot-Marie-Tooth disease (CMT2K). *Neurogenetics*, 10(2), pp.145–150.

Cassereau, J. et al., 2011. Mitochondrial dysfunction and pathophysiology of Charcot-Marie-Tooth disease involving GDAP1 mutations. *Experimental Neurology*, 227(1), pp.31–41.

Chapman, A.L. et al., 2013. Axonal Transport Defects in a Mitofusin 2 Loss of Function Model of Charcot-Marie-Tooth Disease in Zebrafish. *PLoS ONE*, 8(6).

Chen, H. et al., 2003. Mitofusins Mfn1 and Mfn2 coordinately regulate mitochondrial fusion and are essential for embryonic development. *Journal of Cell Biology*, 160(2), pp.189–200.

Chiavegatto, S. et al., 2000. A functional role for complex gangliosides: motor deficits in GM2/GD2 synthase knockout mice. *Experimental neurology*, 166(2), pp.227–234.

Claramunt, R. et al., 2005. Genetics of Charcot-Marie-Tooth disease type 4A: mutations, inheritance, phenotypic variability, and founder effect. *J Med Genet*, 42, pp.358–365.

Coleman, M.P. & Freeman, M.R., 2010. Wallerian Degeneration, Wld S, and Nmnat. *Annual Review of Neuroscience*, 33(1), pp.245–267.

Cuesta, A. et al., 2002. The gene encoding ganglioside-induced differentiation-associated protein 1 is mutated in axonal Charcot-Marie-Tooth type 4A disease. *Nature genetics*, 30(1), pp.22–25.

d'Ydewalle, C. et al., 2011. HDAC6 inhibitors reverse axonal loss in a mouse model of mutant HSPB1-induced Charcot-Marie-Tooth disease. *Nature medicine*, 17(8), pp.968–974.

Decosterd, I. & Woolf, C.J., 2000. Spared nerve injury: An animal model of persistent peripheral neuropathic pain. *Pain*, 87(2), pp.149–158.

El-Abassi, R., England, J.D. & Carter, G.T., 2014. Charcot-Marie-Tooth Disease: An Overview of Genotypes, Phenotypes, and Clinical Management Strategies. *Pm&R*, 6(4), pp.342–355.

Estela, A. et al., 2011. Charcot-marie-tooth-related gene GDAP1 complements cell cycle delay at G 2/M phase in Saccharomyces cerevisiae fis1 gene-defective cells. *Journal of Biological Chemistry*, 286(42), pp.36777–36786.

Fischer, A.H. et al., 2008. Hematoxylin and Eosin Staining of Tissue and Cell Sections. *Cold Spring Harbor Protocols* , 2008 (5), p.pdb.prot4986.

Fu, M. meng & Holzbaur, E.L.F., 2014. Integrated regulation of motor-driven organelle transport by scaffolding proteins. *Trends in Cell Biology*, 24(10), pp.564–574.

Gilley, J. et al., 2012. Age-dependent axonal transport and locomotor changes and tau hypophosphorylation in a "P301L" tau knockin mouse. *Neurobiology of Aging*, 33(3), pp.621.e1–621.e15.

Gilley, J., Adalbert, R. & Coleman, M.P., 2011. Modelling early responses to neurodegenerative mutations in mice. *Biochemical Society transactions*, 39(4), pp.933–8.

Gilley, J. & Coleman, M.P., 2010. Endogenous Nmnat2 Is an Essential Survival Factor for Maintenance of Healthy Axons. *PLoS Biology*, 8(1).

Guedes-Dias, P. & Oliveira, J.M.A., 2013. Lysine deacetylases and mitochondrial dynamics in neurodegeneration. *Biochimica et Biophysica Acta - Molecular Basis of Disease*, 1832(8), pp.1345–1359.

Halliwell, B., 2014. Cell culture, oxidative stress, and antioxidants: Avoiding pitfalls. *Biomedical Journal*, 0(0), p.0.

Huber, N. et al., 2013. Charcot-Marie-Tooth disease-associated mutants of GDAP1 dissociate its roles in peroxisomal and mitochondrial fission. *EMBO reports*, 14(6), pp.545–52.

Iurlaro, R. & Muñoz Pinedo, C., 2015. Cell death induced by endoplasmic reticulum stress. *FEBS Journal*, p.n/a–n/a.

Jackson, M. & Tourtellotte, W., 2014. Neuron culture from mouse superior cervical ganblion. *bio-protocol*, 4.

Janke, C. & Kneussel, M., 2010. Tubulin post-translational modifications: Encoding functions on the neuronal microtubule cytoskeleton. *Trends in Neurosciences*, 33(8), pp.362–372.

Jerath, N.U. & Shy, M.E., 2014. Hereditary motor and sensory neuropathies: Understanding molecular pathogenesis could lead to future treatment strategies. *Biochimica et biophysica acta*, 1852(4), pp.667–678.

Juárez, P. & Palau, F., 2012. Neural and molecular features on Charcot-Marie-Tooth disease plasticity and therapy. *Neural Plasticity*, 2012.

Kádar, A. et al., 2009. Improved method for combination of immunocytochemistry and Nissl staining. *J Neurosci Methods*, 184(1), pp.115–118.

Kanning, K.C., Kaplan, A. & Henderson, C.E., 2010. Motor Neuron Diversity in Development and Disease. *Annual Review of Neuroscience*, 33(1), pp.409–440.

Kapitein, L.C. & Hoogenraad, C.C., 2015. Building the Neuronal Microtubule Cytoskeleton. *Neuron*, 87(3), pp.492–506.

Katirji, B. et al., 2013. *Neuromuscular Disorders in Clinical Practice*,

Kedlaya, D., 2014. emedicine.medscape.com.

Kevenaar, J.T. & Hoogenraad, C.C., 2015. The axonal cytoskeleton: from organization to function. *Frontiers in molecular neuroscience*, 8(August), p.44.

Klapdor, K. et al., 1997. A low-cost method to analyse footprint patterns. *Journal of Neuroscience Methods*, 75(1), pp.49–54.

Krieger, F. et al., 2013. Fast motor axon loss in SMARD1 does not correspond to morphological and functional alterations of the NMJ. *Neurobiology of Disease*, 54, pp.169–182.

Krinke, G.J. et al., 2014. Experience with examination of the spinal cord and peripheral nervous system (PNS) in mice: A brief overview. *Experimental and Toxicologic Pathology*, 66(7), pp.277–280.

Lallemend, F. & Ernfors, P., 2012. Molecular interactions underlying the specification of sensory neurons. *Trends in Neurosciences*, 35(6), pp.373–381.

Li, M.X. & Dewson, G., 2015. Mitochondria and apoptosis: emerging concepts. *F1000prime reports*, 7(April), p.42.

Lovas, J.R. & Wang, X., 2013. The meaning of mitochondrial movement to a neuron's life. *Biochimica et Biophysica Acta - Molecular Cell Research*, 1833(1), pp.184–194.

Luong, T.N. et al., 2011. Assessment of motor balance and coordination in mice using the balance beam. *Journal of visualized experiments : JoVE*, (49), pp.5–7.

Ma, Q. et al., 2003. Morphological study of disordered myelination and the degeneration of nerve fibers in the spinal cord of mice lacking complex gangliosides. *Archives of Histology and Cytology*, 66(1), pp.37–44.

Malik, A.N. & Czajka, A., 2013. Is mitochondrial DNA content a potential biomarker of mitochondrial dysfunction? *Mitochondrion*, 13(5), pp.481–492.

Mallik, A.K. & Weir, A.I., 2005. Nerve conduction studies: essentials and pitfalls in practice. *Journal of neurology, neurosurgery, and psychiatry*, 76 Suppl 2, pp.ii23–i31.

Manganelli, F. et al., 2014. Charcot-Marie-Tooth disease: Frequency of genetic subtypes in a Southern Italy population. *Journal of the Peripheral Nervous System*, 19(4), pp.292–298.

Marco, A. et al., 2004. Evolutionary and Structural Analyses of GDAP1, Involved in Charcot-Marie-Tooth Disease, Characterize a Novel Class of Glutathione Transferase-Related Genes. *Molecular Biology and Evolution*, 21(1), pp.176–187.

Matsushima, S. & Sadoshima, J., 2015. The role of sirtuins in cardiac disease. *American Journal of Physiology - Heart and Circulatory Physiology*, 1(5), p.ajpheart.00053.2015.

Milde, S. et al., 2015. Axonal transport declines with age in two distinct phases separated by a period of relative stability. *Neurobiology of Aging*, 36(2), pp.971–981.

Milde, S., Gilley, J. & Coleman, M.P., 2013. Subcellular Localization Determines the Stability and Axon Protective Capacity of Axon Survival Factor Nmnat2. *PLoS Biology*, 11(4).

Misgeld, T. et al., 2007. Imaging axonal transport of mitochondria in vivo. *Nature methods*, 4(7), pp.559–561.

Misgeld, T. & Kerschensteiner, M., 2006. In vivo imaging of the diseased nervous system. *Nature reviews. Neuroscience*, 7(6), pp.449–63.

Misko, A. et al., 2010. Mitofusin 2 is necessary for transport of axonal mitochondria and interacts with the Miro/Milton complex. *The Journal of neuroscience : the official journal of the Society for Neuroscience*, 30(12), pp.4232–40.

Murray, L., Gillingwater, T.H. & Kothary, R., 2014. Dissection of the transversus abdominis muscle for whole-mount neuromuscular junction analysis. *Journal of visualized experiments : JoVE*, (83), p.e51162.

Murray, L.M., Talbot, K. & Gillingwater, T.H., 2010. Review: Neuromuscular synaptic vulnerability in motor neurone disease: Amyotrophic lateral sclerosis and spinal muscular atrophy. *Neuropathology and Applied Neurobiology*, 36(2), pp.133–156.

Nguyen, T.T. et al., 2014. Loss of Miro1-directed mitochondrial movement results in a novel murine model for neuron disease. *Proc Natl Acad Sci U S A*, 111(35), pp.E3631–40.

Ni, H.M., Williams, J.A. & Ding, W.X., 2015. Mitochondrial dynamics and mitochondrial quality control. *Redox Biology*, 4, pp.6–13.

Niemann, A. et al., 2005. Ganglioside-induced differentiation associated protein 1 is a regulator of the mitochondrial network: New implications for Charcot-Marie-Tooth disease. *Journal of Cell Biology*, 170(7), pp.1067–1078.

Niemann, A. et al., 2009. GDAP1 mutations differ in their effects on mitochondrial dynamics and apoptosis depending on the mode of inheritance. *Neurobiology of Disease*, 36(3), pp.509–520.

Niemann, A. et al., 2014. The Gdap1 knockout mouse mechanistically links redox control to Charcot-Marie-tooth disease. *Brain*, 137(3), pp.668–682.

Noack, R. et al., 2012. Charcot-Marie-Tooth disease CMT4A: GDAP1 increases cellular glutathione and the mitochondrial membrane potential. *Human Molecular Genetics*, 21(1), pp.150–162.

Ogawa, F. et al., 2016. NDE1 and GSK3β associate with TRAK1 and regulate axonal mitochondrial motility: Identification of cyclic AMP as a novel modulator of axonal mitochondrial trafficking. *ACS Chemical Neuroscience*, p.acschemneuro.5b00255.

Ong, S.-B. et al., 2015. Mitochondrial fusion and fission proteins as novel therapeutic targets for treating cardiovascular disease. *European Journal of Pharmacology*, 763, pp.1–11.

Otera, H., Ishihara, N. & Mihara, K., 2013. New insights into the function and regulation of mitochondrial fission. *Biochimica et biophysica acta*, 1833(5), pp.1256–68.

Palmano, K. et al., 2015. The role of gangliosides in neurodevelopment. *Nutrients*, 7(5), pp.3891–3913.

Pareyson, D. et al., 2015. Mitochondrial dynamics and inherited peripheral nerve diseases. *Neuroscience Letters*, 596, pp.66–77.

Paus, T. & Toro, R., 2009. Could Sex Differences in White Matter be Explained by g ratio? *Frontiers in neuroanatomy*, 3(September), p.14.

Pedrola, L. et al., 2008. Cell expression of GDAP1 in the nervous system and pathogenesis of Charcot-Marie-Tooth type 4A disease. *J Cell Mol Med*, 12(2), pp.679–689.

Pedrola, L. et al., 2005. GDAP1, the protein causing Charcot-Marie-Tooth disease type 4A, is expressed in neurons and is associated with mitochondria. *Human Molecular Genetics*, 14(8), pp.1087–1094.

Perier, C. et al., 2013. Accumulation of mitochondrial DNA deletions within dopaminergic neurons triggers neuroprotective mechanisms. *Brain*, 136(8), pp.2369–2378.

Pla-Martín, D., 2012. *Fisiopatología celular del déficit de Gdap1, relacionado con la enfermedad de Charcot Marie Tooth*.

Pla-Martín, D. et al., 2013. Silencing of the Charcot-Marie-Tooth disease-associated gene GDAP1 induces abnormal mitochondrial distribution and affects Ca2+ homeostasis by reducing store-operated Ca2+ entry. *Neurobiology of Disease*, 55, pp.140–151.

Pun, S. et al., 2002. An intrinsic distinction in neuromuscular junction assembly and maintenance in different skeletal muscles. *Neuron*, 34(3), pp.357–370.

Punga, A.R. & Ruegg, M.A., 2012. Signaling and aging at the neuromuscular synapse: Lessons learnt from neuromuscular diseases. *Current Opinion in Pharmacology*, 12(3), pp.340–346.

Purves, D. et al., 2004. *Neuroscience third edition*,

Richner, M. et al., 2014. Peripheral Nerve Injury Modulates Neurotrophin Signaling in the Peripheral and Central Nervous System. *Molecular Neurobiology*, 50(3), pp.945–970.

Rogers, D.C. et al., 2001. SHIRPA , a protocol for behavioral assessment : validation for longitudinal study of neurological dysfunction in mice. *Advances*, 306, pp.304–307.

Rossor, A.M., Evans, M.R.B. & Reilly, M.M., 2015. A practical approach to the genetic neuropathies. *Practical Neurology*, 15(3), pp.187–198.

Saez-Atienzar, S. et al., 2016. Bcl-xL-mediated antioxidant function abrogates the disruption of mitochondrial dynamics induced by LRRK2 inhibition. *Biochimica et Biophysica Acta - Molecular Basis of Disease*, 1862(1), pp.20–31.

Sajic, M., 2014. Mitochondrial Dynamics in Peripheral Neuropathies. *Antioxidants & redox signaling*, 00(00), pp.1–20.

Sevilla, T. et al., 2003. Clinical, electrophysiological and morphological findings of Charcot-Marie-Tooth neuropathy with vocal cord palsy and mutations in the GDAP1 gene. *Brain*, 126(9), pp.2023–2033.

Sevilla, T. et al., 2008. Vocal cord paresis and diaphragmatic dysfunction are severe and frequent symptoms of GDAP1-associated neuropathy. *Brain*, 131(11), pp.3051–3061.

Sheikh, K.A. et al., 1999. Mice lacking complex gangliosides develop Wallerian degeneration and myelination defects. *Proceedings of the National Academy of Sciences of the United States of America*, 96(June), pp.7532–7537.

Shi, L., Fu, A.K.Y. & Ip, N.Y., 2012. Molecular mechanisms underlying maturation and maintenance of the vertebrate neuromuscular junction. *Trends in Neurosciences*, 35(7), pp.441–453.

Shield, A.J., Murray, T.P. & Board, P.G., 2006. Functional characterisation of ganglioside-induced differentiation-associated protein 1 as a glutathione transferase. *Biochemical and Biophysical Research Communications*, 347(4), pp.859–866.

Sivera, R. et al., 2013. Charcot-Marie-Tooth disease: Genetic and clinical spectrum in a Spanish clinical series. *Neurology*, 81(18), pp.1617–1625.

Smith, G.M., Falone, A.E. & Frank, E., 2012. Sensory axon regeneration: rebuilding functional connections in the spinal cord. *Trends in Cell Biology*, 35(3), pp.156–163.

Song, W. et al., 2013. Mutant SOD1G93A triggers mitochondrial fragmentation in spinal cord motor neurons: Neuroprotection by SIRT3 and PGC-1?? *Neurobiology of Disease*, 51, pp.72–81.

Stifani, N., 2014. Motor neurons and the generation of spinal motor neuron diversity. *Frontiers in cellular neuroscience*, 8(October), p.293.

Tang, B.L., 2015. MIRO GTPases in Mitochondrial Transport, Homeostasis and Pathology. *Cells*, 5(1), p.1.

Tankisi, H. et al., 2012. Correlation between compound muscle action potential amplitude and duration in axonal and demyelinating polyneuropathy. *Clinical Neurophysiology*, 123(10), pp.2099–2105.

Tazir, M. et al., 2014. Hereditary motor and sensory neuropathies or Charcot-Marie-Tooth diseases: An update. *Journal of the Neurological Sciences*, 347(1-2), pp.14–22.

Timmerman, V., Strickland, A. V. & Züchner, S., 2014. Genetics of Charcot-Marie-Tooth (CMT) disease within the frame of the human genome project success. *Genes*, 5(1), pp.13–32.

Tintignac, L. a, Brenner, H.-R. & Rüegg, M.A., 2015. Mechanisms Regulating Neuromuscular Junction Development and Function and Causes of Muscle Wasting. *Physiological reviews*, 95(3), pp.809–52.

Ugrenović, S. et al., 2015. Morphometric analysis of the diameter and g-ratio of the myelinated nerve fibers of the human sciatic nerve during the aging process. *Anatomical Science International*.

Valdés-Sánchez, T. et al., 2010. BDNF is essentially required for the early postnatal survival of nociceptors. *Developmental Biology*, 339(2), pp.465–476.

Wakabayashi, J. et al., 2009. The dynamin-related GTPase Drp1 is required for embryonic and brain development in mice. *Journal of Cell Biology*, 186(6), pp.805–816.

Wiethölter, H., Eckert, S. & Stevens, A., 1990. Measurement of atactic and paretic gait in neuropathies of rats based on analysis of walking tracks. *Journal of Neuroscience Methods*, 32(3), pp.199–205.

Witte, H., Neukirchen, D. & Bradke, F., 2008. Microtubule stabilization specifies initial neuronal polarization. *Journal of Cell Biology*, 180(3), pp.619–632.

Wloga, D. & Gaertig, J., 2010. Post-translational modifications of microtubules. *Journal of cell science*, 123(Pt 20), pp.3447–55.

Wong, F. et al., 2009. Axonal and neuromuscular synaptic phenotypes in WldS, SOD1G93A and ostes mutant mice identified by fiber-optic confocal microendoscopy. *Molecular and Cellular Neuroscience*, 42(4), pp.296–307.

Wu, H., Xiong, W.C. & Mei, L., 2010. To build a synapse: signaling pathways in neuromuscular junction assembly. *Development (Cambridge, England)*, 137(7), pp.1017–33.

Wu, H.-J. et al., 2015. The Molecular Mechanisms Between Autophagy and Apoptosis: Potential Role in Central Nervous System Disorders. *Cellular and Molecular Neurobiology*, 35(1), pp.85–99.

www.pennmedicine.org, 2001. Nervous System Information. *ADAM*.

Zala, D. et al., 2013. Vesicular glycolysis provides on-board energy for fast axonal transport. *Cell*, 152(3), pp.479–491.

Zhu, Y. et al., 2007. Didanosine causes sensory neuropathy in an HIV/AIDS animal model: Impaired mitochondrial and neurotrophic factor gene expression. *Brain*, 130(8), pp.2011–2023.

Zimon, M., Baets, J. & Fabrizi, G.M., 2012. Dominant GDAP1 mutations cause predominantly mild CMT phenotypes. *Neurology*, 77(6), pp.540–548.